DIPLOMARABEIT
Master Thesis

Onset of cracking in concrete: debonding or ITZ failure? A micromechanical approach

ausgeführt zum Zwecke der Erlangung des
akademischen Grades eines Diplom-Ingenieurs

unter der Leitung von

Assoc.-Prof. Dipl.-Ing. Dr. techn. Bernhard Pichler

und

Univ. -Prof. Dipl.-Ing. Dr. techn. Christian Hellmich

Inst.Nr.: E202
Institut für Mechanik der Werkstoffe und Strukturen

eingereicht an der Technischen Universität Wien
Fakultät für Bauingenieurwesen

von

Markus Königsberger

Matr.Nr.: 07 28 166
Unterm Hals 25
A – 3541 Senftenberg

Wien, am 10.10.2012

Danksagung

Zuallererst möchte ich meinen beiden Betreuern vom Institut für Mechanik der Werkstoffe und Strukturen danken, die mir während meiner Arbeit stets mit Rat und Tat zur Seite gestanden sind. Herrn Assoc.-Prof. Dipl.-Ing. Dr. techn. Bernhard Pichler danke ich im Besonderen für die Einführung in die Materie, für die intensive Unterststützung bei den Berechnungen, sowie für seine zahlreichen Korrekturen und Anmerkungen in der Ausarbeitungsphase, die die Qualität der Arbeit maßgeblich erhöhten. Bei Herrn Univ.-Prof. Dipl.-Ing. Dr. techn. Christian Hellmich bedanke ich mich einerseits für die Chance, mich im Rahmen meiner Masterarbeit mit einem solch komplexen Thema auseinandersetzen zu dürfen, andererseits aber auch für die steuernden Eingriffe bezüglich des Inhalts der Arbeit. Beiden Betreuern danke ich für die vielen Diskussionen zu einzelnen Themenbereichen der Arbeit, durch die ich viel Neues gelernt habe und einen tiefen Einblick in den packenden Forschungsbereich der Kontinuums-Mikromechanik erlangen konnte.

Ebenfalls bedanken möchte ich mich bei meinen zukünftigen Arbeitskollegen des Institutes. Mit ihrer Hilfe und mit ihren Ratschlägen konnte ich auftretende Probleme, stets schnell beseitigen und mich neuen Herausforderungen stellen. Außdem danke ich ihnen für die freundliche Aufnahme in das Team und das ausgezeichnete Arbeitsklima, das am Institut herrscht.

Für den nötigen Rückhalt während des gesamten Studiums, selbstverständlich auch während der Abfassung meiner Masterarbeit, haben meine Eltern und meine Freundin gesorgt. Nur dank ihrer Unterstützung konnte ich privat den nötigen Ausgleich finden, und mich voller Tatendrang und Motivation in das Studiums stürzen. Herzlichen Dank dafür!

Abstract

Concrete is primarily a matrix-inclusion composite consisting of cement paste and embedded aggregates. However, within a so-called interfacial transition zone (ITZ) of 15 microns around the surface of the aggregates, cement paste exhibits a larger porosity than in the bulk, stemming from segregation effects during production of concrete. During monotonous increase of mechanical loads, onset of concrete microcracking is observed within the ITZ. However, the exact location at which microcracking starts and the related failure mechanism are still unclear. Inspection of post-failure fragments of concrete allows for *a posteriori* identification of two possibilities: in some parts of the aggregates' surfaces, a clean debonding from cement paste is observed, while in other parts, a very thin layer of cement paste remains attached to the aggregates. The former observation implies that onset of microcracking might be related to debonding in the two-dimensional interface between the aggregates and the surrounding ITZ, while the latter one suggests that also bulk failure of the thin ITZ is possible. This provides us with the motivation to study onset of concrete cracking by means of a micromechanics approach.

Herein, we develop tensile failure criteria (i) for debonding directly at the two-dimensional aggregate's surface, and (ii) for bulk failure within the three-dimensional ITZ, respectively. Debonding is envisioned, once the maximum normal component of the traction vectors acting on the aggregate's surface reaches a corresponding tensile bond strength. ITZ failure, in turn, is considered if the largest maximum principal ITZ stress reaches the tensile strength of the ITZ. The two failure criteria require access to traction vectors acting on aggregates' surfaces and to the full three-dimensional stress states within the ITZs. This is provided by a continuum micromechanics model, resolving the microstructure of concrete, based on the separation of scales principle. On the scale of several millimeters to centimeters, concrete is considered as a matrix-inclusion composite, where spherical aggregates are perfectly bonded to a matrix of cement paste. Since the thickness of the ITZ is negligible compared to the diameter of the aggregates and is significantly smaller than the typical mean inter-aggregate spacing, the ITZ is treated as a two-dimensional interface. On the much smaller scale of a few microns, the ITZ is represented as a three-dimensional spherical shell which exhibits a shell thickness of 15 microns, perfectly bonded to the aggregates. The described representation of concrete allows us to perform the scale transition from concrete-related macroloading down to microscopic traction vectors and ITZ stresses. Based on continuum micromechanics-related estimates for strain concentration tensors, we first quantify the average stresses and strains of the aggregates. Since these stresses are also relevant for the aggregates' surfaces, we use Cauchy's formula in order to compute the orientation-

dependent traction vectors acting on the aggregate's surface. Their normal components are involved in the aforementioned debonding criterion. Perfect bond-related continuity conditions for stresses and displacements, in turn, allow us to translate aggregate's stresses and strains into three-dimensional, position-dependent ITZ stress states. A subsequent principal stress analysis delivers principal ITZ stresses which are involved in the aforedescribed ITZ failure criterion.

In real concretes, onset of microcracking manifests at the material scale of concrete as the onset of pre-peak nonlinearities in measured force-displacement diagrams, such that onset of microcracking refers to the elastic limit of concrete. Consequently, our two models result in estimates for two elastic limit surfaces in the macroscopic principal stress space. Considering typical concrete properties in order to compute model predictions, and comparing them with experimentally observed elastic limits of concrete under uniaxial tension and compression, respectively, allows us to conclude that ITZ failure is governing for onset of concrete microcracking under compression-dominated loading scenarios. For tension-dominated loading scenarios, in turn, both debonding and ITZ failure appear to be possible, and the relevant failure mode is governed by the ratio between the tensile strength values related to debonding and to ITZ failure, respectively. Finally, we study the sensitivity of our model predictions with respect to the properties of the constituents of concrete, including the stiffness of aggregates, of cement paste, and of the ITZ, as well as the dosage and the Poisson's ratio of the aggregates. This shows onset of microcracking in normal concretes is quite different from that of lightweight concretes.

Kurzfassung

Beton stellt im Wesentlichen ein Matrix-Einschluss-Verbundmaterial dar, wobei Zuschlagskörner in einer Zementsteinmatrix eingebettet sind. In einer ca. 15 Mikrometer großen Schnittstellen-Übergangszone („interfacial transition zone“ ITZ) rund um die Zuschlagskornoberflächen weist der Zementstein allerdings aufgrund von Entmischungsvorgängen während der Betonherstellung eine größere Porosität als im Rest der Zementsteinmatrix auf. Steigert man monoton die makroskopische Beanspruchung von Betonen, so wird einsetzende Mikrorissbildung in dieser ITZ beobachtet. Die exakte Position der beginnenden Rissbildung und der damit verbundene Versagensmechanismus sind jedoch immer noch unklar. Betonbruchstücke aus zerstörenden Druckversuchen weisen auf zwei Möglichkeiten hin: manchmal sind die Zuschlagskornoberflächen sauber von der Zementsteinmatrix getrennt, ein andermal Regionen bleiben sehr dünne Zementsteinschichten auf den Zuschlagskörnern zurück. Die erste Beobachtung verdeutlicht, dass Ablösung in der zweidimensionalen Trennfläche zwischen den Zuschlagskörnern und der ITZ maßgebend sein könnte, während die zweite Beobachtung anzeigt, dass Versagen innerhalb der dreidimensionalen ITZ ebenso plausibel erscheint. Das ist die Motivation, einsetzendes Risswachstum in Betonen mit Hilfe eines mikromechanischen Modells zu untersuchen.

Es werden zwei Zugfestigkeitskriterien entwickelt: zum einen Ablösen entlang der zweidimensionalen Oberfläche der Zuschlagskörner und zum anderen ITZ Versagen. Ablösen wird vorhergesehen, wenn die größte auf die Zuschlagskornoberfläche wirkende Normalspannung eine entsprechende Zugfestigkeit erreicht. ITZ Versagen wiederum wird vorausgesagt, wenn die größte Hauptnormalzugspannung in der ITZ eine entsprechende Zugfestigkeit erreicht. Diese beiden Versagenskriterien erfordern die Quantifizierung mikroskopischer Spannungszustände als Funktion der makroskopischen Beanspruchung von Beton. Dieser Skalenübergang wird mit Hilfe der Kontinuumsmikromechanik ermöglicht, wobei die Mikrostruktur von Beton basierend auf dem Maßstabstrennungprinzip („separation of scales requirement“) modelliert wird. Auf dem Beobachtungsmaßstab von einigen Millimetern bis zu einigen Zentimetern wird Beton als Matrix-Einschluss-Verbundwerkstoff betrachtet, wobei kugelförmige Zuschläge kraftschlüssig mit der umgebende Zementsteinmatrix verbunden sind, d. h. die ITZ wird als zweidimensionale Trennfläche modelliert, weil die ITZ-Dicke einerseits gegenüber der charakteristischen Größe der Zuschlagskörner vernachlässigbar ist, und andererseits auch wesentlich kleiner als der charakteristische Zuschlagskornabstand. Auf dem viel kleineren Beobachtungsmaßstab von einigen Mikrometern wird die ITZ allerdings als dreidimensionale und 15 Mikrometer dicke Kugelschale modelliert, welche die Zuschlagskörner umhüllt und mit ihnen ebenfalls kraftschlüssig verbunden ist. Diese Darstellung der Mikrostruktur von Beton ist die Basis für den Maßstabsübergang von makroskopischer

Betonbeanspruchung hinunter auf mikroskopische Spannungsvektoren an der Zuschlagskornoberfläche und Spannungszustände in der ITZ. Mit Hilfe von Verzerrungskonzentrationstensoren der Kontiuumsmikromechanik werden zuerst die mittleren Spannungs- und Verzerrungszustände der Zuschläge berechnet. Da diese Spannungen auch an den Zuschlagskornoberflächen relevant sind, werden die ortsabhängigen Spannungsvektoren, die auf den Zuschlagskornoberflächen wirken, mit Hilfe der Cauchyschen Formel berechnet. Die Normalspannungskomponenten gehen in das Versagenskriterium für Ablösen der Zementsteinmatrix vom Zuschlagskorn ein. Weiters zieht kraftschlüssiger Verbund Kontinuitätsbedingungen für Spannungen und Verschiebungen nach sich; und damit können Spannungs- und Verzerrungszustände der Zuschläge in dreidimensionale und ortsabhängige Spannungszustände in der ITZ übersetzt werden. Eine nachfolgende Hauptnormalspannungsanalyse führt auf die größte Hauptzugspannung der ITZ, die in das zuvor genannte ITZ-Versagenskriterium eingeht.

In realen Betonen führt einsetzendes Mikrorisswachstum zu Nichtlinearitäten in makroskopisch gemessenen Last-Verschiebungs-kurven, sodass beginnende Mikrorissbildung mit der elastischen Grenzlast von Beton verbunden ist. Somit ergeben die beiden beschriebenen Versagenskriterien zwei elastische-Grenzbeanspruchungsflächen im Hauptnormalspannungsraum. Basierend auf typischen Betoneigenschaften werden Modellprognosen berechnet und mit experimentell beobachteten elastischen Grenzlasten von Beton unter einaxialer Zug- bzw. Druckbeanspruchung verglichen. Das erlaubt die Schlussfolgerung, dass einsetzendes Risswachstum unter dominanter Druckbeanspruchung von ITZ-Versagen herrührt. Unter dominanter Zugbeanspruchung ist sowohl Ablösen als auch ITZ-Versagen möglich, und die Frage, welcher der beiden Mechanismen relevant ist, kann nur anhand des Verhältnisses der beiden Zugfestigkeiten entschieden werden. Abschließend wird die Sensitivität der Modellprognosen in Hinblick auf Variationen der Betoneigenschaften untersucht, wobei sowohl die Steifigkeiten der Zuschläge, der Zemensteinmatrix und der ITZ, als auch die Zuschlagsdosierung und die Querdehnungszahl des Zuschlagsmaterials variiert werden. Diese Untersuchung weist darauf hin, dass Normalbeton und Leichtbetone hinsichtlich einsetzender Mikrorissbildung ein markant unterschiedliches Verhalten aufweisen.

Contents

Chapter 1

Introduction

Visual inspection of concrete reveals the heterogeneity of the material: submillimeter to millimeter-sized sand grains and millimeter to centimeter-sized aggregates are embedded in a cement paste matrix. High-resolution microscopic imaging techniques, with a characteristic pixel size of less than one micron, visualize the characteristic heterogeneities of cement paste [20]: clinker grains, hydration products, and capillary pores, with a characteristic size typically ranging from single microns to few microns. Capillary porosity is not uniform throughout the cement paste matrix, but it is larger in narrow zones around the surfaces of the aggregates and the sand grains, and it is smaller in the bulk of the cement paste [75]. These interfacial transition zones stem primarily from segregation effects associated with the characteristic production process of concrete [66], i. e. with the dynamic mixing and compaction processes of concrete, during which cement paste is not yet a solid material, but behaves rather like a viscous fluid. The typical width of interfacial transition zones amounts to 15 microns.

Because the porosity within the interfacial transition zones (ITZs) is larger than the one in the bulk cement paste, ITZs exhibit a smaller stiffness and a smaller strength than the bulk cement paste, rendering ITZs the weakest link in the immediate vicinity of the aggregates' surfaces. This becomes evident, e.g., in classical, macroscopic, short-term laboratory testing, in which concrete behaves only initially linear elastic [46, 51]. Onset of cracking in the immediate vicinity of the aggregates' surfaces results in pre-peak nonlinearities of macroscopically measured force-displacement diagrams [42, 76]. In other words, onset of microcracking is related to the elastic limit of concrete, rather than to the strength of the material.

The open literature contains a great variety of modeling approaches which aim at explaining the initiation of microcracks and/or the nonlinear shape of macroscopic stress-strain relations of concrete. In the following, we provide a brief overview over a few selected approaches. Hashin [36] studies a homogeneous two-dimensional interface between a spherical inclusion and a surrounding matrix, he defines a constitutive law in terms of a linear relation between displacement jumps and interface tractions, and he proves that this approach is equivalent to a thin (but three-dimensional) interfacial zone (or a thin coating), see also [32]. In this context, displacement jumps may be positive, indicating a separation of the inclusion from matrix, associated with tensile tractions transferred across the interface, and they may be negative, indicating a small interpenetration of inclusion and matrix, associated

with compressive tractions transferred across the interface. Nilsen and Monteiro [83] concluded, that a reliable model for concrete should include the ITZ as distinct phase, since experimentally determined elastic properties do not fall between the lower and the upper Hashin-Shtrikman bound, computed for a two-phase model of concrete (aggregates + cement paste matrix). This was the motivation for follow-up papers presenting analytical three-phase models considering aggregates, ITZs, and cement paste for predicting the elastic stiffness of concrete [49, 64, 87]. Hashin and Monteiro [37] back-analyze, from measured elastic properties of concrete, input values for their three-phase model of concrete: the elastic stiffness of the ITZ is by a factor of 2 smaller than the one the bulk cement paste. Blechman models the formation and accumulation of stable (non-propagating) microcracks in order to simulate the degradation process of concrete right up to failure [14]. Landis and Bolander simulate interface debonding with a three-dimensional lattice model where interface elements break based on a Mohr-Coulomb criterion with a tension cut-off [47]. Mihai and Jefferson combine the exterior point Eshelby solution for the stress field around a spherical inclusion with circular microcracks exhibiting rough surfaces in order to predict initiation and evolution of microcracking in concrete [57].

None of the available models distinguishes between aggregate debonding and ITZ failure, but this differentiation appears to be interesting when having a more detailed look at post-failure fragments of concrete specimens (which were produced with spherical aggregates). They reveal that the aggregates have partly clearly separated from the cement paste matrix, and partly a very thin layer of cement paste remains attached to the aggregates' surfaces [67]. One of these two failure mechanisms is obviously related to onset of microcracking, but a posteriori it is impossible to decide which one it is. Also state-of-the-art measurement equipment (such as computer tomography carried out simultaneously to mechanical loading) is not yet able to provide a convincing answer [27]. This is the motivation for the present work, where we develop micromechanics models for tension-driven onset of microcracking.

Herein, we develop two tensile failure criteria: one for clean debonding directly at the two-dimensional aggregate's surface and another one for bulk failure within the three-dimensional ITZ, respectively. Debonding is envisioned, once the maximum normal component of the traction vectors acting on the aggregate's surface reaches a corresponding tensile bond strength. ITZ failure, in turn, is considered if the largest maximum principal ITZ stress reaches the tensile strength of the ITZ. The two failure criteria require access to traction vectors acting on aggregates' surfaces and to the full three-dimensional stress states within the ITZs. To this end, we consider perfect bonding in all interfaces, and we study at which macroscopic load intensity onset of debonding or of ITZ failure, respectively, is predicted by the micromechanics models.

Motivated by the separation of scales principle, we represent the ITZ either as a two-dimensional interface, or as a three-dimensional volume, which is explained next. When it comes to the stress concentration from macrostresses imposed on the boundary of a representative concrete volume down to average stress states in aggregates, the ITZ is modeled a two-dimensional interface, because its characteristic width of 15 microns is by orders of magnitude smaller than the characteristic size of sand grains and aggregate inclusions. Average stress states within the aggregates are quantified based on a continuum micromechanics approach [86]. Assuming that these stresses are representative also close to the aggregates' surfaces, we use Cauchy's formula in order to compute the traction vectors

acting on the aggregate's surface. In general, they are orientation-dependent, i. e. they are a function of zenith angle ϕ and azimuth angle θ used to mark positions on spherical aggregate inclusions. When it comes to quantification of stress states inside the ITZ, the latter is resolved as a three-dimensional continuum in form of a spherical shell surrounding the aggregates. The transition from stress states in aggregates to ITZ stress states is based (i) again on the assumption that average aggregate stresses are representative also close to the aggregates' surfaces, (ii) on equilibrium-related continuity conditions for stresses, and (iii) on perfect bond-related continuity conditions for displacements. Except for macroscopic isotropic loading, under which the entire ITZ exhibits a uniform stress state, ITZ stress states fluctuate in space, described by zenith angle ϕ and azimuth angle θ.

The aim of this work is to translate the two different microscopic Rankine-type elastic limit criteria "debonding" and "ITZ failure" into corresponding elastic limit surfaces in principal stress space of concrete macrostresses, and to compare these model predictions with available experimental data. To this end, the thesis is organized as follows: Chapter 2 provides an overview over experimental observations which are the motivation for the modeling approach presented thereafter. Analytical solutions for the relation between macroloading imposed on a representative concrete volume, on the one hand, and traction vectors at aggregate's surface as well as three-dimensional stress states in 3D interfacial transition zones, on the other hand, are the topic of Chapter 3. These macro-micro stress concentration rules open the door towards upscaling of tensile strength criteria describing onset of debonding and onset of ITZ failure, respectively, see Chapter 4. Chapter 5 contains a comparison of the two different models, a confrontation of model-predicted elastic limits of concrete with corresponding experimental observations, as well as a sensitivity analysis regarding the influence of concrete composition of the model-predicted elastic limits. Finally, Chapter 6 contains conclusion and an outlook to future work.

Chapter 2

Experimental Observations

2.1 Pre-existing cracks and progressive cracking as reason for pre-failure nonlinearities of concrete

Hsu et al. [42] measured the length of pre-existing cracks in the region of the aggregate's surface, in thin slices of concrete samples which – apart from the loading experienced during the slicing process – were never exposed to significant mechanical stresses. The experimenters conclude that approximately 12 % of the aggregates' surfaces are not bonded to the bulk cement paste matrix and that this stems typically from gravity-driven bleeding underneath the aggregates (taking place right after the production) and from hydration-induced shrinkage of cement paste [42].

The pre-failure behavior of concrete under monotonous increase of macroscopic uniaxial compression is associated with non-linearities stemming from different microstructural processes described next. From the very beginning of the loading process, the opening-closure behavior of initially existing cracks is considered to result in small non-linearities of measured force-displacement diagrams [42, 78, 76, 25, 77]. Still, the pre-existing cracks remain quite stationary (almost no crack propagation) and only a small amount of new cracks forms, as was observed visually [42], and by ultrasonics testing [45]. Therefore, concrete is typically considered to behave practically linear elastic, see Fig. 2.1. Surpassing approximately 30-50 % of the compressive strength of the material results in onset of distributed cracking close to the aggregates surface [42, 76, 77], whereby cracks typically propagate in the direction of macroscopic loading [77, 27]. This onset of microcracking marks the elastic limit of concrete [42, 76, 46], and the corresponding macroscopic load intensity is typically referred to as initiation stress [42, 77]. Distributed microcracking intensifies with further load increase, such that macroscopic deformations increase overlain with increasing macroloading [42, 76]. Surpassing approximately 70-90 % of the compressive strength, onset of cracking in the matrix is observed [78, 76, 51], whereby cracks characteristically propagate again in direction of the macroscopic loading [77], bridging interfacial cracks of neighboring aggregates such that continuous cracks are formed [42, 77]. The described onset of matrix cracking correlates well with the point of inflection in the graph showing the macroscopic uniaxial stress over the macroscopic volumetric strain [46]. Reaching the strength of the material, i.e. at the peak load, cracks are still propagating in the direction of macroscopic loading,

but this is no longer a spatially distributed phenomenon, because cracks start to localize such that post-peak failure of concrete specimens is associated with the formation of a shear band which is inclined with respect to the direction of macroscopic loading [27].

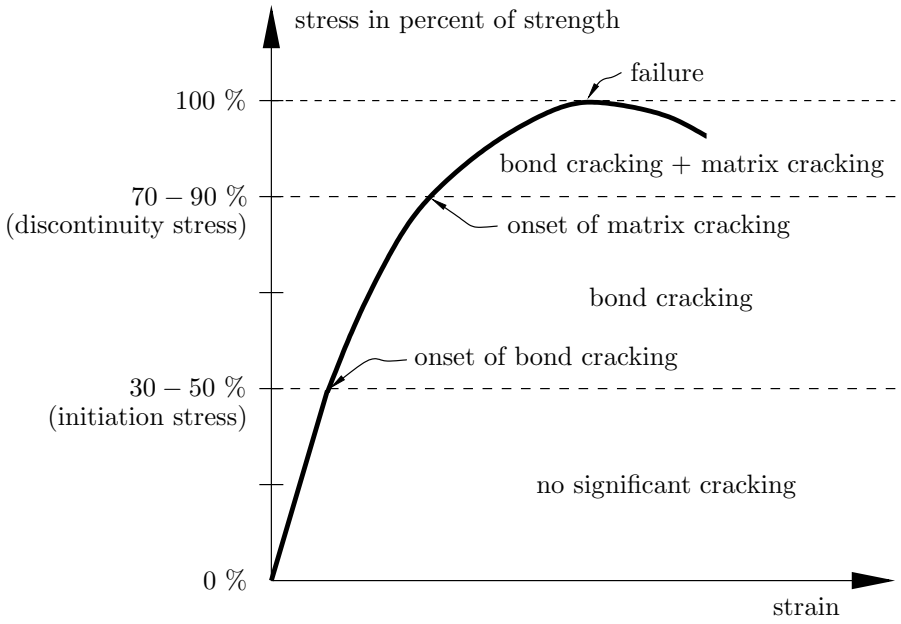

Figure 2.1: Typical stress-strain graph of concrete under uniaxial compression and the relation to the cracking behavior

Under monotonous increase of macroscopic uniaxial tension, some authors describe a more or less progressive increase of cracking in the vicinity of the aggregates' surfaces [72]. Other experimenters do not observe a deviation from linearity of the stress-strain graphs in their experiments [84]. Still, concrete is typically considered to remain practically linear elastic up to 70-80 % of the tensile strength. Further macroscopic load increase, however, results in significant microcracking and strain localization [46, 82].

Significantly less information is available for biaxial and triaxial types of macroscopic loading. Under isotropic triaxial compression, typically no cracking is observed, but the material behaves rather ductile [22]. Under other forms of triaxial compression (including the special case of biaxial compression), cracks typically propagate in planes which are orthogonal to the direction of the largest compressive stress [22].

In all cases, onset of cracking is typically observed in the immediate vicinity to the aggregates' surfaces. This is the motivation to focus on the microstructure of concrete.

2.2 Microstructure of concrete

Concrete is a hierarchically organized material, i.e. characteristic heterogeneities are observed at different scales of observation. On the scale of millimeters to centimeters, concrete is a matrix-inclusion composite consisting of aggregate stones and sand grains embedded in a matrix of cement paste. At

the finer scale of observation of several tens of microns down to a few single microns, the characteristic heterogeneity of cement paste is observed, consisting of unhydrated clinker grains, of hydration products, and of capillary pores, either filled by water or air, such as first revealed electron-optically by Chatterji and Jeffery [20].

In the immediate vicinity to the surface of the aggregate stones and sand grains, i.e. in a layer with a characteristic width of 15 microns, both porosity and clinker content of cement paste deviate from the typical values observed in the bulk paste [66, 75, 38]. In more detail, imaging techniques such as back-scattered electron microscopy [75] revealed that at the surface of the aggregates (or sand grains), the porosity is significantly larger and the clinker content is significantly smaller than in the bulk of the cement paste matrix, and with increasing distance from the surface, porosity decreases and the clinker content increases monotonically to the corresponding values of the bulk cement paste, see Fig. 2.2. This was the motivation to introduce the name "interfacial transition zone" (ITZ). The

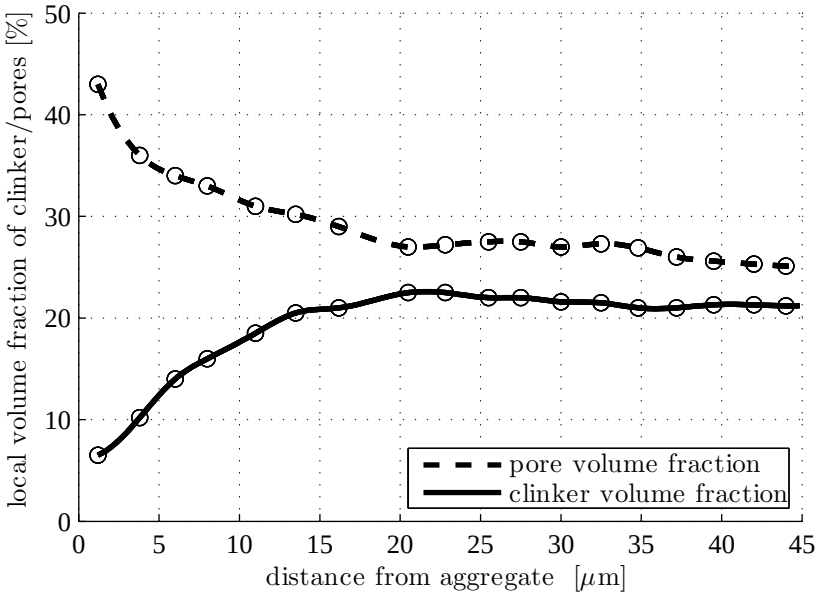

Figure 2.2: Distribution of (unhydrated) clinker volume fraction and of capillary pore volume fraction as a function of the distance to the aggregate's surface, determined one day after mixing by means of back-scattered electron microscopy [75]; (initial) water-to-cement mass ratio $w/c = 0.4$

described porosity and clinker content gradients stem from segregation effects[1] during the dynamic mixing process of the material [66] during which cement paste represents a viscous fluid and not yet a solid material. Another consequence of the segregation effect is that, right after mixing, the ITZ consists predominantly of small clinker grains, while the larger grains are "washed" out to the

[1]The segregation effect is frequently referred to as "wall effect", since a similar process can be observed at a markedly larger scale of observation, namely during the dynamic placement and compaction of concrete: aggregates segregate from cement paste in regions close to the formwork-walls such that the surface of the final concrete structure consists practically of cement paste alone.

bulk cement paste [75]. This becomes again "visible" from back-scattered electron microscopy used to quantify the temporal evolution of the clinker content in the vicinity of the aggregate's surface [75]: up to 28 days, the clinker content inside the ITZ decreases significantly faster than in the bulk cement paste, because small clinker grains dissolve much faster than large ones. During hydration, the pores around the aggregates are at least partly filled up by hydration products precipitating out of the oversaturated pore water solution. Notably, Diamond and Huang [28] describe in this context that the solution of clinker ions in somewhat greater distances from the aggregate's surface as well as transport of these ions towards the aggregate's surface compensate to some extent the initial segregation effect. Still, it is well known that the final porosity within the ITZ remains to be smaller than the one in the bulk cement paste, although quantitatively a significant scatter is measured [26, 28]. The increased ITZ porosity, in turn, implies that the ITZ exhibits smaller stiffness and strength than the bulk cement paste, rendering the ITZ the weakest link in concrete.

Indentation tests into the ITZ and into the bulk cement paste allows experimenters to quantify the contrast of their mechanical properties. Indentation modulus, i.e. the slope of the de-loading graph in a diagram showing the indentation force over depth of indentation, is related to the elastic properties, while indentation hardness, i.e. the ratio between the maximum indentation force and the projected area of the indenter, is related to the strength of the tested materials [23]. Microhardness testing of the ITZ, reviewed in [43], with an indentation size of more than 10 μm cannot be applied because the displacement of the material within the ITZ is restrained by the presence of the neighboring stiffer inclusion. In order to get access to "real" ITZ properties, the size of the indenter has to be scale-separated from the typical size of the ITZ [61] and, therefore, smaller than one micrometer. The indentation modulus of the ITZ around (unspecified) gravel aggregates obtained with a Berkovich indenter (three-side pyramid) amounts to 85 % of the modulus of the bulk paste [60, 61]. The stiffness contrast drops down to 70 % around limestone aggregates [60, 61]. In similar nanoindentation tests, Zhu and Bartos [88] could prove that gravity-driven segregation underneath aggregates and reinforcements results in ITZ properties which are significantly weaker under than above of macroheterogeneities.

2.3 Is onset of cracking related to debonding or ITZ failure?

Macroscopically (i.e. observed from a millimeter-to-centimeter scale), onset of cracking is observed in the region between the aggregates and the bulk cement paste. Therefore, the bond between aggregates and bulk cement paste is considered to represent the weakest link in concrete [42, 76, 89]. Microscopically (i.e. from an observation scale of some microns), however, one is able to distinguish between two failure modes which govern the onset of cracking in the vicinity of the aggregate's surface: debonding (resulting in a clean aggregate's surface) and ITZ failure (resulting in residual thin layer of cement paste attached to the aggregate's surface). Because there are no direct testing methods for tensile bond strength, concrete experimenters commonly do not distinguish between debonding and ITZ failure. However, experimental observations on other composite materials do show two modes of failure, debonding, on the one hand, and failure within the innermost region of the matrix phase, on the other hand. Uniaxial tension applied to a composite consisting of glass spheres (diameter

up to 30 microns) with or without a coating embedded in an epoxy matrix leads exactly to these two failure modes, visible through scanning electron microscopy of the fracture surface: uncoated spheres show debonding, spheres with coatings providing good adhesion between aggregate, coating, and epoxy show failure within the epoxy around the spheres [3], see Fig. 2.3. In a similar way, Gent

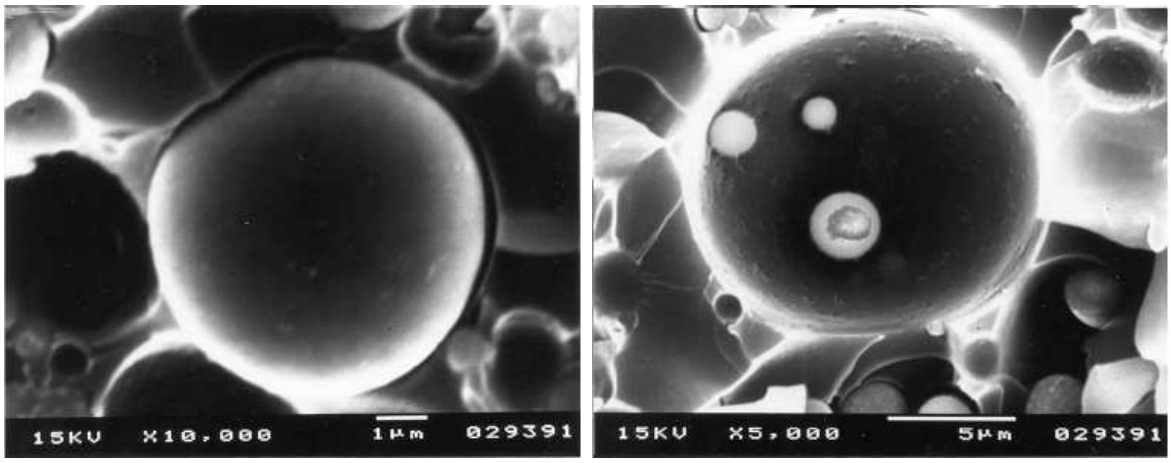

Figure 2.3: Electron scanning micrograph of fracture surface of a composite consisting of glass spheres (diameter ranging between 1 and 30 microns) and an epoxy matrix: uncoated spheres debond and show a clean aggregate's surface (left) while at the coated spheres residuals of the matrix remain at the surface (right) [3]

and Park [33] study a composite of a single spherical glass inclusion embedded in an elastomer matrix. Using a transparent elastomer, they are able to simply observe the failure phenomena from outside. They report two failure modes, (i) debonding of the matrix from the glass sphere, and (ii) cavitation (formation of a vacuole) in the vicinity of the inclusion surface.

As for concrete, post-failure crack patterns suggest that both, debonding and ITZ failure are taking place in macroscopic uniaxial compression tests on concretes. In more detail, Perry and Gillot [67] performed uniaxial compression tests on concrete samples containing spherical glass or quartzite aggregates, respectively, and they inspected post-failure fragments. Given that the "north-south-axis" of the aggregate spheres is aligned with the direction of macroscopic loading, clean debonding was observed in the region around the equator, while closer to the poles a very thin layer of cement paste remained attached to the aggregate's surface, see Fig. 2.4. In other concretes, however, only one of these two failure modes is observable. McCreath et al. [25] for instance, observe that aggregates' surfaces appear to be more or less clean, i.e. free from cement paste residues. Mindess and Diamond [58] observe the fracture surface of concrete specimens (crushed by bending) using scanning electron microscopy: fracture paths passed in the vicinity of the aggregates, but commonly not directly at the interface since clean aggregate's surfaces were seldom observed. Shah and Slate [76], however, report that clean surfaces of rock are visible to the unaided eye, indicating that the two-dimensional interface between aggregates and ITZs itself is the critical region and not the paste within the three-dimensional ITZ.

Conclusively, the question if debonding or ITZ failure governs the bond cracking behavior of con-

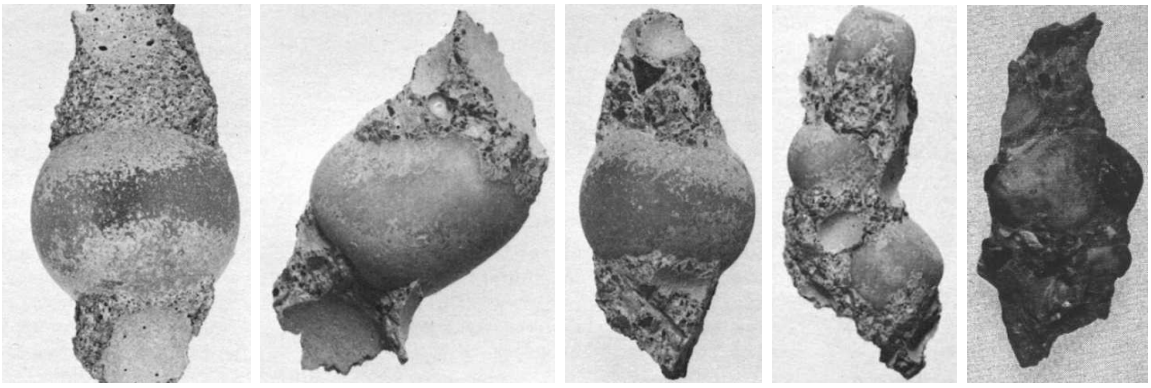

Figure 2.4: Concrete fragments consisting of aggregates and cement paste, after failure under uniaxial compression (in vertical direction), spherical glass aggregates [67] and irregular ellipsoid-shaped marble aggregates (at the far right) [25]

crete can not be answered by experimenters. Although both phenomena are experimentally observed, a distinction in language use as well as in modeling is not found.

2.4 Properties governing the onset of cracking in concrete

There are various factors which influence the initiation of microcracks in the vicinity of the aggregate's surface, and therefore, the macrostress level corresponding to the elastic limit of concrete. The applied loading as one dominating factor is already discussed, see Sec. 2.1.

2.4.1 Strength in the vicinity of the aggregate's surface

Mechanical and chemical bonds across the two-dimensional aggregate-ITZ interface govern the ultimate tensile forces transmittable from the aggregate to the ITZ. Given aggregates exhibiting an open porosity with a characteristic pore size of a few microns (typically lightweight aggregates), pore water will enter the aggregate's porosity, and precipitating hydrates will result in an interdigitation of the ITZ and the aggregate (see Fig. 2.5). This is typically referred to as mechanical interlocking [79, 53], and it is effective as long as the characteristic size of surface roughness is larger than the one of hydration products. Chemical bond, in turn, is the name given to attractive electrical forces acting on even finer scales of observation. In this context we note that a chemical reaction between calcareous aggregates and the cement paste constituents is reported in [89]. It results in an increased tensile bond strength with increasing degree of hydration. The final macroscopic tensile strength is larger than observed with equally rough inert aggregates like feldspar or granite. A similar effect is also described for siliceous rocks [5, 79]. This implies that the aggregate type has a strong influence on bond strength [41, 89, 81].

Experimenters studying the local strength in the vicinity of the aggregate's surface do not distinguish between bond failure or ITZ failure, because there is no direct testing method for the two different strength values. Therefore, test results contain information on the smaller of the two strength values.

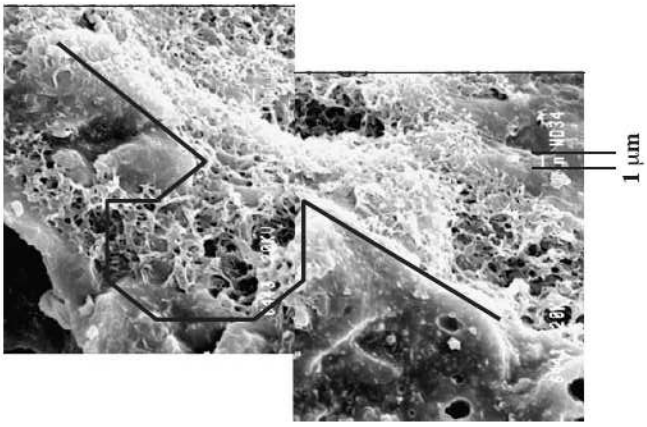

Figure 2.5: Extensive mechanical interlocking at porous aggregates due to the ingrowth of hydration products [53]

Moreover, no generally excepted test method was developed so far [19]. Different push-out tests aim at pushing a single, cylindrical aggregate out of a matrix of cement paste or mortar [59, 7, 19]. Tension tests, in turn, show that the local strength is strongly influenced by the aggregate type [41, 89, 81], by the roughness of the aggregate [41, 89, 81, 70], and by the composition of the cement paste [41], discussed in more detail in the following.

Tasong et al. [81] applied direct tension to specimens of cement paste casted on two sides against an 20 mm aggregate cube. The surfaces of the latter are, either rounded, or saw-cut, or fractured. The authors observed a major influence of the aggregate's surface roughness on the bond strength when using basalt and quartz rocks, but almost no influence when using limestone. They also noted that some of the fractured aggregates failed in their outermost regions, and conclude that the fracture process used during the production of the aggregates results in an effective aggregate strength which is smaller than the bond strength or the ITZ strength. In order to study the influence of surface roughness, similar bond tests were earlier performed by Hsu and Slate [41], where (inert) sandstone and granite aggregates show an increasing tensile strength with increasing surface roughness, while for limestone this trend was not observed. In addition, the authors report for naturally fractured limestone that 50 % of the failure surface broke through the the outermost regions of the aggregates, while another type of limestone from a different quarry and without distinct fault planes, failed directly at the aggregate-ITZ interface.

As for the properties of cement pastes, age, and composition are the main factors. The tensile strength (obtained by flexural tests) in the vicinity of the aggregates increases with increasing age, e.g. the 28-day strength is by 50 % larger than the strength at an age of seven days [4]. The bond between aggregates and the bulk cement paste was studied by Hsu and Slate [41] as a function of the initial water-to-cement mass ratios in the interval $w/c \in [0.26\,, 0.36]$. The tensile bond strength decreases with increasing w/c and it decreases more significantly than the tensile strength of the bulk cement paste. Rao and Prasad [70] measured this tensile strength of mortars with different

initial sand-to-cement ratios, casted against a mature concrete surface: On the one hand, higher sand content delivers higher bond strengths. On the other hand, the tensile strength of the mortar-to-mature concrete interface is by a factor of three smaller than the tensile strength of mortar (initial water-to-binder mass ratio: 0.4, 10 % of cement mass replaced by silica fume, initial sand-to-binder mass ratio: 3.0).

All this tensile strength tests, however, refer to initial perfect bond, i.e. they do not account for pre-existing bond cracks which is typical in concrete. What can be concluded from these experiments is that the tensile strength at the interface (be it the bond strength or the strength of the ITZ) is smaller than the strength of neat cement paste [76, 5]. Hsu and Slate [41] report that the tensile strength at the aggregate's surface amounts to some $33 - 67$ % of the tensile strength of neat cement paste. Their very comprehensive experimental activities included varying aggregate types, varying aggregate's surface roughness, and varying cement paste compositions.

2.4.2 Stiffness, shape, size, and size distribution of aggregates

The influence of the elastic properties of the aggregates compared to those of the paste can be studied when considering lightweight aggregate concretes. Lightweight aggregates (such as pumice, expanded clay, or sintered pelletised fly ash) exhibit a Young's modulus which is in the range of or even smaller than the Young's modulus of mature cement paste [63]. Similar stiffnesses are reported by [15], and this reduced stiffness contrast significantly reduces the probability of microcracking [16]. Aggregates which are more compliant than the cement paste matrix entail, that the stress fluctuations resulting from the stiffness contrast result in smaller-than-mean stresses in aggregates and larger-than-mean stresses in the bulk cement paste. The stress-strain relation under uniaxial compression or tension is less nonlinear for lightweight concrete (with aggregates of Taclite or Lydon) than for limestone concrete, and the deviation from linearity starts at macrostress levels which are closer to the strength of the material [9].

The influence of the aggregate size was studied by Akçaoğlu et al. [1, 2], who placed a single aggregate into a matrix of mortar and performed first compression tests (to a load level well below the strength of the material, but large enough to induce bond cracks) and carried out destructive tension tests thereafter. For the same pre-compression level, he observes a decrease of the tensile strength with increasing aggregate size.

The initiation stress, i.e. the macroload level at which measured force-displacement diagrams start to exhibit non-linearities, is a scattering quantity. The scatter increases with increasing aggregate shape diversity and increasing aggregate size distribution [67]. The scatter is partly induced by the heterogeneity of the ITZ [75].

2.4.3 Ultrafine additions

Using silica fume (in combination with superplasticizers which defloculate the particles) densifies the ITZs [74, 34], since these ultrafine additions fill the zones around the aggregate's surfaces, where the segregation effect yields to an initially higher porosity. Backscattered electron microscopy implies that

a 180 days old ITZ of ordinary Portland cement paste even exhibits a higher porosity than just a one day old ITZ of a cement-silica fume paste [74].

The macroscopic uniaxial compressive strength increases monotonously with increasing silica fume content [34]. Inert microfillers such as alumina or carbon black result in a similar increase of macroscopic uniaxial compressive strength [66]. Therefore, it appears that the described filling of the ITZ is more relevant than the puzzolanic reaction induced by silica fume. Also the microscopic push-out resistance of a single aggregate (sandstone, limestone, and granite) increases when replacing 20 % of the cement by silica fume [19] .

2.5 Lessons learned from two-dimensional test setups

Since a detailed three-dimensional study regarding onset of cracking in the immediate vicinity of the aggregate's surfaces is not yet available, two-dimensional studies of plate-type specimens containing cylindrical aggregates provide interesting insight into microstructural processes. Still, we note, that stress fluctuations around inclusion cylinders differ significantly from the ones around spherical inclusions, i. e. observations from two-dimensional studies do not necessarily imply that real concretes will exhibit the same behavior.

The type of the used matrix and inclusion materials as well as the number and arrangement of inclusion cylinders refer to the test setup, and the latter typically differs considerably from study to study, such that results observed in two-dimensional testing are difficult to compare. The matrix materials range from mortar [18, 52, 55] over high-strength mortar produced with silica fume [8], to gypsum [44]. The inclusions consist of limestone [18, 52, 8, 55], of basalt and diabase and many other natural stones [8], or they represent voids [55]. Typically the inclusions are stiffer than the matrix [18, 52, 8, 55, 44], but some studies also investigate inclusions which are more compliant than the matrix [8, 44], including the extreme case of an infinite stiffness contrast given for cylindrical voids [55]. The number of aggregate cylinders embedded in the tested specimens ranges from one [8, 55, 44] over two [44] or nine [18] to several [52]. The latter studies either refer to cylinders with the same diameter [52], or to cylinders exhibiting a diameter distribution [18].

Experimental observations under uniaxial compression cover a wide spectrum and are partly equivalent to what is known from real concretes. Pre-existing interface cracks, for instance, are particularly observed underneath the aggregates [52], resulting from gravity-driven segregation processes. Onset of cracking is observed – as a rule – in the vicinity of the inclusion surface. In specimens containing inclusions of different sizes, the first cracks show up around larger inclusions first [52]. Acoustic emission studies investigating the role of the cylinder diameter in specimens containing one single inclusion imply that first cracks appear at load intensities which increase with decreasing cylinder diameter [55]. The onset of cracking is associated with beginning nonlinearities in measured force-displacement diagrams [55]. The matrix cracks observed at larger load levels typically propagate in the direction of macroscopic loading [18, 52].

The largest scatter refers to the position at which onset of cracking is observed. Limestone cylinders start to debond from a mortar matrix at an angle of approximately 30 degrees with respect to the axis

of loading [55]. If the (gypsum) matrix is stiffer than the inclusions, first cracks show up in lateral regions of the cylinders (equatorial region), and if the matrix is more compliant than the inclusions, onset of cracks is observed in the region where the axis of loading intersects the cylinder surfaces (polar region). However, also an inverse observation was made: stiff basalt and diabase aggregates start to debond from a mortar matrix at the polar region, while onset of debonding with more compliant limestone aggregates took place at the equatorial region [8].

We conclude that also two-dimensional experiments do not provide a satisfactory insight into the onset of cracking phenomenon. This provides the motivation for a micromechanical analysis which allows for performing parameter studies in the framework of modeling tensile failure in the region close to the aggregate's surfaces.

Chapter 3

Analytical solutions for traction vectors at aggregate's surfaces and for stress states in 3D interfacial transition zones

In the sequel, we quantify the stress concentration from uniform macrostresses imposed on a representative concrete volume down to two different stress-like microscopic fields, namely (i) traction vectors acting on the surfaces of spherical aggregates and (ii) three-dimensional stress states in interfacial transition zones exhibiting a typical width of 15 microns [66, 75]. The proposed modeling approach is resting on the separation of scales principle [86],

$$\ell \ll d \ll \mathcal{L}\,. \tag{3.1}$$

Eq. (3.1) implies that the characteristic size d of a representative volume element (RVE) of a heterogeneous material is significantly larger than the characteristic size ℓ of the embedded heterogeneities and, at the same time, significantly smaller than characteristic size $\mathcal{L}$ of stress and strain fluctuations inside the structure containing the RVE. The former property allows for assigning homogenized material properties to the RVE, and the latter property for dealing with RVEs subjected to uniform stress or strain boundary conditions.

3.1 Fundamentals of continuum micromechanics

In applied continuum micromechanics, an RVE Ω of a heterogeneous material is typically subdivided into n_p quasi-homogeneous material phases. Each phase j (with $j = 1, 2, \ldots, n_p$) exhibits a specific elastic stiffness $\mathbb{C}_j$ and it occupies a specific subvolume Ω_j of the RVE. In the bulk of the RVE, i.e. at any position $\underline{x} \in \Omega$, we introduce field equations of linear elasticity comprising static equilibrium conditions, linear strain-displacement relations, and linear elastic material behavior in terms of generalized Hooke's law. At any position on the boundary of the RVE, i.e. at all $\underline{x} \in \partial\Omega$, a linear relation between prescribed displacement vectors and a uniform macroscopic strain state $\boldsymbol{E}$ (uniform strain

boundary conditions [35]) is considered. The described field equations and boundary conditions imply a linear strain concentration rule, i.e. a linear relation between the macrostrain $\boldsymbol{E}$ and the volume average of the microscopic phase strains $\boldsymbol{\varepsilon}_j$ [40]:

$$\boldsymbol{\varepsilon}_j = \mathbb{A}_j : \boldsymbol{E} \qquad j = 1, 2, \ldots, n_p \tag{3.2}$$

The n_p phase strain concentration tensors $\mathbb{A}_j$ also allow for upscaling microscopic phase elasticity tensors to the homogenized stiffness $\mathbb{C}_{hom}$ of the RVE [40]

$$\mathbb{C}_{hom} = \sum_{j=1}^{n_p} f_j \, \mathbb{C}_j : \mathbb{A}_j \,, \tag{3.3}$$

with f_j standing for the volume fraction of the j-th phase, $f_j = \Omega_j / \Omega$.

Estimates of phase strain concentration tensors $\mathbb{A}_j$ are obtained based on Eshelby-Laws-type matrix inclusion problems [86], where a single ellipsoidal inclusion is perfectly bonded to an infinite matrix which exhibits auxiliary stiffness tensor $\mathbb{C}_\infty$, and which is subjected to uniform auxiliary strains $\boldsymbol{E}_\infty$ at the infinitely remote boundary. One matrix-inclusion problem is considered for every material phase of the RVE such that in the j-th problem the inclusion shape and stiffness are set equal to the corresponding properties of the particular material phase. The spatially uniform strain state inside every inclusion [31, 48] serves as estimate for the average strains of the corresponding material phase. In a conceptually similar way, the auxiliary properties $\mathbb{C}_\infty$ and $\boldsymbol{E}_\infty$ are linked to corresponding properties of the RVE, based on considerations regarding phase interaction and strain compatibility [86]. In more detail, if the RVE exhibits a matrix-inclusion morphology, $\mathbb{C}_\infty$ is set equal to the matrix stiffness of the RVE; and if the RVE represents a highly disordered arrangement of directly interacting heterogeneities (so-called polycrystalline morphology), $\mathbb{C}_\infty$ is set equal to the homogenized stiffness of the RVE. The auxiliary strain $\boldsymbol{E}_\infty$, in turn, is linked to the RVE strain $\boldsymbol{E}$ based on the strain average rule. This way of reasoning provides access to tensorial expressions for strain concentration tensors reading as [12]

$$\mathbb{A}_j = \left[\mathbb{I} + \mathbb{P}_j^\infty : (\mathbb{C}_j - \mathbb{C}_\infty)\right]^{-1} : \left\{ \sum_{i=1}^{n_p} f_i \, \left[\mathbb{I} + \mathbb{P}_i^\infty : (\mathbb{C}_i - \mathbb{C}_\infty)\right]^{-1} \right\}^{-1} , \qquad j = 1, 2, \ldots, n_p \tag{3.4}$$

where $\mathbb{P}_j^\infty$ denotes the fourth-order Hill tensor which depends on the shape of the inclusion and on the stiffness of the infinite matrix. $\mathbb{I}$ denotes the symmetric fourth-order identity tensor with components $I_{ijkl} = 1/2 \, (\delta_{ik}\delta_{jl} + \delta_{il}\delta_{kj})$, where δ_{ij} denotes the Kronecker delta which is equal to 1 for $i = j$ and 0 otherwise.

3.2 Micromechanical representation of concrete including interfacial transition zones

Herein, we consider concrete to be a three-phase material comprising a cement paste matrix, millimeter-to-centimeter sized aggregates, and interfacial transition zones (ITZs) with a characteristic width of 15 microns [75]. Strongly related to the scale separation principle, we resolve concrete by means of a hierarchical micromechanical representation, involving two markedly different scales of observation, described next.

On the larger observation scale A, exhibiting a characteristic size of several millimeters to a few centimeters, we model concrete as a classical two-phase matrix-inclusion composite, comprising a continuous cement paste matrix and spherical aggregate inclusions (Fig. 3.1). The interfacial transition zones are represented as *two-dimensional* interfaces establishing a perfect bond between the aggregates and the cement paste matrix.

The *three-dimensional* nature of the interfacial transition zones, i.e. their nature as a bulk material phase, is resolved at a much finer observation scale B, exhibiting a characteristic size being equal to 15 microns (= characteristic width of ITZ [75]). In more detail, each aggregate grain is considered to be separated from the cement paste matrix by an interfacial transition zone representing a thin (but three-dimensional) spherical shell with a characteristic thickness of approximately 15 microns. Again, perfect bond is considered in both types of two-dimensional interfaces, i.e. the interface between the aggregates and the interfacial transition zones, as well as the interface between the interfacial transition zones and the cement paste matrix. The thin ITZ shell is subdivided into approximately cubic RVEs with side length being equal to the shell thickness. In agreement with the separation of scales principle, smeared (averaged) stiffness properties are assigned to the ITZ. The typical heterogeneity of the ITZ, with a characteristic size amounting to a few microns (= the size of small unhydrated clinker grains, hydration products, and capillary pores), refers to an even finer scale of observation which is beyond the scope of the two-scale model proposed herein.

Given our interest in onset of concrete cracking – triggered either by aggregate debonding or by ITZ failure – we propose a new and elegant step-by-step method for the macro-to-micro scale transition from loading imposed on a macroscopic RVE of concrete down to tractions at aggregate's surfaces and to ITZ stresses, respectively. The approach is strongly related to the scale-separated hierarchical organization described above and to the assumption of perfect bond in all observation scale-specific interfaces. First, we perform the stress concentration from the macroloading down to average aggregate stresses and strains, based on the aforedescribed two-phase representation of concrete (observation scale A). The next step refers to the finer observation scale B, where Cauchy's formula allows us to translate aggregate stresses into the traction vectors acting on the surfaces of spherical aggregates. Also on observation scale B, perfect bond-related continuity rules for stresses and strains across the interface between the aggregate and the ITZ allow us to compute the three-dimensional stress state of any RVE within the ITZ shell.

3.3 Average aggregate stresses (observation scale A)

We consider loading of a macroscopic RVE of concrete (Fig. 3.1) in form of a general stress state $\boldsymbol{\Sigma}$. Corresponding macrostrains $\boldsymbol{E}$ follow from the macroscopic elasticity law of concrete

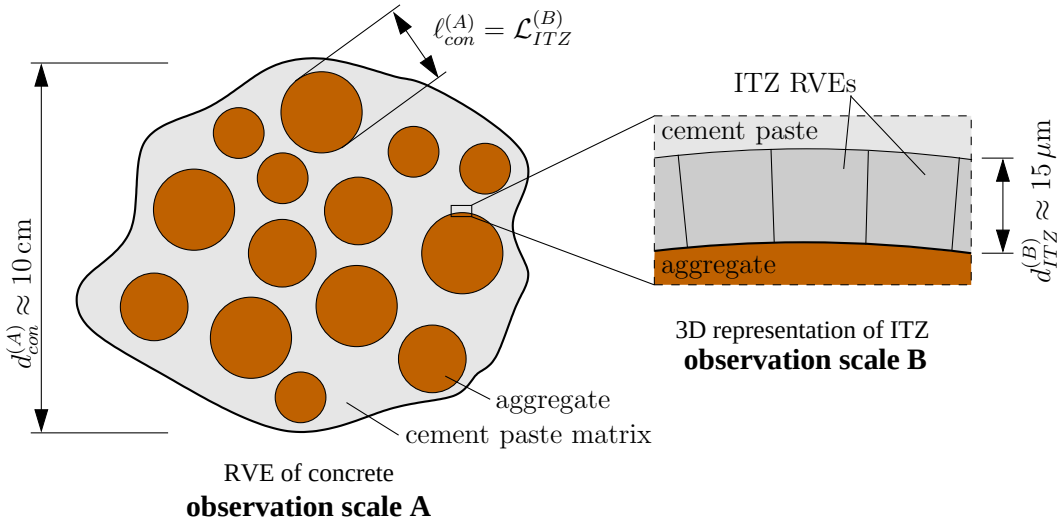

Figure 3.1: RVE of the matrix-inclusion composite "concrete" where a spherical aggregate phase is perfectly bonded to a cement paste matrix (modeled by Mori-Tanaka scheme) on observation scale A, and the three-dimensional representation of the ITZ on an even finer scale of observation (scale B); both two-dimensional sketches refer to three-dimensional volume elements

$$\boldsymbol{E} = (\mathbb{C}_{con})^{-1} : \boldsymbol{\Sigma}\,, \tag{3.5}$$

where $\mathbb{C}_{con}$ denotes the homogenized elastic stiffness of concrete, for which the micromechanical estimate is described next. In this context, both the cement paste matrix and the aggregates are considered to be isotropic such that their phase stiffness tensors can be written as

$$\mathbb{C}_j = 3\,k_j\,\mathbb{J} + 2\,\mu_j\,\mathbb{K} \qquad j = \{cp, agg\}\,. \tag{3.6}$$

k_{cp} and k_{agg} as well as μ_{agg} and μ_{cp} denote bulk moduli and shear moduli of cement paste (cp) and aggregate (agg), respectively. $\mathbb{J}$ stands for the volumetric part of the fourth-order unity tensor $\mathbb{J} = 1/3\ \mathbf{1} \otimes \mathbf{1}$ and $\mathbb{K}$ stands for its deviatoric part $\mathbb{K} = \mathbb{I} - \mathbb{J}$, where $\mathbf{1}$ denotes the second-order unity tensor with components equal to the Kronecker delta δ_{ij}. Since the sum of the volume fractions of cement paste, f_{cp}, and the one of aggregates, f_{agg}, equals one,

$$f_{cp} + f_{agg} = 1\,, \tag{3.7}$$

it is sufficient to specify the volume dosage of one phase (e.g. f_{agg}), rendering the other one (e.g. f_{cp}) a dependent quality. The envisioned matrix-inclusion morphology of concrete (Fig. 3.1) renders the Mori-Tanaka scheme [62, 12] relevant for stiffness homogenization [86]. This implies that the stiffness

of the infinite matrix C_∞ in the underlying two Eshelby problems is set equal to the stiffness of the cement paste matrix $\mathbb{C}_{cp}$ from (3.6), see [86] for details. Specification of Eq. (3.3) for Eq. (3.4) and the resulting expression for the two-phase concrete with spherical aggregates yields, under consideration of Eq. (3.7) and $\mathbb{C}_\infty = \mathbb{C}_{cp}$,

$$\begin{aligned} \mathbb{C}_{con} \quad = \quad & \left\{ (1-f_{agg})\ \mathbb{C}_{cp} + f_{agg}\, \mathbb{C}_{agg} : \left[\mathbb{I} + \mathbb{P}^{cp}_{sph} : (\mathbb{C}_{agg} - \mathbb{C}_{cp}) \right]^{-1} \right\} : \\ & \left\{ (1-f_{agg})\ \mathbb{I} + f_{agg}\ \left[\mathbb{I} + \mathbb{P}^{cp}_{sph} : (\mathbb{C}_{agg} - \mathbb{C}_{cp}) \right]^{-1} \right\}^{-1} ; \end{aligned} \tag{3.8}$$

$\mathbb{P}^{cp}_{sph}$ stands for the Hill tensor of a spherical inclusion within an infinite matrix of cement paste. It is typically decomposed into the dimensionless Eshelby tensor and the inverse of the stiffness tensor of the infinite cement paste matrix:

$$\mathbb{P}^{cp}_{sph} = \mathbb{S}^{cp}_{sph} : \mathbb{C}^{-1}_{cp} \,, \tag{3.9}$$

Because of the isotropy of the infinite cement paste matrix, the Eshelby tensor for a spherical inclusion reads as [86]

$$\mathbb{S}^{cp}_{sph} = \alpha\, \mathbb{J} + \beta\, \mathbb{K} \,, \tag{3.10}$$

with dimensionless coefficients α and β reading as

$$\alpha = \frac{3k_{cp}}{3k_{cp} + 4\mu_{cp}} \qquad \text{and} \qquad \beta = \frac{6\ (k_{cp} + 2\mu_{cp})}{5\ (3k_{cp} + 4\,\mu_{cp})} \,. \tag{3.11}$$

Eq. (3.8) delivers an isotropic homogenized stiffness estimate with homogenized bulk modulus k_{con} and homogenized shear modulus μ_{con}, respectively, reading as (see Appendix A for details)

$$k_{con} = \left(\frac{f_{agg}\, k_{agg}}{1 + \frac{\alpha(k_{agg} - k_{cp})}{k_{cp}}} + f_{cp}\, k_{cp} \right) \left(\frac{f_{agg}}{1 + \frac{\alpha(k_{agg} - k_{cp})}{k_{cp}}} + f_{cp} \right)^{-1} \tag{3.12}$$

and

$$\mu_{con} = \left(\frac{f_{agg}\, \mu_{agg}}{1 + \frac{\beta(\mu_{agg} - \mu_{cp})}{\mu_{cp}}} + f_{cp}\, \mu_{cp} \right) \left(\frac{f_{agg}}{1 + \frac{\beta(\mu_{agg} - \mu_{cp})}{\mu_{cp}}} + f_{cp} \right)^{-1} . \tag{3.13}$$

The scale transition from the macrostrains (3.5) to the average aggregate strains, $\boldsymbol{\varepsilon}_{agg}$, is provided by the strain concentration rule (3.2) which reads, specified for the aggregate phase, as

$$\boldsymbol{\varepsilon}_{agg} = \mathbb{A}_{agg} : \boldsymbol{E} \,, \tag{3.14}$$

with $\mathbb{A}_{agg}$ denoting the strain concentration tensor of the spherical aggregates, following from specification of Eq. (3.4) for the two-phase concrete as

$$\mathbb{A}_{agg} = \left[\mathbb{I} + \mathbb{P}^{\infty}_{sph} : (\mathbb{C}_{agg} - \mathbb{C}_{cp}) \right]^{-1} : \left\{ (1-f_{agg})\ \mathbb{I} + f_{agg}\ \left[\mathbb{I} + \mathbb{P}^{cp}_{sph} : (\mathbb{C}_{agg} - \mathbb{C}_{cp}) \right]^{-1} \right\}^{-1} \tag{3.15}$$

Also $\mathbb{A}_{agg}$ is a isotropic fourth-order tensor, allowing us to decompose it into a deviatoric part and a volumetric part,

$$\mathbb{A}_{agg} = A_{vol}\mathbb{J} + A_{dev}\mathbb{K}\,, \tag{3.16}$$

with dimensionless coefficients A_{vol} and A_{dev} reading as (see Appendix A for details)

$$\begin{aligned} A_{vol} &= \left(\frac{1}{1+\frac{\alpha(k_{agg}-k_{cp})}{k_{cp}}}\right)\left(\frac{f_{agg}}{1+\frac{\alpha(k_{agg}-k_{cp})}{k_{cp}}}+f_{cp}\right)^{-1}, \\ A_{dev} &= \left(\frac{1}{1+\frac{\beta(\mu_{agg}-\mu_{cp})}{\mu_{cp}}}\right)\left(\frac{f_{cp}}{1+\frac{\beta(\mu_{agg}-\mu_{cp})}{\mu_{cp}}}+f_{cp}\right)^{-1}. \end{aligned} \tag{3.17}$$

Combination of Eqs. (3.5) and (3.14) yields a macrostress-microstrain relation, reading as

$$\boldsymbol{\varepsilon}_{agg} = \mathbb{D}_{agg} : \boldsymbol{\Sigma} \qquad \text{with} \qquad \mathbb{D}_{agg} = \mathbb{A}_{agg} : (\mathbb{C}_{con})^{-1} = D_{vol}\mathbb{J} + D_{dev}\mathbb{K}\,, \tag{3.18}$$

and involving $\mathbb{D}_{agg}$, a fourth-order isotropic concentration tensor with

$$\begin{aligned} D_{vol} &= \frac{1}{3}\frac{1}{(\alpha f_{cp}+f_{agg})\,k_{agg}+[f_{cp}\,(1-\alpha)]\,k_{cp}} \\ D_{dev} &= \frac{1}{2}\frac{1}{(\beta f_{cp}+f_{agg})\,\mu_{agg}+[f_{cp}\,(1-\beta)]\,\mu_{cp}} \end{aligned} \tag{3.19}$$

Average microscopic stresses within the aggregate phase, $\boldsymbol{\sigma}_{agg}$, follow from the elasticity law

$$\boldsymbol{\sigma}_{agg} = \mathbb{C}_{agg} : \boldsymbol{\varepsilon}_{agg}\,, \tag{3.20}$$

with $\mathbb{C}_{agg}$ derived in Eq. (3.6). Combination of Eqs. (3.5), (3.14), and (3.20) results in a linear relation between macroscopic RVE loading and microscopic aggregate stresses:

$$\boldsymbol{\sigma}_{agg} = \mathbb{B}_{agg} : \boldsymbol{\Sigma} \qquad \text{with} \qquad \mathbb{B}_{agg} = \mathbb{C}_{agg} : \mathbb{A}_{agg} : (\mathbb{C}_{con})^{-1} = B_{vol}\mathbb{J} + B_{dev}\mathbb{K} \tag{3.21}$$

where $\mathbb{B}_{agg}$ denotes the isotropic fourth-order stress concentration tensor of the aggregate phase with

$$\begin{aligned} B_{vol} &= \frac{k_{agg}}{(\alpha f_{cp}+f_{agg})\,k_{agg}+[f_{cp}\,(1-\alpha)]\,k_{cp}} \\ B_{dev} &= \frac{\mu_{agg}}{(\beta f_{cp}+f_{agg})\,\mu_{agg}+[f_{cp}\,(1-\beta)]\,\mu_{cp}} \end{aligned} \tag{3.22}$$

3.4 Traction vectors acting at aggregates' surfaces (observation scale B)

Inspired by the spatially constant stress and strain state in the inclusion of an Eshelby problem, we consider $\boldsymbol{\varepsilon}_{agg}$ and $\boldsymbol{\sigma}_{agg}$ from (3.14) and (3.20) to be – on average – representative for the strain and stress at any position inside the aggregates, including any positions adjacent to the surface of the

aggregate. Therefore, we may compute the traction vector acting on the surface of the aggregates by means of Cauchy's formula

$$\underline{T}_{agg}(\underline{x}) = \boldsymbol{\sigma}_{agg} \cdot \underline{n}(\underline{x}) \qquad \underline{x} \in \partial\Omega_{agg} \tag{3.23}$$

where $\underline{n}(\underline{x})$ denotes the unit outward normal vector at any point $\underline{x}$ on the surface of an aggregate grain.

3.5 Stress states in three-dimensional ITZs (observation scale B)

Herein, we provide the theoretical fundamentals allowing us to determine the full three-dimensional stress states within the ITZ shell, based on known stress and strain states within an aggregate sphere. This transition is possible because of perfect bond-related continuity conditions at the 2D interface $\mathcal{I}_{agg}^{ITZ}$ separating an aggregate from the surrounding three-dimensional ITZ.

A material interface represents a discontinuity in material stiffness ($\mathcal{I}_{agg}^{ITZ}$, for instance, separates an aggregate with stiffness $\mathbb{C}_{agg}$ from an ITZ with stiffness $\mathbb{C}_{ITZ}$) and this results, generally speaking, in discontinuous stress and strain fields across the interface. In case no atomic bonds exist between the two neighboring materials, they may part from each other, or they may slide along each other. In the former case, no continuity condition for stresses or displacements apply, but in the latter case, the principle of action and reaction allows for deriving stress transfer conditions and geometric conditions ensure that the two materials stay in contact but do not intersect each other. The here-considered perfect bond along $\mathcal{I}_{agg}^{ITZ}$, in turn, implies two specific types of continuity conditions described next. On the one hand, formulation of equilibrium of a three-dimensional body containing an arbitrary part of an aggregate, a part of the interface, as well as a part of the ITZ shell, and shrinking this body (in the sense of a mathematical limit procedure) to a two-dimensional domain on the interface, delivers the following stress continuity condition [29]

$$\boldsymbol{\sigma}_{agg}(\underline{x}) \cdot \underline{n}(\underline{x}) = \boldsymbol{\sigma}_{ITZ}(\underline{x}) \cdot \underline{n}(\underline{x}) \qquad \forall\ \underline{x} \in \mathcal{I}_{agg}^{ITZ} \tag{3.24}$$

On the other hand, continuity of displacement vectors $\underline{u}$ reading as

$$\underline{u}_{agg}(\underline{x}) = \underline{u}_{ITZ}(\underline{x}) \qquad \forall\ \underline{x} \in \mathcal{I}_{agg}^{ITZ} \tag{3.25}$$

requires continuity of the displacement vector field's tangential derivatives on $\mathcal{I}_{agg}^{ITZ}$, the so-called Hadamard compatibility relation [73]

$$\boldsymbol{\nabla}\underline{u}_{agg}(\underline{x}) \cdot \underline{t}(\underline{x}) = \boldsymbol{\nabla}\underline{u}_{ITZ}(\underline{x}) \cdot \underline{t}(\underline{x}) \qquad \forall\ \underline{x} \in \mathcal{I}_{agg}^{ITZ} \tag{3.26}$$

where $\underline{t}(\underline{x})$ denotes any possible tangent vector to $\mathcal{I}_{agg}^{ITZ}$ at position $\underline{x}$. Combination of (3.26) with the linear strain-displacement relation

$$\boldsymbol{\varepsilon} = \frac{1}{2}\left[\boldsymbol{\nabla}\underline{u} + (\boldsymbol{\nabla}\underline{u})^T\right] \tag{3.27}$$

allows for deriving strain continuity conditions. Eqs. (3.24)-(3.26) represent in total, six linearly

independent stress and strain conditions such that knowledge of $\boldsymbol{\sigma}_{agg}$ and $\boldsymbol{\varepsilon}_{agg}$ together with the ITZ elasticity law

$$\boldsymbol{\sigma}_{ITZ} = \mathbb{C}_{ITZ} : \boldsymbol{\varepsilon}_{ITZ} \tag{3.28}$$

allows for a component-wise reconstruction of the sought full three-dimensional stress state at any point of the ITZ which is adjacent to the interface. As for the related details, we have to introduce coordinate systems, and this will be done next.

3.6 Implementation based on a Cartesian and a spherical coordinate system

The macro-to-micro stress concentration described above is implemented next, based on an observing Cartesian coordinate system (with unit base vectors $\underline{e}_x$, $\underline{e}_y$, and $\underline{e}_z$) as well as spherical coordinates with unit base vectors $\underline{e}_\phi$, $\underline{e}_\theta$, and $\underline{e}_r$ forming a triad moving over the surface of an aggregate sphere, see Fig. 3.2. The zenith angle ϕ and the azimuth angle θ describe positions on this two-dimensional

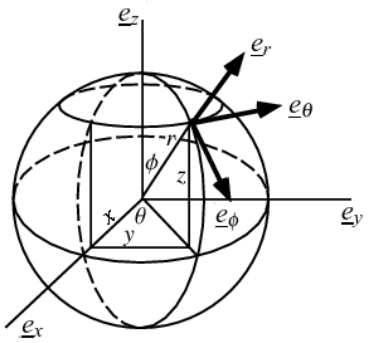

Figure 3.2: Spherical coordinates, from [85] with adapted notation

surface, r stands for the radial distance.

As for the macro-to-micro scale transition, Cartesian base frame is used, i.e. the 3×3 matrix representation of the second-order macrostress tensor reads as

$$\boldsymbol{\Sigma} = \begin{pmatrix} \Sigma_{xx} & \Sigma_{xy} & \Sigma_{xz} \\ \Sigma_{xy} & \Sigma_{yy} & \Sigma_{yz} \\ \Sigma_{xz} & \Sigma_{yz} & \Sigma_{zz} \end{pmatrix}_{\underline{e}_x, \underline{e}_y, \underline{e}_z} , \tag{3.29}$$

and specification of Eq. (3.18) for Eq. (3.29) delivers the aggregate strain components

$$\begin{aligned} \varepsilon_{agg,xx} =& 1/3 \left[(D_{vol} + 2D_{dev}) \Sigma_{xx} + (D_{vol} - D_{dev}) (\Sigma_{yy} + \Sigma_{zz}) \right] \\ \varepsilon_{agg,yy} =& 1/3 \left[(D_{vol} + 2D_{dev}) \Sigma_{yy} + (D_{vol} - D_{dev}) (\Sigma_{zz} + \Sigma_{xx}) \right] \\ \varepsilon_{agg,zz} =& 1/3 \left[(D_{vol} + 2D_{dev}) \Sigma_{zz} + (D_{vol} - D_{dev}) (\Sigma_{xx} + \Sigma_{yy}) \right] \\ \varepsilon_{agg,xy} =& D_{dev} \Sigma_{xy} \quad \varepsilon_{agg,xz} = D_{dev} \Sigma_{xz} \quad \varepsilon_{agg,yz} = D_{dev} \Sigma_{yz} \quad , \end{aligned} \tag{3.30}$$

see also Eqs. (3.19). In a similar way, we specify Eq. (3.21) for Eqs. (3.29), delivering the aggregate stress components as

$$\begin{aligned}
\sigma_{agg,xx} =& 1/3\ [(B_{vol} + 2B_{dev})\,\Sigma_{xx} + (B_{vol} - B_{dev})\,(\Sigma_{yy} + \Sigma_{zz})] \\
\sigma_{agg,yy} =& 1/3\ [(B_{vol} + 2B_{dev})\,\Sigma_{yy} + (B_{vol} - B_{dev})\,(\Sigma_{zz} + \Sigma_{xx})] \\
\sigma_{agg,zz} =& 1/3\ [(B_{vol} + 2B_{dev})\,\Sigma_{zz} + (B_{vol} - B_{dev})\,(\Sigma_{xx} + \Sigma_{yy})] \\
\sigma_{agg,xy} =& B_{dev}\Sigma_{xy} \quad \sigma_{agg,xz} = B_{dev}\Sigma_{xz} \quad \sigma_{agg,yz} = B_{dev}\Sigma_{yz} \quad ,
\end{aligned} \tag{3.31}$$

see also Eq. (3.22). In the context of traction vectors acting on aggregates' surfaces, we note that the local unit normal to any point of an aggregate sphere is the base vector $\underline{e}_r$, reading in Cartesian components:

$$\underline{n}(\phi,\theta) = \underline{e}_r(\phi,\theta) = \cos\theta\sin\phi\,\underline{e}_x + \sin\theta\sin\phi\,\underline{e}_y + \cos\theta\,\underline{e}_z \tag{3.32}$$

Specification of Cauchy's formula (3.23), for stress state (3.31) and normal vector (3.32) provides access to traction vectors acting on the aggregate's surface; notably, in Cartesian components $T_x(\phi,\theta)$, $T_y(\phi,\theta)$, and $T_z(\phi,\theta)$. In order to derive the local normal traction component $T_r(\phi,\theta)$ as well as the the shear components $T_\phi(\phi,\theta)$ and $T_\theta(\phi,\theta)$, transformation of the Cartesian components into local spherical coordinates is carried out, based on the transformation matrix $\boldsymbol{Q}(\phi,\theta)$

$$\begin{pmatrix} T_\phi \\ T_\theta \\ T_r \end{pmatrix} = \boldsymbol{Q}(\phi,\theta)\cdot \begin{pmatrix} T_x \\ T_y \\ T_z \end{pmatrix} \quad \text{with} \quad \boldsymbol{Q}(\phi,\theta) = \begin{pmatrix} \cos\theta\cos\phi & \sin\theta\cos\phi & -\sin\phi \\ -\sin\theta & \cos\theta & 0 \\ \cos\theta\sin\phi & \sin\theta\sin\phi & \cos\phi \end{pmatrix} . \tag{3.33}$$

This yields position-depended spherical components of the traction vector

$$\begin{aligned}
T_\phi(\phi,\theta) =& B_{dev}\Big[\frac{1}{2}\sin(2\phi)\left(\Sigma_{xx}\cos^2\theta + \Sigma_{yy}\sin^2\theta - \Sigma_{zz} + \Sigma_{xy}\sin(2\theta)\right) \\
&+ \left(2\cos^2\phi - 1\right)\left(\Sigma_{xz}\cos\theta + \Sigma_{yz}\sin\theta\right)\Big] \\
T_\theta(\phi,\theta) =& B_{dev}\Big[- \Sigma_{xz}\sin\theta\frac{1}{2}\left(-\Sigma_{xx} + \Sigma_{yy}\right)\sin(2\theta)\sin\phi \\
&+ \Sigma_{xy}\sin\phi\left(2\cos^2\theta - 1\right) + \cos\phi\left(-\Sigma_{xz}\sin\theta + \Sigma_{yz}\cos\theta\right)\Big] \\
T_r(\phi,\theta) =& \frac{1}{3}B_{vol}\left(\Sigma_{xx} + \Sigma_{yy} + \Sigma_{zz}\right) + B_{dev}\Big[\Sigma_{xx}\left(\cos^2\theta\sin^2\phi - \frac{1}{3}\right) + \Sigma_{yy}\left(\frac{2}{3} - \cos^2\phi\sin^2\theta - \cos^2\theta\right) \\
&+ \Sigma_{zz}\left(\cos^2\phi - \frac{1}{3}\right) + \Sigma_{xy}\sin(2\theta)\sin^2\phi + \Sigma_{xz}\sin(2\phi)\cos\theta + \Sigma_{yz}\sin(2\phi)\sin\theta\Big]
\end{aligned} \tag{3.34}$$

As for the stresses of the ITZ, comparison of Cauchy's formula (3.23) with stress continuity condition (3.24) allows for identifying that the normal stress component in r-direction, σ_{rr}, as well as the

shear stress components $\sigma_{\phi r}$ and $\sigma_{\theta r}$ are continuous across the interface $\mathcal{I}_{agg}^{ITZ}$, i.e.

$$\begin{aligned}\sigma_{ITZ,rr}(\phi,\theta) &= \sigma_{agg,rr}(\phi,\theta) = T_r(\phi,\theta)\\ \sigma_{ITZ,\phi r}(\phi,\theta) &= \sigma_{agg,\phi r}(\phi,\theta) = T_\phi(\phi,\theta)\\ \sigma_{ITZ,\theta r}(\phi,\theta) &= \sigma_{agg,\theta r}(\phi,\theta) = T_\theta(\phi,\theta)\,.\end{aligned} \tag{3.35}$$

When it comes to the displacement continuity condition (3.38), we note that all possible tangent vectors $\underline{t}$ at any position (ϕ,θ) of the interface $\mathcal{I}_{agg}^{ITZ}$ can be expressed as a linear combination of the local base vectors $\underline{e}_\phi$ and $\underline{e}_\theta$ (see Fig. 3.2)

$$\underline{t}(\phi,\theta) = c_1\underline{e}_\phi(\phi,\theta) + c_2\underline{e}_\theta(\phi,\theta) \qquad c_1,c_2\in\mathbb{R} \tag{3.36}$$

In this context, we recall that the matrix representation of the displacement gradient in spherical coordinates reads as [73]

$$\boldsymbol{\nabla}\underline{u} = \begin{pmatrix} \frac{1}{r}\left(\frac{\partial u_\phi}{\partial\phi}+u_r\right) & \frac{1}{r}\left(\frac{1}{\sin\phi}\frac{\partial u_\phi}{\partial\theta}+u_\theta\,\cot\phi\right) & \frac{\partial u_\phi}{\partial r}\\ \frac{1}{r}\frac{\partial u_\theta}{\partial\phi} & \frac{1}{r}\left(\frac{1}{\sin\phi}\frac{\partial u_\theta}{\partial\theta}+u_\phi\,\cot\phi+u_r\right) & \frac{\partial u_\theta}{\partial r}\\ \frac{1}{r}\left(\frac{\partial u_r}{\partial\phi}-u_\phi\right) & \frac{1}{r}\left(\frac{1}{\sin\phi}\frac{\partial u_r}{\partial\theta}-u_\theta\right) & \frac{\partial u_r}{\partial r}\end{pmatrix} \tag{3.37}$$

Combination of (3.26) with (3.36) and (3.37) implies that the components in the left two rows in (3.37) are continuous across $\mathcal{I}_{agg}^{ITZ}$ while the components in the right row will exhibit jumps, i.e. six out of nine components are continuous. This implies, under consideration of the strain-displacement relation (3.27), that the normal strain components both in ϕ and θ-direction as well as the shear strain component $\varepsilon_{\phi\theta}$ are continuous across the interface, i.e.

$$\begin{aligned}\varepsilon_{ITZ,\phi\phi}(\phi,\theta) &= \varepsilon_{agg,\phi\phi}(\phi,\theta)\\ \varepsilon_{ITZ,\theta\theta}(\phi,\theta) &= \varepsilon_{agg,\theta\theta}(\phi,\theta)\\ \varepsilon_{ITZ,\phi\theta}(\phi,\theta) &= \varepsilon_{agg,\phi\theta}(\phi,\theta)\,,\end{aligned} \tag{3.38}$$

whereby the aggregate strains follow from transforming the Cartesian components (3.30) into local spherical coordinates

$$\begin{pmatrix}\varepsilon_{agg,\phi\phi} & \varepsilon_{agg,\phi\theta} & \varepsilon_{agg,\phi r}\\ \varepsilon_{agg,\phi\theta} & \varepsilon_{agg,\theta\theta} & \varepsilon_{agg,\theta r}\\ \varepsilon_{agg,\phi r} & \varepsilon_{agg,\theta r} & \varepsilon_{agg,rr}\end{pmatrix} = \boldsymbol{Q}(\phi,\theta)\cdot\begin{pmatrix}\varepsilon_{agg,xx} & \varepsilon_{agg,xy} & \varepsilon_{agg,xz}\\ \varepsilon_{agg,xy} & \varepsilon_{agg,yy} & \varepsilon_{agg,yz}\\ \varepsilon_{agg,xy} & \varepsilon_{agg,yy} & \varepsilon_{agg,yz}\end{pmatrix}\cdot\boldsymbol{Q}^T(\phi,\theta)\,. \tag{3.39}$$

In Eq. (3.39), $\boldsymbol{Q}^T(\phi,\theta)$ stands for the transpose of $\boldsymbol{Q}(\phi,\theta)$ given in (3.33). Specification of (3.38) for

(3.39) and the resulting expression for (3.30) delivers the following ITZ strain components

$$\begin{aligned}
\varepsilon_{ITZ,\phi\phi}(\phi,\theta) &= \frac{1}{3}D_{vol}\left(\Sigma_{xx}+\Sigma_{yy}+\Sigma_{zz}\right) + D_{dev}\left[\Sigma_{xx}\left(\cos^2\phi\cos^2\theta-\frac{1}{3}\right)+\Sigma_{yy}\left(\cos^2\phi\sin^2\theta-\frac{1}{3}\right)\right.\\
&\quad \left.-\Sigma_{zz}\left(\cos^2\phi-\frac{2}{3}\right)+\Sigma_{xy}\cos^2\phi\sin(2\theta)-\sin(2\phi)\left(\Sigma_{xz}\cos\theta+\Sigma_{yz}\sin\theta\right)\right]\\
\varepsilon_{ITZ,\theta\theta}(\theta) &= \frac{1}{3}D_{vol}\left(\Sigma_{xx}+\Sigma_{yy}+\Sigma_{zz}\right)\\
&\quad + D_{dev}\left[\Sigma_{xx}\left(-\cos^2\theta+\frac{2}{3}\right)+\Sigma_{yy}\left(\cos^2\theta-\frac{1}{3}\right)-\frac{1}{3}\Sigma_{zz}-\Sigma_{xy}\sin(2\theta)\right]\\
\varepsilon_{ITZ,\phi\theta}(\phi,\theta) &= D_{dev}\left[\frac{1}{2}\left(-\Sigma_{xx}+\Sigma_{yy}\right)\sin(2\theta)\cos\phi+\Sigma_{xy}\cos\phi\left(2\cos^2\theta-1\right)\right.\\
&\quad \left.+\sin\phi\left(\Sigma_{xz}\sin\theta-\Sigma_{yz}\cos\theta\right)\right]
\end{aligned} \tag{3.40}$$

Conclusively, consideration of equilibrium and of kinematic continuity at the interface $\mathcal{I}_{agg}^{ITZ}$ enabled us to calculate three stress and three strain components of the ITZ. The remaining stress and strain components can be determined from the isotropic elasticity law, see (3.28), which reads, in compressed notation (according to Kelvin [71, 24]) as

$$\begin{pmatrix}\sigma_{ITZ,\phi\phi}\\ \sigma_{ITZ,\theta\theta}\\ \sigma_{ITZ,rr}\\ \sqrt{2}\sigma_{ITZ,\theta r}\\ \sqrt{2}\sigma_{ITZ,\phi r}\\ \sqrt{2}\sigma_{ITZ,\phi\theta}\end{pmatrix} = \begin{pmatrix} k_{ITZ}+\frac{4}{3}\mu_{ITZ} & k_{ITZ}-\frac{2}{3}\mu_{ITZ} & k_{ITZ}-\frac{2}{3}\mu_{ITZ} & 0 & 0 & 0\\ & k_{ITZ}+\frac{4}{3}\mu_{ITZ} & k_{ITZ}-\frac{2}{3}\mu_{ITZ} & 0 & 0 & 0\\ & & k_{ITZ}+\frac{4}{3}\mu_{ITZ} & 0 & 0 & 0\\ \vdots & & & 2\mu_{ITZ} & 0 & 0\\ & & & & 2\mu_{ITZ} & 0\\ \text{symm} & & \cdots & & & 2\mu_{ITZ}\end{pmatrix} \cdot \begin{pmatrix}\varepsilon_{ITZ,\phi\phi}\\ \varepsilon_{ITZ,\theta\theta}\\ \varepsilon_{ITZ,rr}\\ \sqrt{2}\varepsilon_{ITZ,\theta r}\\ \sqrt{2}\varepsilon_{ITZ,\phi r}\\ \sqrt{2}\varepsilon_{ITZ,\phi\theta}\end{pmatrix} \tag{3.41}$$

where k_{ITZ} and μ_{ITZ} denote the bulk and shear modulus of the ITZ, respectively. For the sake of conciseness, we omit the argument (ϕ,θ) for all stress and strain components. The last three lines of (3.41) imply that $\varepsilon_{ITZ,\theta r}$, $\varepsilon_{ITZ,\phi r}$, and $\sigma_{ITZ,\phi\theta}$ follow as

$$\varepsilon_{ITZ,\theta r} = \frac{1}{2\mu_{ITZ}}\,\sigma_{ITZ,\theta r}\,, \qquad \varepsilon_{ITZ,\phi r} = \frac{1}{2\mu_{ITZ}}\,\sigma_{ITZ,\phi r}\,, \quad \text{and} \quad \sigma_{ITZ,\phi\theta} = 2\mu_{ITZ}\,\varepsilon_{ITZ,\phi\theta}\,. \tag{3.42}$$

The first three lines of (3.41), in turn, can be solved for the sought normal components $\sigma_{ITZ,\phi\phi}$, $\sigma_{ITZ,\theta\theta}$, and $\varepsilon_{ITZ,rr}$:

$$\begin{aligned}
\sigma_{ITZ,\phi\phi} &= \frac{4\mu_{ITZ}(2k_{ITZ}+\mu_{ITZ})\varepsilon_{ITZ,\phi\phi}+(3k_{ITZ}-2\mu_{ITZ})(2\mu_{ITZ}\varepsilon_{ITZ,\theta\theta}+\sigma_{ITZ,rr})}{3k_{ITZ}+4\mu_{ITZ}}\,,\\
\sigma_{ITZ,\theta\theta} &= \frac{4\mu_{ITZ}(2k_{ITZ}+\mu_{ITZ})\varepsilon_{ITZ,\theta\theta}+(3k_{ITZ}-2\mu_{ITZ})(2\mu_{ITZ}\varepsilon_{ITZ,\phi\phi}+\sigma_{ITZ,rr})}{3k_{ITZ}+4\mu_{ITZ}}\,,\\
\varepsilon_{ITZ,rr} &= \frac{3\sigma_{ITZ,rr}-(3k_{ITZ}-2\mu_{ITZ})(\varepsilon_{ITZ,\phi\phi}+\varepsilon_{ITZ,\theta\theta})}{3k_{ITZ}+4\mu_{ITZ}}
\end{aligned} \tag{3.43}$$

Specification of Eqs. (3.42) and (3.43) for the continuous stress and strain components given in (3.35), (3.34), and (3.38) delivers expressions for the six sought components of ITZ stresses and strains exhibiting jumps across $\mathcal{I}_{agg}^{ITZ}$, such that the complete three-dimensional stress and strain states within the ITZ are determined.

3.7 Microscopic stress states under macroscopic uniaxial loading

In the sequel, we illustrate the results described so far by considering an RVE of concrete which is subjected to a macroscopic uniaxial stress state in z-direction

$$\boldsymbol{\Sigma} = \Sigma_{zz}\, \underline{e}_z \otimes \underline{e}_z \,, \tag{3.44}$$

and by comparing components of aggregate stresses $\boldsymbol{\sigma}_{agg}$, traction vectors acting on the aggregate's surface $\mathcal{I}_{agg}^{ITZ}$, and ITZ stresses $\boldsymbol{\sigma}_{ITZ}$, as a function of the spherical coordinates ϕ and θ, see Fig. 3.2. Because of the axial symmetry of this problem with respect to the z-axis, (i) microscopic stress fields are constant along the circumferential direction θ, i.e. they only depend on the longitudinal direction ϕ, and (ii), the following shear stress components vanish:

$$\sigma_{agg,\phi\theta} = \sigma_{ITZ,\phi\theta} = \sigma_{agg,\theta r} = \sigma_{ITZ,\theta r} = T_\theta \tag{3.45}$$

As for the aggregate stresses, we transform their Cartesian components (3.31) by analogy to the strain transformation given in (3.39), and with the transformation matrix $\boldsymbol{Q}$ from (3.33), into spherical stress components. Specification of the resulting expressions for macroscopic uniaxial loading (3.44) delivers, in dimensionless form, the following non-vanishing components

$$\begin{aligned}
\frac{\sigma_{agg,\phi\phi}(\phi)}{\Sigma_{zz}} &= \frac{1}{3}B_{vol} + B_{dev}\left(\frac{2}{3} - \cos^2\phi\right) \\
\frac{\sigma_{agg,\theta\theta}(\phi)}{\Sigma_{zz}} &= \frac{1}{3}\left(B_{vol} - B_{dev}\right) \\
\frac{\sigma_{agg,rr}(\phi)}{\Sigma_{zz}} &= \frac{1}{3}B_{vol} + B_{dev}\left(\cos^2\phi - \frac{1}{3}\right) \\
\frac{\sigma_{agg,\phi r}(\phi)}{\Sigma_{zz}} &= -\frac{1}{2}B_{dev}\sin(2\phi)\,,
\end{aligned} \tag{3.46}$$

with B_{vol} and B_{dev} given in (3.22).

Non-zero spherical components of traction vectors acting on the aggregate's surface follow from specification of the general expressions (3.34) for macroscopic uniaxial loading (3.44). They read, in dimensionless form, as

$$\begin{aligned}
\frac{T_\phi(\phi)}{\Sigma_{zz}} &= -\frac{1}{2}B_{dev}\sin(2\phi) \\
\frac{T_r(\phi)}{\Sigma_{zz}} &= \frac{1}{3}B_{vol} + B_{dev}\left(\cos^2\phi - \frac{1}{3}\right)\,.
\end{aligned} \tag{3.47}$$

Non-zero spherical components of ITZ stresses follow, on the one hand, from (3.47) under consid-

eration of (3.34) and, on the other hand, from $(3.42)_3$ and $(3.43)_{1,2}$ under consideration of (3.40) and uniaxial loading (3.44), they read, in dimensionless form, as

$$\begin{aligned}
\frac{\sigma_{ITZ,\phi\phi}(\phi)}{\Sigma_{zz}} &= \frac{1}{(9k_{ITZ}+12\mu_{ITZ})}\Big\{B_{dev}\left[\cos^2\phi\,(9k_{ITZ}-6\mu_{ITZ})-3k_{ITZ}+2\mu_{ITZ}\right] \\
&\quad + B_{vol}\,(3k_{ITZ}-2\mu_{ITZ}) + 4D_{dev}\mu_{ITZ}\left[-3\cos^2\phi\,(3k_{ITZ}+\mu_{ITZ})+2\mu_{ITZ}-6k_{ITZ}\right] \\
&\quad + 4D_{vol}\mu_{ITZ}\,(3k_{ITZ}+\mu_{ITZ})\Big\} \\
\frac{\sigma_{ITZ,\theta\theta}(\phi)}{\Sigma_{zz}} &= \frac{1}{(9k_{ITZ}+12\mu_{ITZ})}\Big\{B_{dev}\left[\cos^2\phi\,(9k_{ITZ}-6\mu_{ITZ})-3k_{ITZ}+2\mu_{ITZ}\right] \\
&\quad + B_{vol}\,(3k_{ITZ}-2\mu_{ITZ}) + 6D_{dev}\mu_{ITZ}\left[-\cos^2\phi\,(3k_{ITZ}-2\mu_{ITZ})-2\mu_{ITZ}\right] \\
&\quad + 4D_{vol}\mu_{ITZ}\,(3k_{ITZ}+\mu_{ITZ})\Big\} \\
\frac{\sigma_{ITZ,rr}(\phi)}{\Sigma_{zz}} &= \frac{1}{3}B_{vol} + B_{dev}\left(\cos^2\phi-\frac{1}{3}\right) \\
\frac{\sigma_{ITZ,\phi r}(\phi)}{\Sigma_{zz}} &= -\frac{1}{2}B_{dev}\sin(2\phi)\,,
\end{aligned} \tag{3.48}$$

with B_{vol}, B_{dev}, D_{vol}, and D_{dev} from (3.22) and (3.19).

Next, we evaluate Eqs. (3.46), (3.47), and (3.48) for a typical concrete. In more detail, we consider an initial water-to-cement mass ratio of $w/c = 0.5$, a hydration degree close to completed hydration (95 %), and a concrete-related volume fraction of quartz aggregates, being equal to 65 %:

$$f_{agg} = 0.65 \qquad f_{cp} = 1 - f_{agg} = 0.35 \tag{3.49}$$

The elastic properties, in terms of Young's modulus E and Poisson's ratio ν, of quartz read as [11]

$$E_{agg} = 96\ \text{GPa} \qquad \nu_{agg} = 0.08\,. \tag{3.50}$$

The ones of cement paste are estimated by the validated continuum micromechanics-model of [68]:

$$E_{cp} = 16\ \text{GPa} \qquad \nu_{cp} = 0.23\,. \tag{3.51}$$

The Young's modulus of the ITZ is considered to amount to 85 % to the Young's modulus of the bulk cement paste:

$$E_{ITZ} = 13.6\ \text{GPa} \qquad \nu_{ITZ} = 0.23\,. \tag{3.52}$$

The choice $\nu_{ITZ} = \nu_{cp}$ is motivated by the fact that the (drained) Poisson's ratio of cement paste is – in good approximation – constant with respect to the composition-related initial water-to-cement mass ratio and to the maturity-related hydration degree [69]. Microscopic stresses (3.46), (3.47), and (3.48) evaluated for the described elastic properties are not only valid for the described concrete, but a dimensional analysis [10] (see Appendix D for details) implies that the evaluations are valid for any

set of elastic properties satisfying

$$\frac{E_{agg}}{E_{cp}} = 6\,, \quad \frac{E_{ITZ}}{E_{cp}} = 0.85\,, \quad \nu_{agg} = 0.08 \quad \nu_{cp} = \nu_{ITZ} = 0.23\,, \quad f_{agg} = 0.65\,. \tag{3.53}$$

Notably, Young's modulus and Poisson's ratio given above can be easily converted into bulk moduli, and shear moduli, based on standard relations of isotropic materials [73]:

$$k_j = \frac{E_j}{3\,(1-2\,\nu_j)}\,, \qquad \mu_j = \frac{E_j}{2\,(1+\nu_j)}\,, \qquad \forall j \in \{agg, cp, ITZ\}\,. \tag{3.54}$$

Specification of Eqs. (3.46) and (3.48) for Eqs. (3.22), (3.19), (3.11), and of the resulting expressions for (3.54) and (3.53) results in normal stress components which are symmetric with respect to $\phi = \pi/2$, and in the shear components which are antimetric with respect to $\phi = \pi/2$, see Fig. 3.3. They are

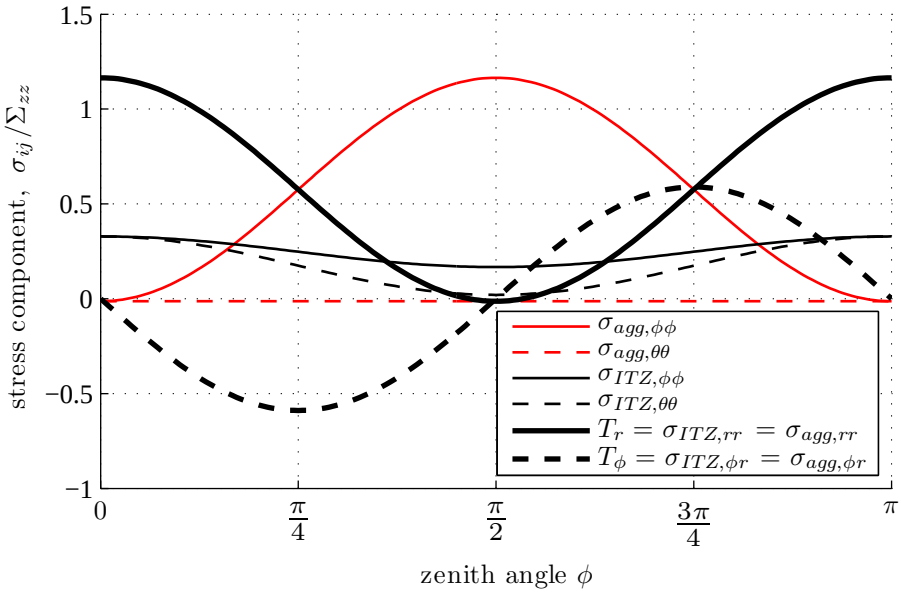

Figure 3.3: Dimensionless, nonzero microscopic stress components as a function of zenith angle: aggregate stresses, traction vector components acting on the aggregate's surface, and ITZ stresses, respectively, under uniaxial loading (3.44), evaluated for elastic properties and aggregate content described in (3.53), see also (3.22), (3.11), and (3.54)

discussed in more detail next:

- Aggregate normal stresses aligned with the direction of RVE loading are by a factor of 1.165 larger than the macroscopically imposed stress intensity Σ_{zz}, see $\sigma_{agg,rr}$ at the poles (i.e. at $\phi = 0$ and $\phi = \pi$, respectively) as well as $\sigma_{agg,\phi\phi}$ at the equator (i.e. at $\phi = \pi/2$). This stress amplification is a result of the statically indeterminate nature of the microstructure of concrete,

which implies that stiffer microstructural components (the aggregates) take over a larger share of the load than more compliant components (the cement paste matrix).

- At the poles, the normal stresses $\sigma_{agg,rr}$ are transferred over the two-dimensional aggregate-ITZ interface to the ITZ, because of the equilibrium-related stress continuity condition (3.24). This implies that – under macroscopic uniaxial tension – both the aggregate-ITZ interface and the bulk ITZ are subjected to a larger tensile normal stresses than the one imposed on the concrete RVE.

- At the equator, the aggregates, aggregate-ITZ interfaces, and bulk ITZs exhibit normal stresses in radial direction, the sign of which is different from the one of the macroloading, see $\sigma_{agg,rr} = T_r = \sigma_{ITZ,rr} = -0.01346\,\Sigma_{zz}$ at $\phi = \pi/2$. In other words, under macroscopic uniaxial compression, the described microscopic normal stresses (acting perpendicular to the direction of macroscopic loading) are tensile.

- Stress jumps across the aggregate-ITZ interface concern normal stresses acting in the tangential plane of every interface point, see the difference between $\sigma_{agg,\phi\phi}$ and $\sigma_{ITZ,\phi\phi}$ as well as between $\sigma_{agg,\theta\theta}$ and $\sigma_{ITZ,\theta\theta}$. While these ITZ stresses range in the interval $[+0.02034\,,+0.3285]\,\Sigma_{zz}$, these aggregate stresses range in the interval $[-0.01346\,,+1.164]\,\Sigma_{zz}$. This stems from the difference in elastic properties of aggregates and the bulk ITZ.

- Shear stresses $\sigma_{agg,r\phi} = T_\phi = \sigma_{ITZ,r\phi}$ vanish only at the poles and at the equator, and they exhibit extreme values amounting to $\mp 0.5892\,\Sigma_{zz}$ at the positions $\phi = \pi/4$ and $\phi = 3\,\pi/4$, respectively. Together with (3.45) this implies that the normal stress component in circumferential θ-direction represents a principal stress component. The normal stresses $\sigma_{ITZ,rr}$ and $\sigma_{ITZ,\phi\phi}$, however, are principal stresses only at the poles and at the equator. In between, the principal stress directions in the local ϕ-r planes deviate from the radial and the longitudinal direction.

For the illustration of microscopic strains resulting from macroscopic uniaxial loading see Appendix B. Therein, symmetric biaxial macroscopic loading is also discussed.

Chapter 4

Upscaling of tensile strength criteria to describe onset of debonding and onset of ITZ failure

Post-failure fragments from laboratory concrete specimens exhibit regions where aggregates are clearly separated from the surrounding binder matrix and other regions where thin deposits of the binder material remain on the surface of the aggregate. The precise spatial location at which the first microcrack nucleated cannot be back-analyzed from such post-failure observations.

The described experimental observations provides us with the motivation to investigate potential and limitation of two different tensile strength criteria for onset of concrete cracking: clean aggregate debonding and failure in the bulk of the three-dimensional ITZ shell. In both cases, we perform elastic limit analyzes, in the framework of an elasto-brittle approach. In more detail, we consider perfect bond in all observation-scale specific interfaces, and we envision that the aggregate-ITZ interface and the bulk ITZ, respectively, remain intact as long as related tensile stresses remain below corresponding strength values. Reaching the latter, in turn, is considered to be associated with onset of (micro)cracking of concrete. Since this microscopic failure mode is not necessarily related to the overall load carrying capacity of the concrete RVE, our analysis delivers macroscopic load intensities at which microcracking-related pre-peak nonlinearities in the macroscopic stress-strain relation of concrete start to appear.

4.1 Microscopic tensile strength criteria

"Aggregate debonding" refers to onset of crack propagation along the two-dimensional interface $\mathcal{I}_{agg}^{ITZ}$ which is separating the aggregate from the three-dimensional ITZ shell. In this context, we assume that the perfect bond established by the interface remains intact as long as the maximum normal traction T_r remains below a related tensile strength value T_r^{ult}, and that onset of cracking is assumed

once the former quantity reaches the latter one. This is reflected by the following failure function

$$f_{\mathcal{I}_{agg}^{ITZ}}(\boldsymbol{\Sigma}) = \max_{\phi,\theta} T_r(\boldsymbol{\Sigma},\phi,\theta) - T_r^{ult} \leq 0 \tag{4.1}$$

see $(3.34)_3$ for an analytical expression of the $T_r(\boldsymbol{\Sigma},\phi,\theta)$. Macroscopic stress states $\boldsymbol{\Sigma}$ under which the interface establishes perfect bond between the aggregates and the ITZ are characterized by $f_{\mathcal{I}_{agg}^{ITZ}}(\boldsymbol{\Sigma}) < 0$, and onset of aggregate debonding is associated with $f_{\mathcal{I}_{agg}^{ITZ}}(\boldsymbol{\Sigma}) = 0$.

"ITZ failure" refers to tension-induced cracking of the most heavily loaded RVE within the three-dimensional ITZ shell. In this context, we introduce a Rankine-type failure function, i.e. an RVE of the ITZ is considered to remain intact as long as the maximum principal stress $\sigma_{ITZ,I}$ remains below a tensile strength value σ_{ITZ}^{ult}, and onset of cracking is envisioned once the former quantity reaches the latter one. This is reflected by the following failure function

$$f_{ITZ}(\boldsymbol{\Sigma}) = \max_{\phi,\theta} \sigma_I(\boldsymbol{\Sigma},\phi,\theta) - \sigma_{ITZ}^{ult} \leq 0 \tag{4.2}$$

Macroscopic stress states $\boldsymbol{\Sigma}$ under which the entire ITZ shell remains intact are characterized by $f_{ITZ}(\boldsymbol{\Sigma}) < 0$, and onset of ITZ failure is associated with $f_{ITZ}(\boldsymbol{\Sigma}) = 0$.

4.2 Performance of the aggregate debonding criterion

Herein, we upscale the aggregate debonding criterion (4.1) to the material scale of concrete in order to link onset of debonding to corresponding macroscopic stress intensities, and to determine the exact position (in terms of position angles ϕ and θ) where criterion (4.1) foresees this beginning debonding process.

4.2.1 Macroscopic uniaxial tension and compression

The radial normal traction components acting in the aggregate-ITZ interface $\mathcal{I}_{agg}^{ITZ}$ are given, for macroscopic uniaxial loading in z-direction (3.44), in $(3.46)_3$ and read as

$$T_r(\phi) = \Sigma_{zz}\left[\frac{1}{3}B_{vol} + B_{dev}\left(\cos^2\phi - \frac{1}{3}\right)\right]. \tag{4.3}$$

Under uniaxial tension ($\Sigma_{zz} > 0$), the maximum normal traction, $\max_{\phi,\theta} T_r(\boldsymbol{\Sigma},\phi,\theta)$, is located at the pole ($\phi = 0$), and amounts to

$$\max_{\phi,\theta} T_r(\boldsymbol{\Sigma},\phi,\theta) = T_r(\boldsymbol{\Sigma},\phi=0,\theta) = \frac{1}{3}\Sigma_{zz}\left(B_{vol} + 2\,B_{dev}\right) \qquad \Sigma_{zz} > 0\,. \tag{4.4}$$

Under uniaxial compression ($\Sigma_{zz} < 0$), the maximum of T_r occurs at the equator ($\phi = \pi/2$) and amounts to

$$\max_{\phi,\theta} T_r(\boldsymbol{\Sigma},\phi,\theta) = T_r(\boldsymbol{\Sigma},\phi=\pi/2,\theta) = \frac{1}{3}\Sigma_{zz}\left(B_{vol} - B_{dev}\right) \qquad \Sigma_{zz} < 0,. \tag{4.5}$$

This implies that the onset of debonding is predicted to start at the pole (under uniaxial tension) or the equator (under uniaxial compression). Related values of the prescribed macrostress refer to macroscopic elastic limits and they are denoted as Σ_{tu}^{lim} and Σ_{cu}^{lim} (where indexes "tu" stand for uniaxial tension and "cu" denotes uniaxial compression). They follow from specification of criterion (4.1) for (4.4) and (4.5), respectively, from considering the limit state $f_{\mathcal{I}_{agg}^{ITZ}} = 0$, and from solving the resulting expressions for Σ_{zz}:

$$\Sigma_{tu}^{lim} = \frac{3T_r^{ult}}{B_{vol} + 2\,B_{dev}} \qquad \Sigma_{cu}^{lim} = \frac{3T_r^{ult}}{B_{vol} - B_{dev}} \tag{4.6}$$

From (4.6) it follows that criterion (4.1) is only able to predict tension-driven debonding under uniaxial compression if $B_{vol} < B_{dev}$, see (3.22). Otherwise the radial normal traction component is compressive all over the aggregate sphere such that tensile debonding is impossible. When considering elastic properties of aggregates and cement paste according to (3.50) and (3.51) as well as an aggregate dosage of 65%, see (3.49), specification of (4.6) for (3.22), (3.11), and (3.54) delivers

$$\frac{\Sigma_{tu}^{lim}}{T_r^{ult}} = +0.8585 \qquad \frac{\Sigma_{cu}^{lim}}{T_r^{ult}} = -74.29 \tag{4.7}$$

4.2.2 Macroscopic biaxial loading

Herein, we study debonding under macroscopic biaxial loading:

$$\boldsymbol{\Sigma} = \Sigma_{xx}\,\underline{e}_x \otimes \underline{e}_x + \Sigma_{yy}\,\underline{e}_y \otimes \underline{e}_y\,. \tag{4.8}$$

To this end, we specify the normal tractions $(3.34)_3$ for (4.8), yielding

$$T_r(\boldsymbol{\Sigma},\phi,\theta) = \frac{1}{3}B_{vol}\,(\Sigma_{xx}+\Sigma_{yy}) + B_{dev}\left[\Sigma_{xx}\left(\cos^2\theta\sin^2\phi - \frac{1}{3}\right) + \Sigma_{yy}\left(\frac{2}{3} - \cos^2\phi\sin^2\theta - \cos^2\theta\right)\right]. \tag{4.9}$$

Determination of maximum normal tractions $\max_{\phi,\theta} T_r(\boldsymbol{\Sigma},\phi,\theta)$ for arbitrary values of Σ_{xx} and Σ_{yy} is a surprisingly challenging mathematical task. Based on the results obtained for uniaxial macroscopic loading (see above) and consideration of the validity of the superposition principle, however, allows for straightforward determination of the position where the maximum radial normal stress T_r is induced. Assuming that both macroscopic stress components are compressive ($\Sigma_{xx} < 0$, $\Sigma_{yy} < 0$), the biaxial loading scenario is considered to be a superposition of two load cases, namely uniaxial compression in x-direction ($\Sigma_{xx} < 0$ and $\Sigma_{yy} = 0$) as well as uniaxial compression in y-direction ($\Sigma_{xx} = 0$, $\Sigma_{yy} < 0$). In the first load case, maximum tensile normal stresses T_r occur at the intersection of the aggregate's surface with the y,z-plane (i.e. at the great circle defined through $\phi \in [0, 2\pi]$ and $\theta = \pi/2$). Similarly, in the second loading case, maximum tensile normal stresses T_r occur at the intersection of the aggregate's surface with the x,z-plane (i.e. at the great circle defined through $\phi \in [0, 2\pi]$ and $\theta = 0$). The tensile normal stresses of both loading cases augment each other at the position where the x,z-plane, the y,z-plane, and aggregate's surface intersect, i.e. at the poles $\phi = 0$ and $\phi = \pi$. Notably, the values of T_r at the two poles are equal due to symmetry conditions. Specification of (4.9)

for $\phi = 0$ and consideration of $\sin^2\theta + \cos^2\theta = 1$ delivers

$$\max_{\phi,\theta} T_r(\mathbf{\Sigma}, \phi, \theta) = T_r(\mathbf{\Sigma}, \phi = 0, \theta) = \frac{1}{3}\left(B_{vol} - B_{dev}\right)\left(\Sigma_{xx} + \Sigma_{yy}\right) \qquad \Sigma_{xx} < 0,\, \Sigma_{yy} < 0\,. \tag{4.10}$$

If Σ_{xx} is tensile ($\Sigma_{xx} > 0$) and larger than Σ_{yy} ($\Sigma_{xx} > \Sigma_{yy}$), again a load case decomposition is considered. The maximum normal stress T_r resulting from governing uniaxial tension $\Sigma_{xx} > 0$ occurs at the intersection of the equator with the x-axis, i.e. at the points ($\phi = \pi/2,\ \theta = 0$) as well as ($\phi = \pi/2,\ \theta = \pi$). As for the superposition of the second load case, no matter whether Σ_{yy} is tensile or compressive, the location of the maximum normal traction does not change. Specification of (4.9) for $\phi = \pi/2$ and $\theta = 0$ delivers

$$\max_{\phi,\theta} T_r(\mathbf{\Sigma}, \phi, \theta) = T_r(\mathbf{\Sigma}, \phi = \frac{\pi}{2}, \theta = 0) = \frac{1}{3}\left[B_{vol}\left(\Sigma_{xx} + \Sigma_{yy}\right) + B_{dev}\left(2\Sigma_{xx} - \Sigma_{yy}\right)\right] \qquad \Sigma_{xx} > 0,\, \Sigma_{xx} > \Sigma_{yy}\,. \tag{4.11}$$

Similarly, for $\Sigma_{yy} > 0$ and $\Sigma_{yy} > \Sigma_{xx}$ the maximum normal traction is obtained as

$$\max_{\phi,\theta} T_r(\mathbf{\Sigma}, \phi, \theta) = T_r(\mathbf{\Sigma}, \phi = \frac{\pi}{2}, \theta = \frac{\pi}{2}) = \frac{1}{3}\left[B_{vol}\left(\Sigma_{xx} + \Sigma_{yy}\right) + B_{dev}\left(-\Sigma_{xx} + 2\Sigma_{yy}\right)\right] \qquad \Sigma_{yy} > 0,\, \Sigma_{yy} > \Sigma_{xx}\,. \tag{4.12}$$

Elastic limit-related normal stress intensities Σ_{xx}^{lim} and Σ_{yy}^{lim} follow from specification of the debonding criterion (4.1) for the case-specific maximum normal tractions (4.10)-(4.12), and from considering the limit state $f_{\mathcal{I}_{agg}^{ITZ}} = 0$ as

$$\begin{aligned}
\left(\Sigma_{xx}^{lim} + \Sigma_{yy}^{lim}\right)\left(B_{vol} - B_{dev}\right) &= 3\,T_r^{ult} \qquad && \Sigma_{xx}^{lim} < 0,\, \Sigma_{yy}^{lim} < 0 \\
\Sigma_{xx}^{lim}\left(B_{vol} + 2B_{dev}\right) + \Sigma_{yy}^{lim}\left(B_{vol} - B_{dev}\right) &= 3\,T_r^{ult} \qquad && \Sigma_{xx}^{lim} > 0,\, \Sigma_{xx}^{lim} > \Sigma_{yy}^{lim} \\
\Sigma_{xx}^{lim}\left(B_{vol} - B_{dev}\right) + \Sigma_{yy}^{lim}\left(B_{vol} + 2B_{dev}\right) &= 3\,T_r^{ult} \qquad && \Sigma_{yy}^{lim} > 0,\, \Sigma_{yy}^{lim} > \Sigma_{xx}^{lim}
\end{aligned} \tag{4.13}$$

Eqs. (4.13) represent three straight lines in macroscopic biaxial stress space, forming a symmetric (with respect to the first meridian), triangular envelope, see Fig. 4.1. Stress states within the elastic limit envelope are elastic (all bonds remain intact), while stress states on the elastic limit envelopes result in onset of debonding at the indicated positions.

In the case of symmetric biaxial loading, $\Sigma_{xx} = \Sigma_{yy}$, (4.9) leads, under consideration of theorems for trigonometric functions, to

$$T_r(\mathbf{\Sigma}, \phi) = \Sigma_{xx}\left[\frac{2}{3}B_{vol} + B_{dev}\left(\frac{1}{3} - \cos^2\phi\right)\right]\,, \tag{4.14}$$

which clearly is independent of the azimuth angle. Maxima of (4.14) occur at the equator for symmetric biaxial tension ($\Sigma_{xx} = \Sigma_{yy} > 0$) and at the pole for symmetric biaxial compression ($\Sigma_{xx} = \Sigma_{yy} < 0$). The latter maximum refers to tensile normal tractions only if $B_{vol} < B_{dev}$. Hence, related macroscopic elastic limits under symmetric biaxial compression Σ_{cb}^{lim} follow from specification of (4.14) for $\phi = 0$

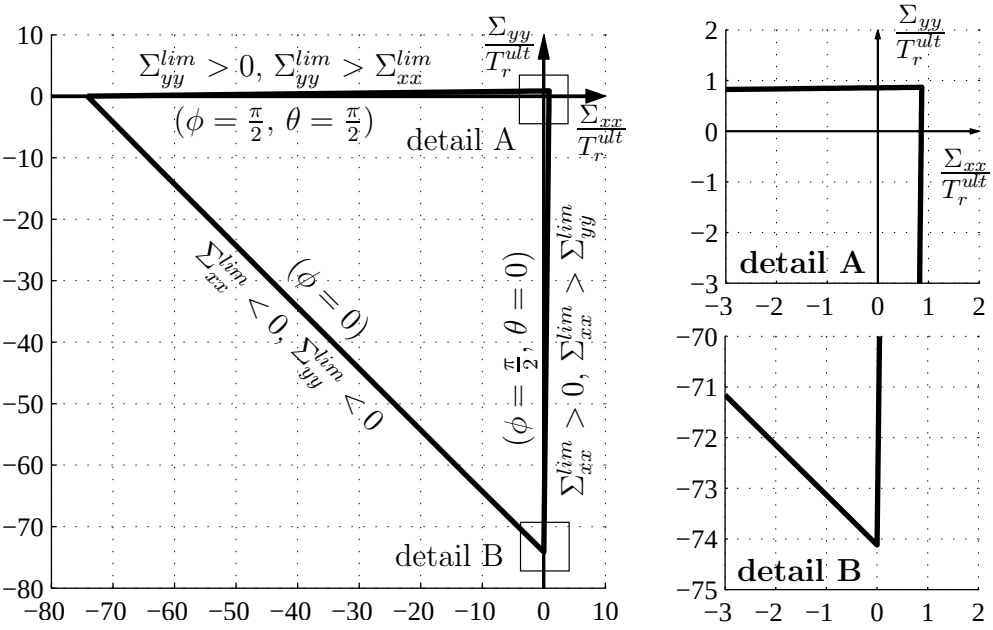

Figure 4.1: Debonding-related elastic limit envelope for macroscopic biaxial loading $\boldsymbol{\Sigma} = \Sigma_{xx}\,\underline{e}_x \otimes \underline{e}_x + \Sigma_{yy}\,\underline{e}_y \otimes \underline{e}_y$: evaluation of debonding relation (4.13) for concrete properties listed in (3.53), see also (3.22), (3.11), and (3.54); in brackets: position at aggregate sphere where debonding starts

and insertion of the resulting expression into the debonding criterion (4.1). Similarly, macroscopic elastic limits under symmetric biaxial tension Σ_{tb}^{lim} follow from specification of (4.14) for $\phi = \pi/2$ and insertion of the resulting expression into the debonding criterion (4.1). Consideration of elastic properties of aggregates and cement paste according to (3.50) and (3.51) as well as of an aggregate dosage of 65%, see (3.49), specification of the resulting expressions for (3.22), (3.11), and (3.54) delivers symmetric biaxial elastic limit-related macroscopic stress intensities, reading as

$$\frac{\Sigma_{tb}^{lim}}{T_r^{ult}} = +0.8685 \qquad \frac{\Sigma_{cb}^{lim}}{T_r^{ult}} = -37.14\,. \tag{4.15}$$

The elastic limit of symmetric biaxial compression, amounts to exactly one half of the corresponding value under uniaxial compression, and the elastic limit of symmetric biaxial tension is only a little larger than under uniaxial tension, due to linear functions (4.13), compare (4.15) and (4.7).

4.2.3 General three-dimensional macroscopic stress states

Here, we consider general triaxial macroscopic loading in terms of principal stresses Σ_{xx}, Σ_{yy}, and Σ_{zz} acting in the principal directions $\underline{e}_x$, $\underline{e}_y$, and $\underline{e}_z$, imposed on an RVE of concrete

$$\boldsymbol{\Sigma} = \Sigma_{xx}\,\underline{e}_x \otimes \underline{e}_x + \Sigma_{yy}\,\underline{e}_y \otimes \underline{e}_y + \Sigma_{zz}\,\underline{e}_z \otimes \underline{e}_z\,, \tag{4.16}$$

Because the concrete is isotropic, any general three-dimensional type of loading may be represented by (4.16). The normal traction field acting on the aggregate's surface follows from specification of $(3.34)_3$ for $\Sigma_{xy} = \Sigma_{yz} = \Sigma_{xz} = 0$ as

$$\begin{aligned} T_r(\boldsymbol{\Sigma}, \phi, \theta) =& \frac{1}{3} B_{vol} \left(\Sigma_{xx} + \Sigma_{yy} + \Sigma_{zz}\right) + B_{dev} \left[\Sigma_{xx} \left(\cos^2\theta \sin^2\phi - \frac{1}{3} \right) \right. \\ & \left. + \Sigma_{yy} \left(\frac{2}{3} - \cos^2\phi \sin^2\theta - \cos^2\theta \right) + \Sigma_{zz} \left(\cos^2\phi - \frac{1}{3} \right) \right], \end{aligned} \tag{4.17}$$

Considering the macroscopic stress state (4.16) as the superposition of three uniaxial load cases, and based on the same line of argumentation as used for biaxial macroscopic loading, only three positions on the aggregate's surface are candidates for the global maximum $\max_{\phi,\theta} T_r(\boldsymbol{\Sigma}, \phi, \theta)$, namely the pole ($\phi = 0$), the intersection of the equator with the x-axis ($\phi = \pi/2$, $\theta = 0$), and the intersection of the equator with the y-axis ($\phi = \pi/2$, $\theta = \pi/2$). The first position is relevant, if Σ_{zz} is the largest principal macrostress ($\Sigma_{zz} > \{\Sigma_{xx}, \Sigma_{yy}\}$), the second one, if $\Sigma_{xx} > \{\Sigma_{yy}, \Sigma_{zz}\}$, and the third one, if $\Sigma_{yy} > \{\Sigma_{xx}, \Sigma_{zz}\}$, yielding:

$$\begin{aligned} \max_{\phi,\theta} T_r(\boldsymbol{\Sigma}, \phi, \theta) = T_r(\boldsymbol{\Sigma}, \phi = 0) &= \frac{1}{3} \left[B_{vol} \left(\Sigma_{xx} + \Sigma_{yy} + \Sigma_{zz}\right) - B_{dev} \left(\Sigma_{xx} + \Sigma_{yy} - \Sigma_{zz}\right) \right] \\ & \qquad \Sigma_{zz} > \{\Sigma_{xx}, \Sigma_{yy}\} \\ \max_{\phi,\theta} T_r(\boldsymbol{\Sigma}, \phi, \theta) = T_r(\boldsymbol{\Sigma}, \phi = \frac{\pi}{2}, \theta = 0) &= \frac{1}{3} \left[B_{vol} \left(\Sigma_{xx} + \Sigma_{yy} + \Sigma_{zz}\right) - B_{dev} \left(-2\Sigma_{xx} + \Sigma_{yy} + \Sigma_{zz}\right) \right] \\ & \qquad \Sigma_{xx} > \{\Sigma_{yy}, \Sigma_{zz}\} \\ \max_{\phi,\theta} T_r(\boldsymbol{\Sigma}, \phi, \theta) = T_r(\boldsymbol{\Sigma}, \phi = \frac{\pi}{2}, \theta = \frac{\pi}{2}) &= \frac{1}{3} \left[B_{vol} \left(\Sigma_{xx} + \Sigma_{yy} + \Sigma_{zz}\right) - B_{dev} \left(\Sigma_{xx} - 2\Sigma_{yy} + \Sigma_{zz}\right) \right] \\ & \qquad \Sigma_{yy} > \{\Sigma_{xx}, \Sigma_{zz}\} \quad . \end{aligned} \tag{4.18}$$

Elastic limit-related macroscopic stress intensities Σ_{xx}^{lim}, Σ_{yy}^{lim}, and Σ_{zz}^{lim} follow from specification of the debonding criterion (4.1) for the case-specific maximum normal tractions (4.18), and from considering the limit state $f_{\mathcal{I}_{agg}^{ITZ}} = 0$ as

$$\begin{aligned} B_{vol} \left(\Sigma_{xx}^{lim} + \Sigma_{yy}^{lim} + \Sigma_{zz}^{lim}\right) - B_{dev} \left(\Sigma_{xx}^{lim} + \Sigma_{yy}^{lim} - \Sigma_{zz}^{lim}\right) &= 3\, T_r^{ult} \qquad \Sigma_{zz}^{lim} > \{\Sigma_{xx}^{lim}, \Sigma_{yy}^{lim}\} \\ B_{vol} \left(\Sigma_{xx}^{lim} + \Sigma_{yy}^{lim} + \Sigma_{zz}^{lim}\right) - B_{dev} \left(-2\Sigma_{xx}^{lim} + \Sigma_{yy}^{lim} + \Sigma_{zz}^{lim}\right) &= 3\, T_r^{ult} \qquad \Sigma_{xx}^{lim} > \{\Sigma_{yy}^{lim}, \Sigma_{zz}^{lim}\} \\ B_{vol} \left(\Sigma_{xx}^{lim} + \Sigma_{yy}^{lim} + \Sigma_{zz}^{lim}\right) - B_{dev} \left(\Sigma_{xx}^{lim} - 2\Sigma_{yy}^{lim} + \Sigma_{zz}^{lim}\right) &= 3\, T_r^{ult} \qquad \Sigma_{yy}^{lim} > \{\Sigma_{xx}^{lim}, \Sigma_{zz}^{lim}\}\,. \end{aligned} \tag{4.19}$$

Eqs. (4.19) represent a tetrahedron-shaped elastic limit surface in principal stress space, see Fig. 4.2. Stress states within the failure surface refer to perfect bond in the aggregate-ITZ interface, while stress states on the limit surface result in onset of debonding at the indicated positions. Notably, if all three macroscopic principal stresses are compressive, it is possible that the entire aggregate's surface exhibit compressive normal tractions such that tensile debonding is impossible. The tip of the yield surface refers to isotropic (=hydrostatic) macroscopic tension. In this case, the entire aggregate's surface

exhibit a uniform tensile normal traction, and criterion (4.1) predicts that the entire aggregate-ITZ interface debonds simultaneously, once the macrostresses reaches Σ_{tt}^{lim}, i.e. the isotropic tension-related macrostress level which leads to onset of debonding, reading as

$$\frac{\Sigma_{tt}^{lim}}{T_r^{ult}} = +0.8783\,. \tag{4.20}$$

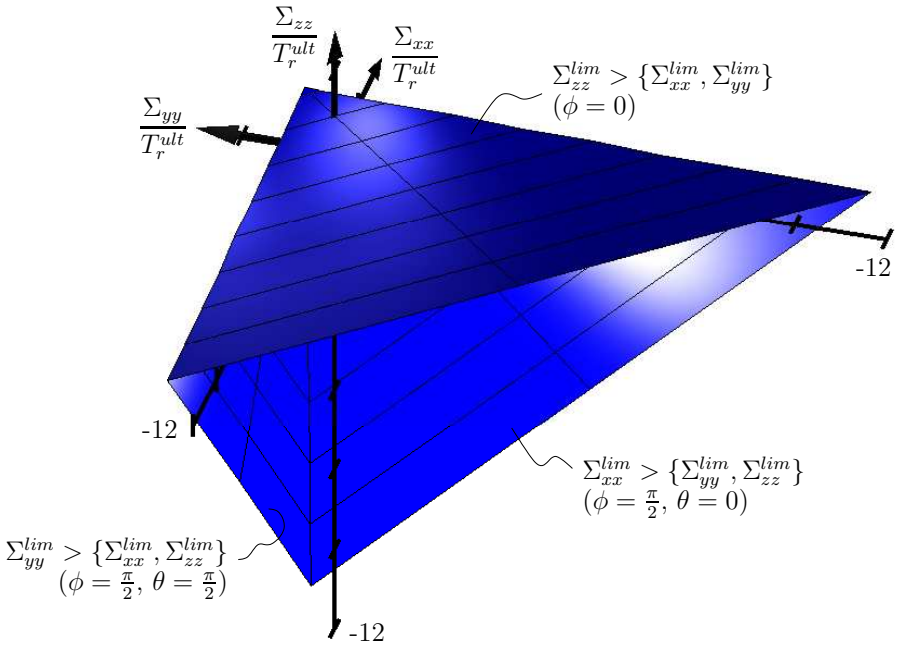

Figure 4.2: Debonding-related elastic limit surface in macroscopic principal stress space: evaluation of debonding relations (4.19) for concrete properties listed in (3.53), see also (3.22), (3.11), and (3.54); in brackets: position on aggregate sphere where debonding starts

4.3 Performance of the ITZ failure criterion

Herein, we upscale the ITZ failure criterion (4.2) to the material scale of concrete, in order to link onset of ITZ failure to corresponding macroscopic stress intensities.[1] Notably, evaluation of the elastic limit criterion (4.2) requires a principal stress analysis, starting from the three-dimensional stress states derived in the previous section, see (3.35), considering (3.34), and $(3.42)_3$ as well as $(3.43)_{1,2}$.

Principal ITZ stresses $\sigma_{ITZ,I} > \sigma_{ITZ,II} > \sigma_{ITZ,III}$ are the eigenvalues of the symmetric stress tensor $\boldsymbol{\sigma}_{ITZ}$ and they are acting in direction of the corresponding eigenvectors $\underline{e}_{ITZ,I}$, $\underline{e}_{ITZ,II}$, and $\underline{e}_{ITZ,III}$ [73]. The eigenvalue problem results in the following characteristic equation, the solution of which are

[1] For macroscopic uniaxial loading, we will also determine the position (in terms of angles ϕ and θ) at which criterion (4.2) foresees this beginning of the ITZ failure process, as well as identify the orientation of the tension-induced first crack.

the sought principal stresses [56]

$$-\sigma_{ITZ,i}^3 + I_1^\sigma \sigma_{ITZ,i}^2 - I_2^\sigma \sigma_{ITZ,i} + I_3^\sigma = 0\,, \qquad i = \{I, II, III\}\,. \tag{4.21}$$

The coefficients of (4.21) can be interpreted as stress invariants and they can be computed from the ITZ stress state as follows [56]

$$\begin{aligned} I_1^\sigma &= \mathrm{tr}(\boldsymbol{\sigma}_{ITZ}) = \sigma_{ITZ,\phi\phi} + \sigma_{ITZ,\theta\theta} + \sigma_{ITZ,rr} \\ I_2^\sigma &= \det\begin{bmatrix} \sigma_{ITZ,\theta\theta} & \sigma_{ITZ,\theta r} \\ \sigma_{ITZ,r\theta} & \sigma_{ITZ,rr} \end{bmatrix} + \det\begin{bmatrix} \sigma_{ITZ,\phi\phi} & \sigma_{ITZ,\phi r} \\ \sigma_{ITZ,r\phi} & \sigma_{ITZ,rr} \end{bmatrix} + \det\begin{bmatrix} \sigma_{ITZ,\phi\phi} & \sigma_{ITZ,\phi\theta} \\ \sigma_{ITZ,\theta\phi} & \sigma_{ITZ,\theta\theta} \end{bmatrix} \\ I_3^\sigma &= \det\begin{bmatrix} \sigma_{ITZ,\phi\phi} & \sigma_{ITZ,\phi\theta} & \sigma_{ITZ,\phi r} \\ \sigma_{ITZ,\theta\phi} & \sigma_{ITZ,\theta\theta} & \sigma_{ITZ,\theta r} \\ \sigma_{ITZ,r\phi} & \sigma_{ITZ,r\theta} & \sigma_{ITZ,rr} \end{bmatrix}. \end{aligned} \tag{4.22}$$

The solution of the characteristic equations (4.21) based on Cardano's formulas and the Haigh-Westergaard coordinates is given in Appendix C.

4.3.1 Macroscopic uniaxial loading

Eqs. (3.48) list the ITZ stress states under macroscopic uniaxial loading aligned with the z-axis, i.e. under

$$\boldsymbol{\Sigma} = \Sigma_{zz}\, \underline{e}_z \otimes \underline{e}_z\,. \tag{4.23}$$

Because of the axial symmetry of the macroscopic loading (3.44), the transformation of ITZ stresses (3.48) into principal ITZ stresses $\sigma_{ITZ,I} \geq \sigma_{ITZ,II} \geq \sigma_{ITZ,III}$, may be considered according to the following simple procedure. The normal stress component $\sigma_{ITZ,\theta\theta}$ represents already a principal normal stress, because the shear stresses $\sigma_{ITZ,\phi\theta}$ and $\sigma_{ITZ,\theta r}$ are equal to zero, see (3.45). The other two principal stresses act in planes perpendicular to the θ-direction, i.e. in the local ϕ-r-planes, such that knowledge of $\sigma_{ITZ,rr}$, $\sigma_{ITZ,\phi\phi}$, and $\sigma_{ITZ,r\phi}$ allows for their determination [56]. Summarizing, the three principal stresses are obtained from

$$\left\{\sigma_{ITZ,I}\,, \sigma_{ITZ,II}\,, \sigma_{ITZ,III}\right\} = \left\{\sigma_{ITZ,\theta\theta}\,, \frac{\sigma_{ITZ,rr} + \sigma_{ITZ,\phi\phi}}{2} \pm \sqrt{\left(\frac{\sigma_{ITZ,rr} - \sigma_{ITZ,\phi\phi}}{2}\right)^2 + {\sigma_{ITZ,r\phi}}^2}\right\} \tag{4.24}$$

After numerical evaluation of the right-hand-side of (4.24), the three computed principal stresses are ordered according to their numerical value and assigned to $\sigma_{ITZ,I}$, $\sigma_{ITZ,II}$, and $\sigma_{ITZ,III}$.

For a typical concrete, intensity and position of the maximum principal normal stress follow from specifying (4.24) for (3.48), (3.22), (3.11), (3.54), and for the concrete properties listed in (3.53). The position of $\max_{\phi,\theta} \sigma_{ITZ,I}$ is described by the zenith angle ϕ, which under uniaxial tension (ϕ_{tu}^{lim}) and under uniaxial compression (ϕ_{cu}^{lim}) amounts to

$$\phi_{tu}^{lim} = 0.3491\,\mathrm{rad}\,, \qquad \phi_{cu}^{lim} = 1.0306\,\mathrm{rad}\,. \tag{4.25}$$

As for the related stress intensities, uniaxial tension leads to

$$\max_{\phi,\theta} \sigma_{ITZ,I} = \sigma_{ITZ,I}(\phi = \phi_{tu}^{lim}, \theta) = 1.1899\,\Sigma_{zz} \qquad \Sigma_{zz} > 0\,. \tag{4.26}$$

see Fig. 4.3 a. Under macroscopic uniaxial compression, in turn, the model delivers

$$\max_{\phi,\theta} \sigma_{ITZ,I} = \sigma_{ITZ,I}(\phi = \phi_{cu}^{lim}, \theta) = -0.2677\,\Sigma_{zz} \qquad \Sigma_{zz} < 0\,. \tag{4.27}$$

The macrostress level related to the onset of ITZ cracking follows from specification of ITZ failure criterion (4.2) for (4.26) and (4.27), respectively, and considering the limit state $f_{ITZ}(\boldsymbol{\Sigma}) = 0$:

$$\frac{\Sigma_{tu}^{lim}}{\sigma_{ITZ}^{ult}} = +0.8404 \qquad \frac{\Sigma_{cu}^{lim}}{\sigma_{ITZ}^{ult}} = -3.736 \tag{4.28}$$

According to $(4.25)_1$, the model suggests that, under macroscopic uniaxial tension, ITZ failure starts in the vicinity of the poles, i.e. along circles of latitude with a zenith angle distance to the poles amounting to $\phi_{tu}^{lim} = 20.00°$, see Fig. 4.3 a. According to $(4.25)_2$, in turn, the model implies that, under macroscopic uniaxial compression, ITZ failure starts a little bit closer to the equator than to the poles, i.e. along circles of latitude with a polar angle distance amounting to $\phi_{cu}^{lim} = 59.05°$, see Fig. 4.3 b. Notably, both maximum principal stresses (4.26) and (4.27) act in the local r-ϕ-planes.

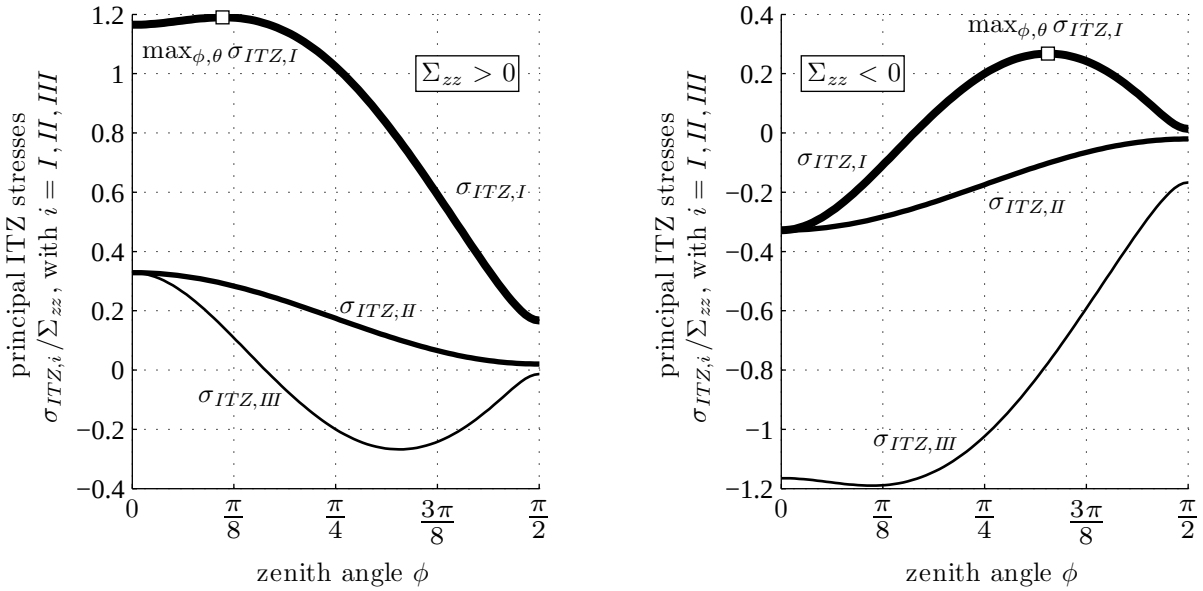

(a) (b)

Figure 4.3: Uniaxial loading ($\Sigma_{zz}\,\underline{e}_z \otimes \underline{e}_z$) induced principal ITZ stresses under tension $\Sigma_{zz} > 0$ (a) and compression $\Sigma_{zz} < 0$ (b), as a function of the zenith angle ϕ, for concrete properties listed in (3.53), see also (3.22), (3.11), and (3.54)

The orientation of the first ITZ cracks is determined next. The directions of the two principal normal stresses acting in the local r, ϕ-planes, relative to the the local r-axis, are described by angles $\gamma(\phi)$ representing the two solution of the following equation [56]

$$\tan(2\gamma(\phi)) = \frac{2\,\sigma_{ITZ,\phi r}(\phi)}{\sigma_{ITZ,rr}(\phi) - \sigma_{ITZ,\phi\phi}(\phi)} \tag{4.29}$$

In order to arrive at a global description of the crack orientation, we introduce $\varrho(\phi)$ as the angle between the global z-direction and the direction of the largest principal ITZ normal stress. This angle is accessible from (4.29) when considering that the local r-direction is rotated by the angle ϕ relative to the z-axis:

$$\varrho(\phi) = \phi + \gamma(\phi)\,, \tag{4.30}$$

where $\gamma(\phi)$ is the relevant solution of (4.29). The orientation of the normal vector to the local crack plane, i.e. the orientation of the maximum of the largest principal ITZ stress with respect to the global z-axis, is denoted as ϱ_{cu}^{lim} for uniaxial compression and ϱ_{tu}^{lim} for uniaxial tension, respectively, and follows from (4.30) if considering the position ϕ_{tu}^{lim} and ϕ_{cu}^{lim}, respectively. The model suggests, that the direction of the maximum principal ITZ stress deviates by only 3.28° from the direction of macroscopic tensile loading, and by only 16.48° from the direction perpendicular to the direction of the macroscopic compressive loading, respectively (Fig. 4.4)

$$\varrho_{tu}^{lim} = 0.0572\,\text{rad} \qquad \varrho_{cu}^{lim} = 1.8585\,\text{rad} \tag{4.31}$$

This implies that, under macroscopic tension, the first ITZ cracks propagate in good approximation in a plane perpendicular to the direction of macroscopic loading, while under macroscopic uniaxial compression, the first ITZ cracks propagate practically in the direction of macroscopic loading.

4.3.2 Macroscopic biaxial loading

For macroscopic biaxial loading $\boldsymbol{\Sigma} = \Sigma_{xx}\,\underline{e}_x \otimes \underline{e}_x + \Sigma_{yy}\,\underline{e}_y \otimes \underline{e}_y$, the principal ITZ stresses follow from the solution of the characteristic equation (4.21), specified for the invariants (4.22) and for the ITZ stresses given in (3.35), (3.42), and in (3.43); see also Appendix C. Insertion of the maximum of the largest principal ITZ stress $\max_{\phi,\theta}\sigma_I(\boldsymbol{\Sigma}, \phi, \theta)$ into the ITZ failure criterion (4.2) and solving the resulting expression for Σ_{xx} and Σ_{yy} delivers macrostresses corresponding to the onset of microcracks caused by ITZ failure. This results in a elastic limit envelope consisting of six virtually linear branches (Fig. 4.6). It has to be determined point-by-point, in the framework of a numerical solution procedure. Stress states within the elastic limit surface are elastic (all bonds remain intact), while stress states on the elastic limit surface are related to onset of ITZ cracking at the most heavily loaded position. There, the crack plane is perpendicular to the direction of the maximum principal normal stress.

While Appendix E.3 lists the full implementation of a numerical solution procedure for determination of the elastic limit envelope and of the orientation of the first ITZ cracks, most relevant details are briefly described next. Given the isotropy of concrete and the resulting axial symmetry of the

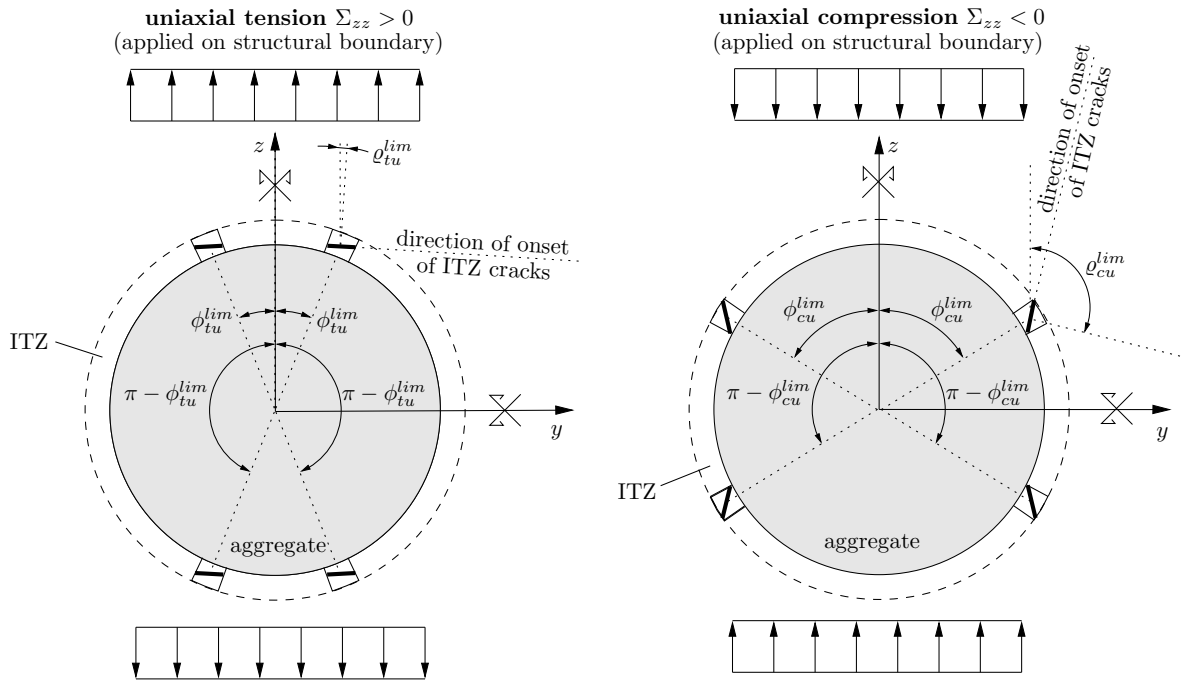

Figure 4.4: Position of onset of ITZ failure and orientation of ITZ cracks under uniaxial tension and under uniaxial compression in the y, z-plane

elastic limit envelope with respect to the first median, it is sufficient to determine one half of the elastic limit envelope and to complete it by mirroring the computed part around the first median (compare Figs. 4.6 and 4.5 a). In this context, it is useful to introduce the stress ratio $a = \Sigma_{xx}/\Sigma_{yy}$ and to investigate positive and negative values of Σ_{yy} as well as values of a in the interval $[-1\,, +1]$, see Fig. 4.5 a. This can be elegantly solved based on nested loops. In the context of finding the position of the largest maximum principal ITZ stress, evaluation of the stress concentration from the macroscale down to principal ITZ stresses may be restricted to one eighth of the aggregate's surface, again because of the symmetries of the underlying problem. To this end, we subdivide the aggregate's surface part within the first octant of the global x, y, z coordinate system (i.e. in the domain $0 \leq \phi \leq \pi/2$ and $0 \leq \theta \leq \pi/2$) into 25×25 grid points, see Fig. 4.5 b for such a grid representation. The one grid point, at which the largest maximum principal ITZ stress is computed for a specific realization of the macroscopic loading, marks the position at which ITZ failure criterion (4.2) suggests onset of ITZ cracking.

Details regarding the numerical procedure, finding the location of the maximum of the largest principal stress for different ratios of Σ_{xx} over Σ_{yy} are given in Appendix E.3. Relating macroscopic elastic limits to the ITZ strength yields a dimensionless illustration in the biaxial stress space, see Fig. 4.6, where again the reference material parameters (3.53) are used.

As for symmetric biaxial compression and tension ($\Sigma_{xx} = \Sigma_{yy}$) we quantify the model predictions.

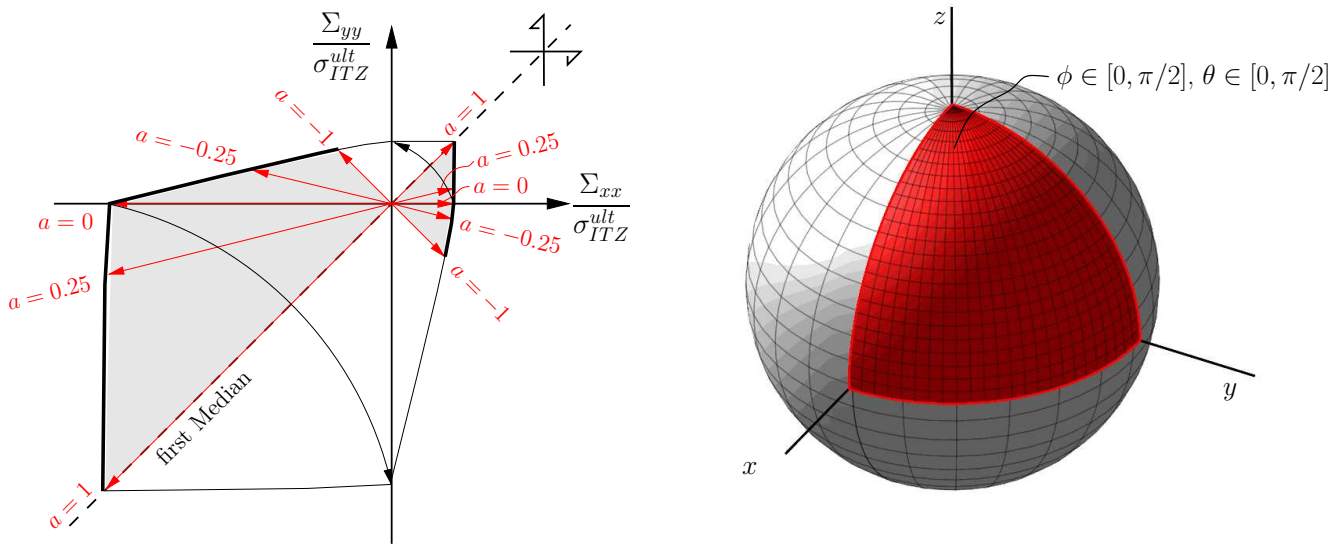

(a) (b)

Figure 4.5: (a) Exploring the macroscopic biaxial stress space with the stress ratio $a = \Sigma_{xx}/\Sigma_{yy}$; (b) grid points on the first octant of the unit sphere in which the maximum of the largest principal ITZ stress is searched

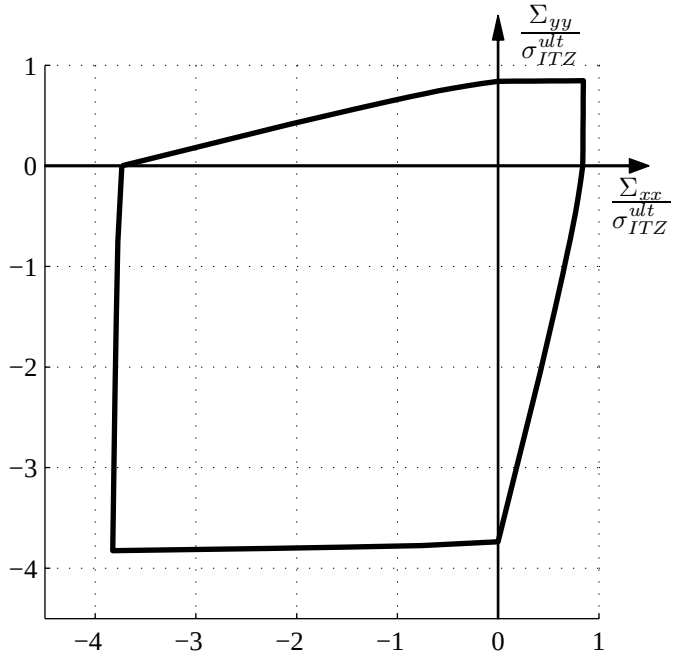

Figure 4.6: ITZ failure-related elastic limit envelope for macroscopic biaxial loading $\mathbf{\Sigma} = \Sigma_{xx}\,\underline{e}_x \otimes \underline{e}_x + \Sigma_{yy}\,\underline{e}_y \otimes \underline{e}_y$ for concrete properties listed in (3.53), see also (3.22), (3.11), and (3.54)

The dimensionless elastic limit-related macrostress levels amount to

$$\frac{\Sigma_{tb}^{lim}}{\sigma_{ITZ}^{ult}} = +0.8465 \qquad \frac{\Sigma_{cb}^{lim}}{\sigma_{ITZ}^{ult}} = -3.826\,. \tag{4.32}$$

4.3.3 General three-dimensional macroscopic stress states

Considering general triaxial macroscopic loading in terms of principal stresses Σ_{xx}, Σ_{yy}, and Σ_{zz}

$$\boldsymbol{\Sigma} = \Sigma_{xx}\,\underline{e}_x \otimes \underline{e}_x + \Sigma_{yy}\,\underline{e}_y \otimes \underline{e}_y + \Sigma_{zz}\,\underline{e}_z \otimes \underline{e}_z \tag{4.33}$$

again a numerical procedure is required for determination of the position at which the largest of the maximum principal ITZ stresses occurs. As for illustration of the resulting elastic limit surface in three-dimensional principal stress space it is useful to introduce Haigh-Westergaard coordinates of the macroscopic loading (4.33). They are cylindrical coordinates, whereby the cylinder axis coincides with the hydrostatic axis defined through $\Sigma_{xx} = \Sigma_{yy} = \Sigma_{zz}$:

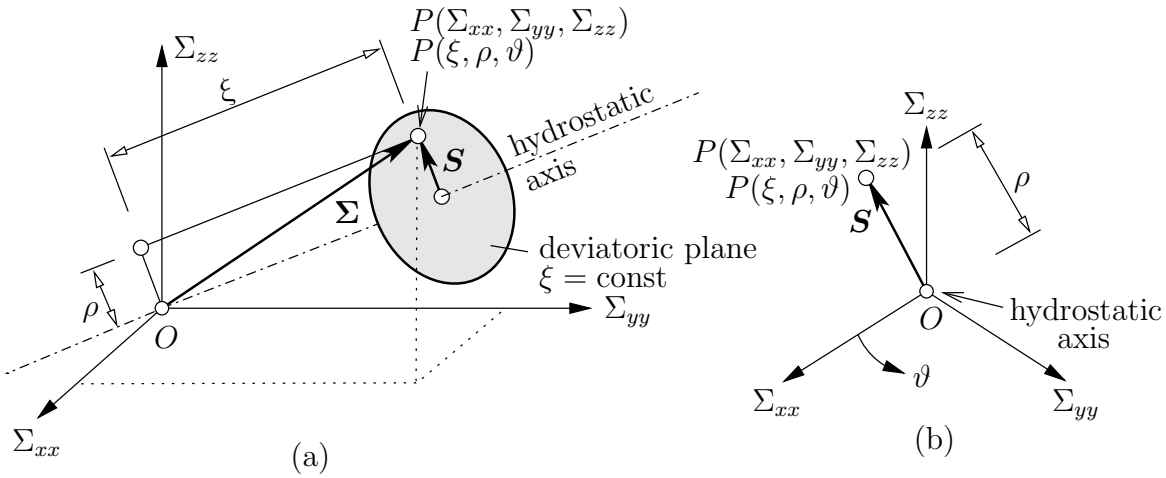

Figure 4.7: (a) Macroscopic stress tensor $\boldsymbol{\Sigma}$ in macroscopic principal stress space Σ_{xx}, Σ_{yy}, and Σ_{zz}, introduction of Haigh-Westergaard coordinates ξ, ρ, and ϑ; (b) deviatoric plane contains stress deviator $\boldsymbol{S}$

- ξ is the axial (hydrostatic) coordinate, quantifying the distance of the stress state (in direction of the hydrostatic axis) from the origin of the coordinate system, i.e. the distance of the deviatoric plane containing the stress state (Fig. 4.7).
- ρ is the radial coordinate, quantifying the distance of the stress state from the intersection of the hydrostatic axis with the deviatoric plane containing the stress state.
- ϑ is the so-called Lode angle [54] marking positions in the deviatoric plane relative to the projection of the Σ_{xx}-axis.

The relation between the three coordinates ξ, ρ, and ϑ, on the one hand, and the principal macrostresses Σ_{xx}, Σ_{yy}, and Σ_{zz}, on the other hand, involves so-called invariants of the stress tensor $\boldsymbol{\Sigma}$ and of the stress deviator $\boldsymbol{S}$, defined as [73]

$$I_1^{\boldsymbol{\Sigma}} = \operatorname{tr} \boldsymbol{\Sigma} \quad J_2^{\boldsymbol{S}} = \frac{1}{2} \boldsymbol{S} : \boldsymbol{S} \,, \quad J_3^{\boldsymbol{S}} = \frac{1}{3} \left(\boldsymbol{S} \cdot \boldsymbol{S} \right) : \boldsymbol{S} \,, \quad \text{with} \quad \boldsymbol{S} = \boldsymbol{\Sigma} - \frac{I_1^{\boldsymbol{\Sigma}}}{3} \mathbf{1} \,, \tag{4.34}$$

and they read as [65]

$$\xi = \frac{1}{\sqrt{3}} I_1^{\boldsymbol{\Sigma}} \,, \quad \rho = \sqrt{2\, J_2^{\boldsymbol{S}}} \,, \quad \cos 3\theta = \frac{3\sqrt{3}}{2} \, \frac{J_3^{\boldsymbol{S}}}{\left(J_2^{\boldsymbol{S}} \right)^{3/2}} \,. \tag{4.35}$$

Notably, six different points in the Haigh-Westergaard representation correspond to one macroscopic stress tensor, since the eigenvalues of $\boldsymbol{\Sigma}$ can be ordered arbitrarily [13].

The simple microscopic ITZ failure criterion (4.2) translates into a quite complex macroscopic elastic limit surface representing an irregular six-sided pyramid consisting of six curved surface parts, connected to each other along the so-called tensile and compressive meridians, characterized by $\vartheta = \{0\,, 2\pi/3\,, 4\pi/3\}$ and by $\vartheta = \{\pi/3\,, \pi\,, 5\pi/3\}$, respectively (Fig. 4.8). While Appendix E.3 lists the full implementation of a numerical solution procedure for determination of this macroscopic elastic limit surface, most relevant details are briefly described next. The tip of the pyramid follows simply from consideration of an isotropic tensile macroloading $\Sigma_{xx} = \Sigma_{yy} = \Sigma_{zz}$, resulting in a homogeneous stress state all over the ITZ shell, such that the ITZ failure criterion predicts – at least theoretically – a simultaneous failure of the entire ITZ, once $\max_{\phi,\theta} T_r(\boldsymbol{\Sigma}, \phi, \theta)$ reaches σ_{ITZ}^{ult}. The macrostress level under hydrostatic tension, which leads to onset of ITZ cracking, Σ_{tt}^{ult}, is quantified for reference material properties (3.53):

$$\frac{\Sigma_{tt}^{lim}}{\sigma_{ITZ}^{ult}} = +0.8788 \tag{4.36}$$

The rest of the failure surface is determined point-by-point, whereby it is useful to compute intersections of the elastic limit surface with deviatoric planes (Fig. 4.9). In this context, the Haigh-Westergaard component ξ is fixed first to a specific value of interest, and a loop is carried out for values of ϑ ranging from 0 to $\pi/3$. The isotropy on concrete, namely, implies that it is sufficient to determine one sixth of elastic limit surface (in the Lode angle regime $\vartheta \in [0\,, \pi/3]$) and to complete the entire elastic limit surface by mirroring around the plane defined by Lode angle $\vartheta = 0$ and subsequently by rotation of this part around the hydrostatic axis for $\pm 2\,\pi/3$. In the context of finding the position of the largest maximum principal ITZ stress, evaluation of the stress concentration from the macroscale down to principal ITZ stresses may be again restricted – because of symmetry properties – to one eighth of the aggregate's surface, see also Fig. 4.5 b. In this context, we again employ the subdivision of the aggregate's surface part within the first octant into 25×25 grid points. The one grid point, at which the largest maximum principal ITZ stress is computed for a specific realization of the macroscopic loading, marks the position at which ITZ failure criterion (4.2) suggests onset of ITZ cracking. In more detail, for every pair of values of ξ and ϑ, the deviatoric Haigh-Westergaard component ρ is progressively increased (starting from zero), until the largest of the maximum principal

ITZ stresses reaches the tensile microstrength σ^{ult}_{ITZ}. Connecting computed points of the elastic limit surface, lying on the tensile or the compressive meridian, respectively, allows for plotting sections through principal stress space which contain the hydrostatic axis and one of the mentioned meridians (Fig. 4.10). This implies that both elastic limit meridians are markedly non-linear in the regime where the hydrostatic part of the macrostress state, ξ, is tensile, and that the compressive meridian increases with a steeper slope than the tensile meridian, when starting at the pyramid tip and considering a series of macroscopic stress states characterized by decreasing values of their hydrostatic part.

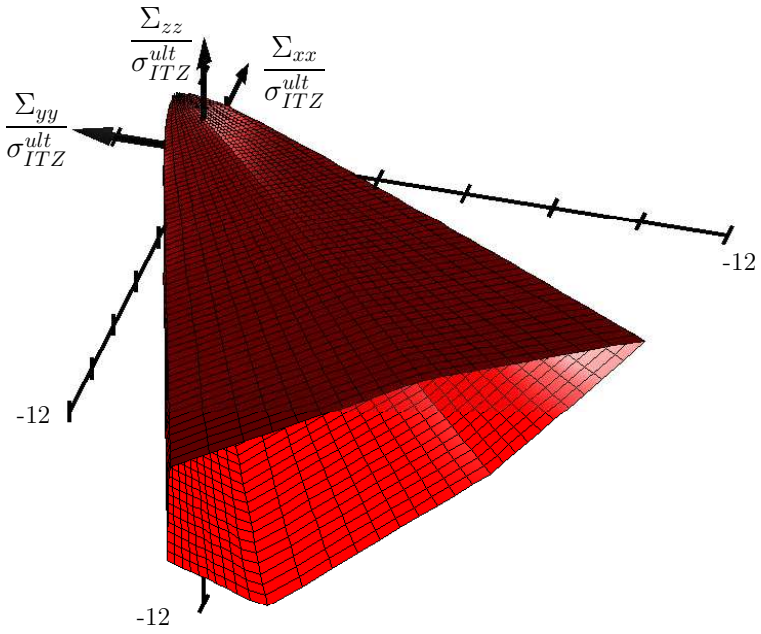

Figure 4.8: ITZ failure-related elastic limit surface in macroscopic principal stress space for concrete properties listed in (3.53), see also (3.22), (3.11), and (3.54)

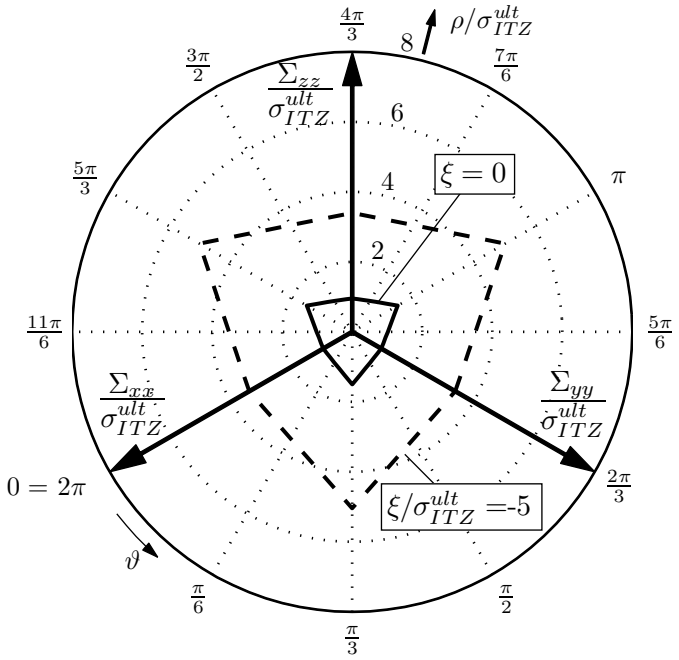

Figure 4.9: ITZ failure-related elastic limit surfaces in different deviatoric sections through the macroscopic principal stress space for concrete properties listed in (3.53), see also (3.22), (3.11), and (3.54)

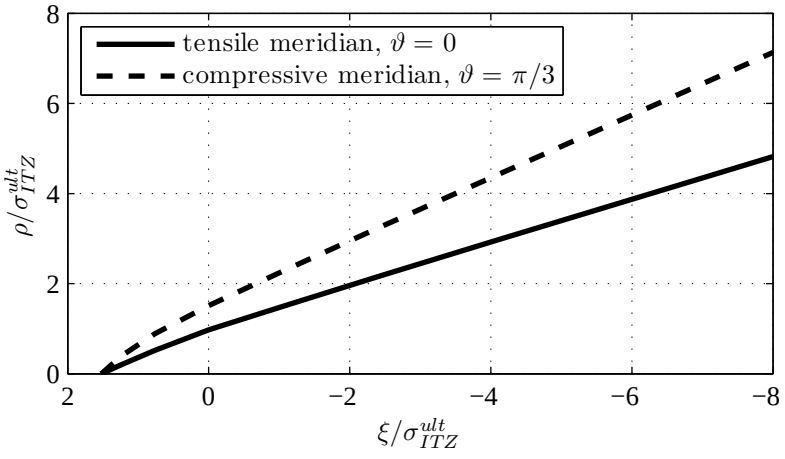

Figure 4.10: Tensile and compressive meridians in macroscopic principal stress space for concrete properties listed in (3.53), see also (3.22), (3.11), and (3.54)

Chapter 5

Discussion

5.1 Comparison of the debonding model with the ITZ failure model

Comparison of the performance of the aggregate debonding criterion (4.1) with the one of the ITZ failure criterion (4.2) requires a relation between the debonding strength T_r^{ult} and the ITZ strength σ_{ITZ}^{ult}. Unfortunately, no experimental insight into this relation is available, because there are no direct testing methods for characterization of debonding strength or ITZ strength, respectively. This is the motivation for carrying out case studies, in which we will assume that T_r^{ult} is larger or smaller, respectively, than σ_{ITZ}^{ult}. This is done for uniaxial compression and symmetric biaxial compression, two types of loading frequently investigated in macroscopic laboratory testing of concrete.[1] Complementing these loading types, we will also discuss different types of tensile macroscopic loading, including uniaxial, symmetric biaxial, and isotropic triaxial tension. In all cases, properties of a typical concrete are considered, see the elastic properties listed in (3.50), (3.51), and (3.52) as well as the aggregate dosage $f_{agg} = 65\,\%$, see (3.49).

Under macroscopic compressive stress states (uniaxial and symmetric biaxial compression), the debonding criterion (4.1) and the ITZ failure criterion (4.2) predict the following elastic limits:

$$\begin{aligned} &\text{uniaxial compression} \quad \dots \quad \Sigma_{cu}^{lim} = \begin{cases} -74.29\, T_r^{ult} & \dots \quad \text{debonding} \\ -3.736\, \sigma_{ITZ}^{ult} & \dots \quad \text{ITZ failure} \end{cases} \\ &\text{symmetric biaxial compression} \quad \dots \quad \Sigma_{cb}^{lim} = \begin{cases} -37.14\, T_r^{ult} & \dots \quad \text{debonding} \\ -3.826\, \sigma_{ITZ}^{ult} & \dots \quad \text{ITZ failure} \end{cases} \end{aligned} \tag{5.1}$$

see also (4.7), (4.28), (4.15), and (4.32). (5.1) implies that aggregate debonding is relevant if the

[1] Isotropic triaxial compression yields to uniform fields of traction vectors and ITZ stresses, respectively. Since they are compressive, tension-driven debonding or ITZ failure is not possible.

debonding strength is significantly smaller than the ITZ strength, i.e.

$$\begin{aligned}
&\text{uniaxial compression} \quad \dots \quad \begin{cases} T_r^{ult}/\sigma_{ITZ}^{ult} < 0.0503 & \dots \text{ debonding is relevant} \\ T_r^{ult}/\sigma_{ITZ}^{ult} > 0.0503 & \dots \text{ ITZ failure is relevant} \end{cases} \\
&\text{symmetric biaxial compression} \quad \dots \quad \begin{cases} T_r^{ult}/\sigma_{ITZ}^{ult} < 0.103 & \dots \text{ debonding is relevant} \\ T_r^{ult}/\sigma_{ITZ}^{ult} > 0.103 & \dots \text{ ITZ failure is relevant} \end{cases}
\end{aligned} \tag{5.2}$$

(5.2) suggests that debonding can only be expected for aggregates exhibiting very polished surfaces which do not well connect to the surrounding ITZ shell, while ITZ failure appears to be relevant in the more realistic case that the debonding strength and the ITZ strength are on the same order of magnitude.

Under macroscopic tensile stress states (uniaxial, symmetric biaxial, and isotropic triaxial tension), the debonding criterion (4.1) and the ITZ failure criterion (4.2) predict the following elastic limits:

$$\begin{aligned}
&\text{uniaxial tension} \quad \dots \quad \Sigma_{tu}^{lim} = \begin{cases} 0.8585\, T_r^{ult} & \dots \text{ debonding} \\ 0.8404\, \sigma_{ITZ}^{ult} & \dots \text{ ITZ failure} \end{cases} \\
&\text{symmetric biaxial tension} \quad \dots \quad \Sigma_{tb}^{lim} = \begin{cases} 0.8685\, T_r^{ult} & \dots \text{ debonding} \\ 0.8465\, \sigma_{ITZ}^{ult} & \dots \text{ ITZ failure} \end{cases} \\
&\text{isotropic triaxial tension} \quad \dots \quad \Sigma_{tt}^{lim} = \begin{cases} 0.8783\, T_r^{ult} & \dots \text{ debonding} \\ 0.8788\, \sigma_{ITZ}^{ult} & \dots \text{ ITZ failure} \end{cases}
\end{aligned} \tag{5.3}$$

see also (4.7), (4.28), (4.15), (4.32), (4.20), and (4.36). (5.3) implies that – practically speaking – aggregate debonding is relevant if the debonding strength is smaller than the ITZ strength, and vice versa:

$$\begin{aligned}
&\text{uniaxial tension} \quad \dots \quad \begin{cases} T_r^{ult}/\sigma_{ITZ}^{ult} < 0.979 & \dots \text{ debonding is relevant} \\ T_r^{ult}/\sigma_{ITZ}^{ult} > 0.979 & \dots \text{ ITZ failure is relevant} \end{cases} \\
&\text{symmetric biaxial tension} \quad \dots \quad \begin{cases} T_r^{ult}/\sigma_{ITZ}^{ult} < 0.975 & \dots \text{ debonding is relevant} \\ T_r^{ult}/\sigma_{ITZ}^{ult} > 0.975 & \dots \text{ ITZ failure is relevant} \end{cases} \\
&\text{symmetric biaxial tension} \quad \dots \quad \begin{cases} T_r^{ult}/\sigma_{ITZ}^{ult} < 1.001 & \dots \text{ debonding is relevant} \\ T_r^{ult}/\sigma_{ITZ}^{ult} > 1.001 & \dots \text{ ITZ failure is relevant} \end{cases}
\end{aligned} \tag{5.4}$$

(5.4) suggests that debonding is expected for concretes with rather polished aggregates while ITZ failure appears to be relevant for good mechanical interlock between aggregates and the ITZ shell, as well as for weak ITZs which, nonetheless, connect well to the aggregate's surface.

5.2 Comparison of model predictions with experimental results

Lack of quantitative experimental data regarding onset of debonding or onset of ITZ failure, respectively, renders comparison of model predictions with experimental observations a challenging task. We

have to rely on typically reported ranges for elastic limits under uniaxial tension and compression, as well as on typical relations between uniaxial tensile strength and uniaxial compressive strength of concrete; as is detailed next. Recalling experimental observations described in Sect. 2, we note that the macroscopic elastic limit under uniaxial tension ($\Sigma^{lim}_{tu,exp}$) ranges from 70 to 100 % of the macroscopic uniaxial tensile strength ($\Sigma^{ult}_{tu,exp}$) [46, 84, 6, 50],

$$\Sigma^{lim}_{tu,exp} \in [0.7\,,1.0]\,\Sigma^{ult}_{tu,exp} \tag{5.5}$$

The macroscopic elastic limit under uniaxial compression ($\Sigma^{lim}_{cu,exp}$) ranges from 30 to 50 % of the macroscopic uniaxial compressive strength ($\Sigma^{ult}_{cu,exp}$) [42, 76, 46, 25]:

$$\Sigma^{lim}_{cu,exp} \in [0.3\,,0.5]\,\Sigma^{ult}_{cu,exp} \tag{5.6}$$

The typical ratio between the absolute values of the uniaxial tensile strength and the uniaxial compressive strength ranges from 1:10 to 1:12

$$\frac{\Sigma^{ult}_{tu,exp}}{|\Sigma^{ult}_{cu,exp}|} \in [0.100\,,0.08\dot{3}] \tag{5.7}$$

(5.5) and (5.6) together with (5.7) allow for determination that the ratio between the elastic limits in uniaxial tension and in uniaxial compression range from 12 to 33 %:

$$\frac{\Sigma^{lim}_{tu,exp}}{|\Sigma^{lim}_{cu,exp}|} = \frac{[0.7\,,1.0]\,\Sigma^{ult}_{tu,exp}}{[0.3\,,0.5]\,|\Sigma^{ult}_{cu,exp}|} = \frac{[0.7\,,1.0]}{[0.3\,,0.5]} \times \frac{\Sigma^{ult}_{tu,exp}}{|\Sigma^{ult}_{cu,exp}|} = \frac{[0.7\,,1.0]}{[0.3\,,0.5]} \times [0.100\,,0.08\dot{3}] = [0.12\,,0.\dot{3}] \tag{5.8}$$

This experiment-related interval is now compared with corresponding model predictions stemming from the debonding model and from the ITZ failure model, respectively.

When it comes to model predictions for macroscopic elastic limits under uniaxial tension and uniaxial compression, respectively, we note that model predictions (5.2) and (5.4) suggest the following scenarios to be possible:

$$\left.\begin{array}{l}\text{debonding in tension and}\\ \text{debonding in compression}\end{array}\right\} \quad \frac{T^{ult}_r}{\sigma^{ult}_{ITZ}} < 0.0503$$

$$\left.\begin{array}{l}\text{debonding in tension and}\\ \text{ITZ failure in compression}\end{array}\right\} \quad \frac{T^{ult}_r}{\sigma^{ult}_{ITZ}} \in [0.0503\,,0.979] \tag{5.9}$$

$$\left.\begin{array}{l}\text{ITZ failure in tension and}\\ \text{ITZ failure in compression}\end{array}\right\} \quad \frac{T^{ult}_r}{\sigma^{ult}_{ITZ}} > 0.979$$

ITZ failure in tension and debonding in compression is not realistic when relying on the two strength models, because the "ITZ failure in tension"-related condition $T^{ult}_r/\sigma^{ult}_{ITZ} > 0.979$ contradicts the "debonding in compression"-related condition $T^{ult}_r/\sigma^{ult}_{ITZ} < 0.0503$, see (5.2) and (5.4). For the scenarios listed in (5.9) we now calculate model predictions for the ratio between the elastic limits in

uniaxial tension and uniaxial compression, based on (5.1) and (5.3):

$$\left.\begin{array}{l}\text{debonding in tension and}\\ \text{debonding in compression}\end{array}\right\} \quad \dots \quad \frac{\Sigma_{tu}^{lim}}{|\Sigma_{cu}^{lim}|} = \frac{0.8585\, T_r^{ult}}{|-74.26\, T_r^{ult}|} = 0.01$$

$$\left.\begin{array}{l}\text{debonding in tension and}\\ \text{ITZ failure in compression}\end{array}\right\} \quad \dots \quad \frac{\Sigma_{tu}^{lim}}{|\Sigma_{cu}^{lim}|} = \frac{0.8585\, T_r^{ult}}{|-3.736\, \sigma_{ITZ}^{ult}|} = 0.23\, \frac{T_r^{ult}}{\sigma_{ITZ}^{ult}} \tag{5.10}$$

$$\left.\begin{array}{l}\text{ITZ failure in tension and}\\ \text{ITZ failure in compression}\end{array}\right\} \quad \dots \quad \frac{\Sigma_{tu}^{lim}}{|\Sigma_{cu}^{lim}|} = \frac{0.8404\, \sigma_{ITZ}^{ult}}{|-3.736\, \sigma_{ITZ}^{ult}|} = 0.22$$

Eqs. (5.8) to (5.10) allow us to assess whether or not the three investigated scenarios appear to be realistic for concrete in view of available experimental observations:

- Given that $T_r^{ult}/\sigma_{ITZ}^{ult} < 0.0503$, the two strength models suggest that debonding is relevant both in tension and compression, but this is related to a model-predicted elastic limit ratio which is by one order of magnitude too small as to fall within the experiment-related interval given in (5.8):

$$\frac{\Sigma_{tu}^{lim}}{|\Sigma_{cu}^{lim}|} = 0.01 \ll [0.12\,, 0.\dot{3}] = \frac{\Sigma_{tu,exp}^{lim}}{|\Sigma_{cu,exp}^{lim}|} \tag{5.11}$$

  This implies that $T_r^{ult}/\sigma_{ITZ}^{ult} < 0.0503$ is not realistic for typical concretes.

- Given that $T_r^{ult}/\sigma_{ITZ}^{ult} > 0.979$, the two strength models suggest that ITZ failure is relevant both in tension and compression, and this is related to a model-predicted elastic limit ratio which lies well within the experiment-related interval of (5.8):

$$\frac{\Sigma_{tu}^{lim}}{|\Sigma_{cu}^{lim}|} = 0.22 \in [0.12\,, 0.\dot{3}] = \frac{\Sigma_{tu,exp}^{lim}}{|\Sigma_{cu,exp}^{lim}|} \tag{5.12}$$

  This implies that $T_r^{ult}/\sigma_{ITZ}^{ult} > 0.979$ appears to be realistic for typical concretes. Notably, the model predicted stress ratio is approximately equal to the mean value of the experimentally determined interval, see (5.12).

- Debonding in tension and ITZ failure in compression, appears to be realistic as long as the ratio between debonding strength and ITZ strength ranges between the following interval,

$$\frac{T_r^{ult}}{\sigma_{ITZ}^{ult}} \in [0.50\,, 0.98] \tag{5.13}$$

  because (5.10) and (5.13) imply that

$$\frac{\Sigma_{tu}^{lim}}{|\Sigma_{cu}^{lim}|} \in [0.12\,, 0.22] \quad \text{and this is within} \quad [0.12\,, 0.\dot{3}] = \frac{\Sigma_{tu,exp}^{lim}}{|\Sigma_{cu,exp}^{lim}|} \tag{5.14}$$

Next, we draw the conclusions, based on the described comparison of model predictions with

experimental observations on concrete. In this context, we also consider that model predicted elastic limits under uniaxial, biaxial and triaxial tension do not differ significantly, and that the elastic limits under uniaxial and biaxial compression are also virtually the same in case of ITZ failure, see (5.1) and (5.3).

1. In real concretes, it is unlikely that the debonding strength is smaller than one half of the ITZ strength.

2. For real concretes, it is realistic that the debonding strength ranges from 50 to 100 % of the ITZ strength. In this case, the developed models suggest that debonding is relevant for onset of cracking under macroscopic tensile loading, and ITZ failure under macroscopic compression.

3. For real concretes, it is also realistic that the debonding strength is larger than the ITZ strength. In this case, the developed models suggest that ITZ failure is always relevant for onset of cracking.

4. If the debonding strength is practically equal to the ITZ strength, then ITZ failure is relevant under macroscopic compression, while debonding and ITZ failure are both realistic for onset of cracking under predominant macroscopic tension.

5.3 Sensitivity analysis: influence of composition on model predictions

So far, we focused on a typical concrete, with quartz aggregates, an initial water-to-cement mass ratio amounting to 0.5, a hydration degree close to complete hydration, an aggregate content of 65 %, and an ITZ which is more compliant than the bulk cement paste, see (3.49)-(3.52) and the related dimensionless properties given in (3.53). In all practical applications, however, a variety of concretes with properties different from those listed in (3.53) are in use. This is the motivation to perform a sensitivity analysis.

The aggregate volume fraction ranges in typical concretes within the following interval

$$f_{agg} \in [0.6\,, 0.7]. \tag{5.15}$$

A smaller amount of aggregates (and therefore, a higher content of cement) is non-economic, and for a larger aggregate content must be expected to reduce the workability of the mix. Still, we will investigate the sensitivity of our model predictions in a larger interval, namely $f_{agg} \in [0.5\,, 0.85]$.

Elastic properties of aggregates differ from product to product. Young's modulus ranges from 96 GPa for quartz [11] over typically $20 - 70$ GPa for limestone [30] down to $3 - 20$ GPa for lightweight aggregates [63]. Poisson's ratio ranges from 0.08 for quartz [11] to $0.2 - 0.3$ for limestone [30] or lightweight aggregates [63]. Elastic properties of cement paste, in turn, depend on the composition and the maturity, i.e. on the initial water-to-cement mass ratio w/c and on the degree of hydration. While Poisson's ratio exhibits only small variance between 0.2 and 0.25, Young's modulus of the cement paste is strongly influenced by w/c and the hydration degree. At very early ages, close to the

liquid-solid transition of cement paste, Young's modulus of cement paste is very small compared to that of frequently used aggregates. Mature, sub-stoichiometric mixed ($w/c < 0.42$), however, exhibit Young's moduli of up to 29 GPa [39]. Thus provides the motivation to study the sensitivity of our model predictions in the intervals

$$\nu_{agg} \in [0.05\,,0.4]\,, \qquad \frac{E_{agg}}{E_{cp}} \in [0\,,20]. \tag{5.16}$$

Nanoindentation tests imply that mature ITZs reach only $70-85$ % of the stiffness of the bulk cement paste. At very early ages, however, the ITZ might exhibit a greater stiffness than the bulk cement paste, because segregation yields to higher density of smaller clinker grains in the ITZ, and they dissolve faster [75], such that the ITZ might be denser than the bulk cement paste at very early ages. This is the motivation to study our model prediction in the interval

$$\frac{E_{ITZ}}{E_{cp}} \in [0.5\,,1.3]. \tag{5.17}$$

In the sequel, we perform sensitivity analyses, whereby we vary one of the dimensionless quantities E_{agg}/E_{cp}, E_{ITZ}/E_{cp}, ν_{agg}, and f_{agg} within the aforedescribed intervals, see (5.15)-(5.17). At the same time, we keep all the other dimensionless quantities equal to the values given in (3.53). Focusing on uniaxial loading (3.44) we repeat the study described in Sections 3 and 4, yielding dimensionless elastic limits under uniaxial tension and compression, related to debonding (4.1) and to ITZ failure (4.2), respectively, see Figs. 5.1 and 5.2.

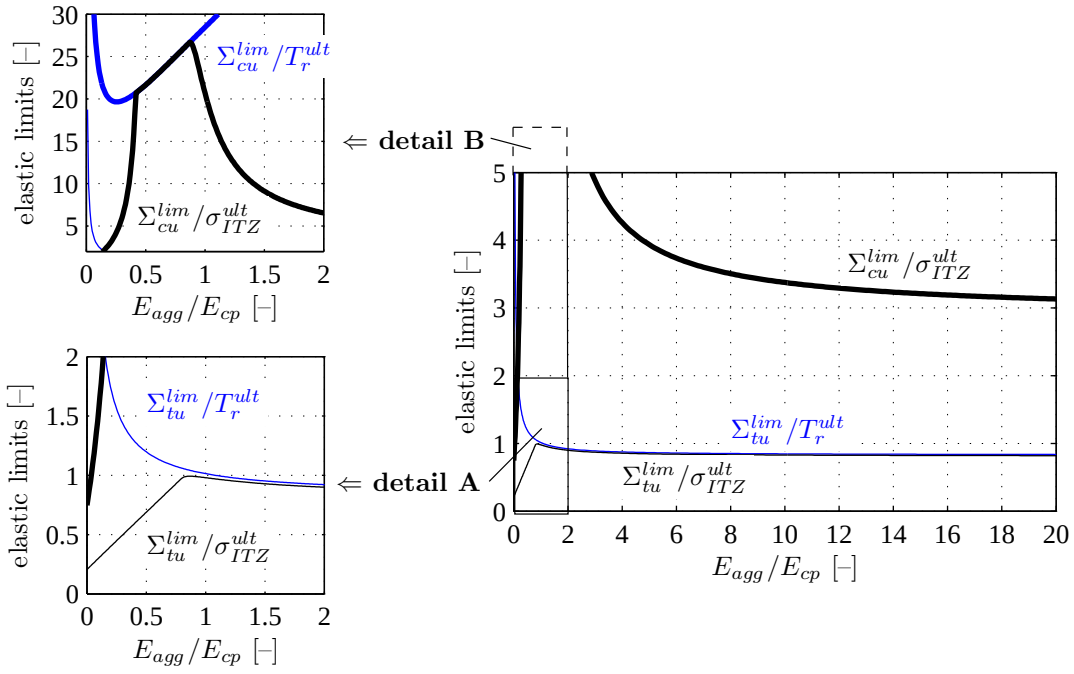

Figure 5.1: Dimensionless elastic limits for concrete properties according to (3.53) for varying E_{agg}/E_{cp} within the interval (5.16)

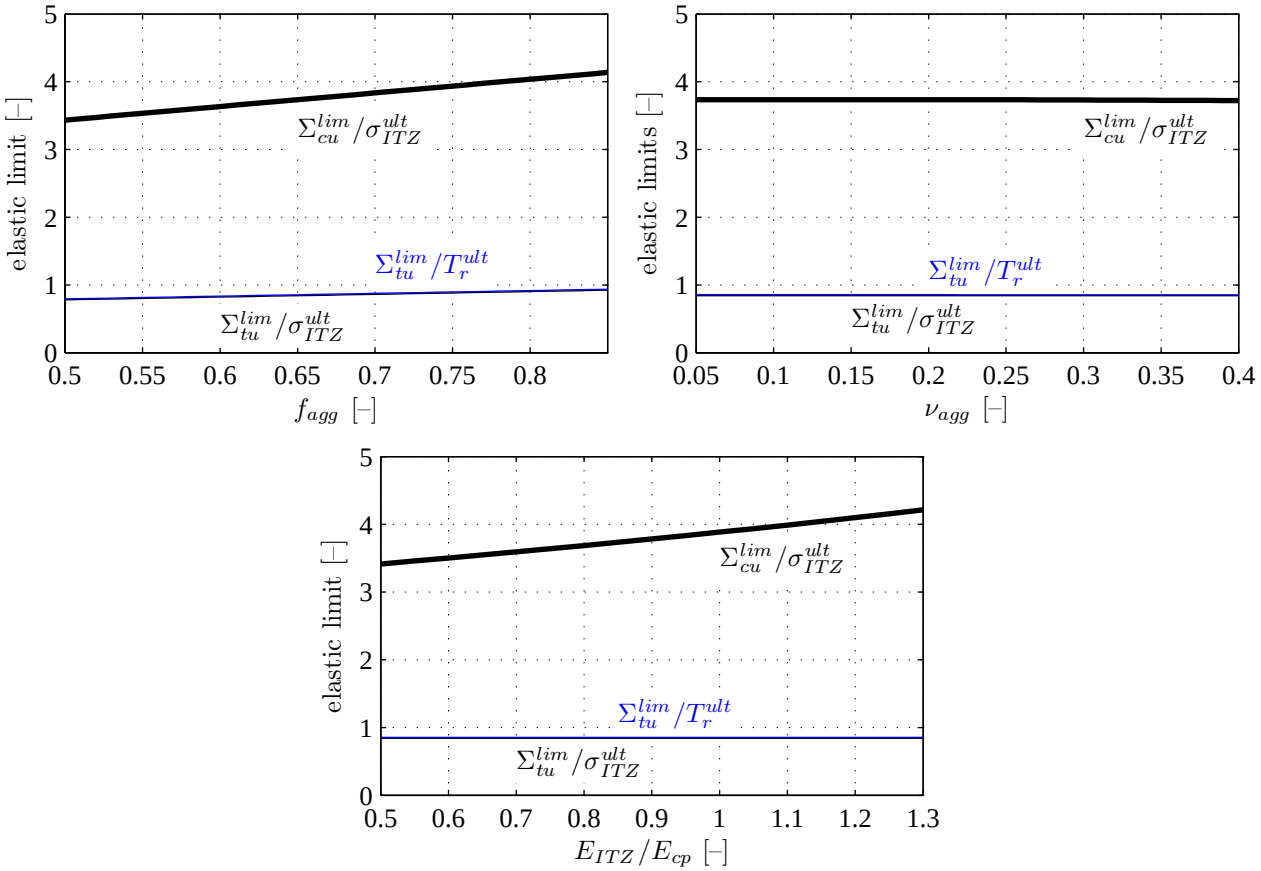

Figure 5.2: Dimensionless elastic limits for concrete properties according to (3.53) whereby one parameter varies within the interval (5.15) (5.16), and (5.17), respectively.

When varying the dimensionless quantity E_{agg}/E_{cp}, we obtain elastic limit expressions which are markedly nonlinear. Result obtained for uniaxial compression motivate us to discuss our model predictions in three intervals, see also Fig. 5.1

$$\frac{E_{agg}}{E_{cp}} = \begin{cases} (0\,,0.42) & \dots \quad \text{regime 1} \\ (0.42\,,0.85) & \dots \quad \text{regime 2} \\ (0.85\,,20.0] & \dots \quad \text{regime 3} \end{cases} \tag{5.18}$$

We discuss these three regimes, starting with regime 3, and ending with regime 1.

- In regime 3, the Young's modulus of the aggregates is larger than the one of the ITZ, because $E_{ITZ}/E_{cp} = 0.85$, i.e.

  $$E_{agg} > E_{ITZ} = 0.85\,E_{cp} \tag{5.19}$$

  The elastic limits $\Sigma_{tu}^{lim}/T_r^{ult}$, $\Sigma_{tu}^{lim}/\sigma_{ITZ}^{ult}$, and $\Sigma_{cu}^{lim}/\sigma_{ITZ}^{ult}$ decrease monotonously with increasing stiffness contrast, since aggregates (which are stiffer than cement paste) attract more loading and therefore the failure governing microstresses are larger. This is detailed next.

  Under uniaxial compression, the position (at which the ITZ failure criterion implies onset of

cracking) increases from $\phi = 1.0455\,\text{rad}$ at $E_{ITZ}/E_{cp} = 20.0$ to $\phi = \pi/2$ at $E_{ITZ}/E_{cp} = 0.85$. In other words, the smaller the stiffness contrast between aggregates and cement paste, the closer to the equator ITZ failure is predicted by the model.

Under uniaxial tension, debonding is always predicted to happen at the poles ($\phi = 0$). The position (at which the ITZ failure criterion implies onset of cracking) increases from $\phi = 0.3369\,\text{rad}$ at $E_{ITZ}/E_{cp} = 20.0$ to $\phi = \pi/2$ at $E_{agg}/E_{cp} = 0.85$. This implies that – for $E_{agg} = E_{ITZ} < 0.85\,E_{cp}$ – the longitudinal normal stresses $\sigma_{ITZ,\phi\phi}$ at the equator, i.e. the normal stresses aligned with the direction of macroscopic tensile loading, are the largest of all maximum principal ITZ stresses.

- In regime 2, the aggregates are the most compliant phase, followed by the ITZ, and the bulk cement paste is the stiffest constituent of concrete:

$$E_{agg} < E_{ITZ} = 0.85\,E_{cp} \tag{5.20}$$

Such stiffness contrast are only realistic for lightweight aggregate concrete, with well hardened cement paste matrix.

Under uniaxial compression, the elastic limit for ITZ failure is equal to the elastic limit for debonding, and both criteria predict onset of cracking at the equator. This implies that the radial stress component at the equator is the largest radial normal stress transferred across the two-dimensional aggregate-ITZ interface [$\max_{\phi,\theta} T_r = T_r(\phi = \pi/2, \theta)$]. At the same time, it is also the largest maximum principal ITZ stress [$\max_{\phi,\theta} \sigma_{ITZ,I} = \sigma_{ITZ,rr}(\phi = \pi/2, \theta)$]; recall the equilibrium-related stress continuity condition $T_r(\phi = \pi/2, \theta) = \sigma_{ITZ,rr}(\phi = \pi/2, \theta)$.

- In regime 1, the stiffness of the aggregates is significantly smaller than the ITZ:

$$E_{agg} < 2\,E_{ITZ} \qquad \text{and} \qquad E_{ITZ} = 0.85\,E_{cp} \tag{5.21}$$

Such stiffness contrast are only realistic for lightweight concretes with extremely compliant aggregates, with well hardened cement paste matrix.

Under uniaxial compression, onset of ITZ failure is predicted to happen at the poles ($\phi = 0$). This implies that the lateral in-plane normal stress $\sigma_{ITZ,\phi\phi} = \sigma_{ITZ,\theta\theta}$ at the poles are the largest of all maximum principal ITZ stresses.

Considering uniaxial tension, we do not have to distinguish between regime 1 and 2. Debonding is always predicted to happen at the poles ($\phi = 0$) and ITZ failure is always predicted to happen at the equator. In this context, it is interesting to study the limiting case of $E_{agg} \to 0$, i. e. the situation in which the aggregate inclusions become spherical pores which are surrounded by thin ITZs. The stress concentration into the inclusion tends to zero if $E_{agg} \to 0$. As for debonding, we note that also the radial normal stresses acting on the surface of the inclusion tend to zero with $E_{agg} \to 0$, such that the debonding criterion formally predicts a dramatic increase of the tensile elastic limit. In the limiting case $E_{agg} \to 0$, the stress trajectories will run around the pore, i.e. through the ITZ and the

adjacent cement paste matrix, leading to a significant stress concentration in the equatorial region. There, the circumferential normal stresses $\sigma_{ITZ,\phi\phi}$ will dramatically increase with decreasing aggregate stiffness, such that the ITZ failure criterion predicts a significant decrease of the tensile elastic limit if $E_{agg} \to 0$. We conclude that, for very small aggregate stiffness and under uniaxial tension, ITZ failure in the equatorial region is much more likely than debonding at the poles.

As for the sensitivity analysis concerning the aggregate dosage, we note that model predicted elastic limits increase with increasing aggregate dosage, see Fig. 5.2. This behavior is driven by the stress concentration from the macroloading down to the aggregate stresses. In this context, we note that the stiffness contrast between cement paste and aggregates is kept constant. It is interesting to discuss the mathematical limit case $f_{agg} \to 1$ in which the microstructure would be uniform, such that a uniform microscopic stress field with *no stress fluctuations* would be obtained. Therefore, the larger the aggregate dosage, the less pronounced is the heterogeneity of the microstructure, and the smaller is the stress concentration in the aggregates.

Poisson's ratio of the aggregates has virtually no influence on the elastic limits predicted by the model, see Fig. 5.2. This implies that – for the considered stiffness contrasts $E_{agg} = 6\,E_{cp}$ and $E_{ITZ} = 0.85\,E_{cp}$ – the Poisson effect does not contribute significantly to the stress states in typical concrete subjected to macroscopic uniaxial tension or compression.

The sensitivity analysis concerning the ITZ stiffness is discussed next, see Fig. 5.2. Debonding-related elastic limits are not affected by variations of the ITZ stiffness, because debonding is driven by $T_r = \sigma_{agg,rr}$ which follows from observation scale A without considering an ITZ. Notably, the ITZ failure-related elastic limits under uniaxial tension is also virtually independent of the ITZ stiffness. Under uniaxial compression, in turn, the elastic limits increase with increasing ITZ stiffness. While this appears to be intuitive from a macroscopic viewpoint (*larger* ITZ stiffness results in larger elastic limits), the micromechanical reason is quite delicate. Therefore, we take the liberty to discuss this effect in some detail. Under uniaxial loading, three stress components of the ITZ are nonzero: $\sigma_{ITZ,rr}$ $\sigma_{ITZ,r\phi}$, and $\sigma_{ITZ,\phi\phi}$. The two components $\sigma_{ITZ,rr}$ and $\sigma_{ITZ,r\phi}$ are equal to corresponding aggregate stress components ($\sigma_{agg,rr}$ and $\sigma_{agg,r\phi}$) because of the equilibrium-related stress continuity condition. Therefore, $\sigma_{ITZ,rr}$ and $\sigma_{ITZ,r\phi}$ are independent of the ITZ stiffness. The ITZ stiffness exclusively concerns the remaining ITZ stress component $\sigma_{ITZ,\phi\phi}$, and the absolute value of the latter increases with increasing ITZ stiffness. This increase of $\sigma_{ITZ,\phi\phi}$, however, results in a *decrease* of the largest maximum principal ITZ stress. At the position of the maximum of the largest principal ITZ normal stress $\max_{\phi,\theta} \sigma_{ITZ,I}$, the normal stress component $\sigma_{ITZ,rr}$ is compressive and its absolute value is smaller than the shear stress $\sigma_{agg,r\phi}$; the normal stress component $\sigma_{ITZ,\phi\phi}$ is also compressive, but its absolute value is smaller than the one of $\sigma_{ITZ,rr}$, see the Mohr circles illustrated in Fig. 5.3. If the absolute value of $\sigma_{ITZ,\phi\phi}$ increases, the distance of the two normal stresses $\sigma_{ITZ,rr}$ and $\sigma_{ITZ,\phi\phi}$ decreases. This moves the center of the Mohr circle in the direction of the compressive normal stresses and, at the same time, it slightly decreases the radius of the Mohr circle. This explains why an increase of $\sigma_{ITZ,\phi\phi}$ results in a *decrease* of the largest maximum principal ITZ stress and, therefore, in an increase of the elastic limit.

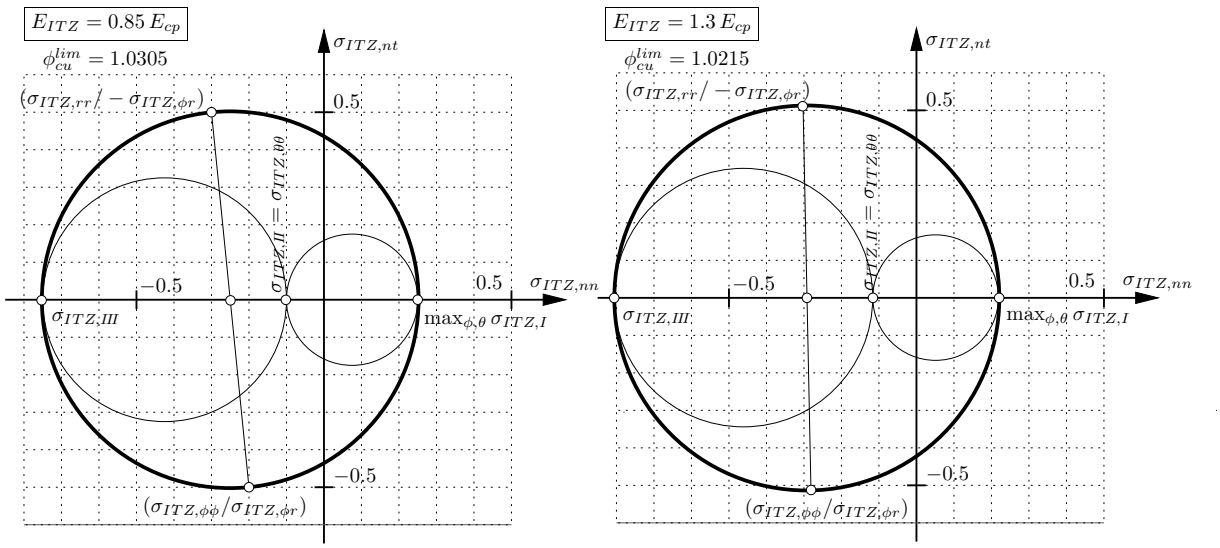

Figure 5.3: Stress representation of $\boldsymbol{\sigma}_{ITZ}$ in Mohr's stress space under uniaxial compression at the position at the interface where the maximum of the largest principal ITZ stress is obtained $\phi = \phi_{cu}^{lim}$ for material parameters according to (3.53) ($E_{ITZ}/E_{cp} = 0.85$, left) and for a ITZ which is stiffer than the bulk paste $E_{ITZ}/E_{cp} = 1.3$ (right): the longitudinal ITZ stress component $\sigma_{ITZ,\phi\phi}$ decreases with increasing ITZ stiffness yielding a shift of the center of the largest circle towards the compressive region, which, in turn, leads to a smaller maximum of the largest principal stress $\max_{\phi,\theta}\sigma_{ITZ,I}$

Chapter 6

Summary, conclusions, and future outlook

Herein we considered concrete to be a matrix-inclusion composite, consisting of aggregates embedded in a continuous cement paste matrix, with thin (but three-dimensional) interfacial transition zones (ITZs) in between. A continuum micromechanics model provided analytical access to the relation between macroscopic loading imposed on representative concrete volumes, on the one hand, and (i) traction vectors acting on the surface of spherical concrete aggregates as well as (ii) the three-dimensional stress states inside the surrounding ITZs, on the other hand. Based on knowledge regarding microscopic tractions and stresses, we formulated tension-based elastic limit criteria for debonding and ITZ failure, respectively. The two microscopic Rankine-type elastic limit criteria were upscaled to elastic limit surfaces in principal stress space of concrete macrostresses: a three-cornered pyramid in case of debonding, and an irregular-shaped six-sided pyramid in case of ITZ failure, with pyramid axes coinciding in both cases with the hydrostatic axis. This result underlines that simple physical laws defined at the microscale are frequently related to rather complex macroscopic behavior, such as observed during testing of microheterogeneous materials. Finally, model predictions were compared with corresponding experimental observations, and the sensitivity of model predictions was studied with respect to the stiffness of aggregates, cement paste, and the ITZ, as well as to the dosage and Poisson's ratio of the aggregates.

The presented continuum micromechanics approach is well suited to study the influence of phase properties (such volume fractions as well as stiffnesses of aggregates, cement paste, and the ITZ) on the macroscopic behavior of concrete. Regarding the influence of the stiffness difference between aggregates and cement paste on onset of microcracking, the models suggest the following conclusions:

- Under macroscopic uniaxial compression, elastic limits of typical concretes are governed by ITZ failure. ITZ failure will start at positions somewhere between the poles and the equator and, there, the first ITZ cracks will propagate – practically speaking – in the direction of macroscopic compressive loading. The elastic limits increase with decreasing aggregate stiffness, because the stress concentration from the macroloading down to stress states in aggregates decreases with

decreasing aggregate stiffness. For lightweight aggregates, however, the situation appears to be much more complex, because ITZ failure at the intersection of the axis of loading with the spherical aggregates competes with debonding in lateral parts.

- Under macroscopic uniaxial tension, the stiffness difference between aggregates and cement paste plays only a significant role, if aggregates are similarly compliant as or even more compliant than the cement paste matrix. This is realistic for lightweight concretes. The more compliant the aggregates, the more likely ITZ failure will be responsible for onset of microcracking. This is caused by stress concentrations stemming from stress trajectories running around the weak aggregates.

As for the sensitivity of microcracking with respect to other concrete properties, the models suggest the following conclusions:

- The larger the aggregate content, the larger the elastic limits of concrete, because the stress concentration from the macroloading down to stress states in aggregates decreases with increasing aggregate dosage.

- Poisson's ratio of the aggregates as well as the stiffness contrast between ITZ and cement paste, in turn, have virtually no influence on elastic limits of concrete.

Regarding the influence of the macroscopic loading type on onset of microcracking, the models suggest the following conclusions:

- For compression-dominated types of macroloading, microcracking is likely to start in the ITZ, because the debonding criterion predicts elastic limits which are by far too large compared to experimental measurements.

- If the ITZ strength is smaller than the bond strength, ITZ failure is relevant for the elastic limits of concrete, independent from the specific type of macroloading. This is likely to be the case (i) for aggregates with strong microroughness, providing a good mechanical interlock between the aggregates and the ITZ and (ii) for aggregate types which react with the pore water solution, resulting in chemical compounds exhibiting a larger strength than the usual hydration products.

- Debonding, in turn, appears to be relevant for tension-dominated types of macroloading, if the ITZ strength is larger than the bond strength. This is likely to be the case for aggregates exhibiting a rather smooth surface, which are made from a material which does not react with the pore solution.

The model considers perfect bond in all observation scale-specific interfaces, such that it is well suited to describe onset of microcracking, but the description of the following evolution of the cracking process is out of reach. Once onset of ITZ failure or debonding takes place under general types of macroscopic loading, namely, the bond properties between the aggregates and the cement paste matrix are heterogeneously distributed over the aggregates' surfaces: in the debonded region, no tractions are

transmittable anymore, but a displacement jump will develop, while in the still bonded regions, the displacement jump will be equal to zero, but tractions will still be transferred across the interface.[1] A solution to this problem is available for the two-dimensional case of a circular inclusion in an infinite matrix, in plane elastostatics [80]. In three dimensions, Chen et al. presented a series solution for an axisymmetric conduction problem [21], but no approach for a stress analysis is available. While this provides a lot of motivation for future work on this topic, we focus on macroscopic uniaxial tension, and we discuss that onset of debonding and onset of ITZ failure, respectively, might well result in different types of subsequent microcrack evolution.

- If debonding is relevant for onset of microcracking, this process will start at the intersection of the axis of loading with the aggregate sphere, i. e. at the poles. Microcracking will result in load re-distributions, i. e. tensile forces which were formerly transmitted from the aggregates to the ITZ have to be taken over in more lateral parts of the interface, i. e. right ahead of the crack edge. These stress concentrations ahead of the crack edge will result in a catastrophic domino effect: the bond crack will continue to propagate until also the ITZ ahead of the crack edge can no longer sustain its loading. At that point, the crack will continue to propagate through the cement paste matrix, and this marks the beginning of complete disintegration of the concrete specimen. Consequently, onset of debonding is likely to be not only associated with the elastic limit of concrete, but also with the tensile strength of the material. Inverting this line of argumentation, one might conclude that onset of microcracking in concretes showing practically no pre-peak non-linearities under uniaxial tension takes place by debonding.

- If ITZ failure is relevant for onset of microcracking, this process will start at positions somewhere between the poles and the equator and, there, the first ITZ cracks will propagate – practically speaking – in a plane which is normal to the direction of macroscopic tensile loading. Once the first crack has propagated throughout the 15 micron thick ITZ, such that it connects the aggregate's surface with the bulk cement paste matrix, it is likely that the crack arrests. The crack, namely will be rather small, such that corresponding stress-redistributions need not necessarily result in bond failure or in failure of the bulk cement paste matrix. Inverting this line of argumentation, one might conclude that onset of microcracking in concretes showing pronounced pre-peak non-linearities under uniaxial tension takes place by ITZ failure.

[1] These conditions are frequently referred to as unilateral constraints, and interfaces with position-dependent properties are often referred to as inhomogeneous imperfect interfaces.

Bibliography

[1] T. Akçaoglu, M. Tokyay, and T. Çelik. Effect of coarse aggregate size on interfacial cracking under uniaxial compression. *Materials letters*, 57(4):828–833, 2002.

[2] T. Akçaoğlu, M. Tokyay, and T. Çelik. Effect of coarse aggregate size and matrix quality on ITZ and failure behavior of concrete under uniaxial compression. *Cement and Concrete Composites*, 26(6):633–638, 2004.

[3] A. Al-Ostaz, H. Al-Moussawi, and L.T. Drzal. Characterization of the interphase in glass sphere reinforced polymers. *Composites Part B: Engineering*, 35(5):393–412, 2004.

[4] KM Alexander. Strength of the cement aggregate bond. In *ACI Journal Proceedings*, volume 56, pages 377–390. ACI, 1959.

[5] K.M. Alexander, J. Wardlaw, and D.J. Gilbert. Aggregate-cement bond, cement paste strength and the strength of concrete. In *The structure of concrete and its behaviour under load: proceedings of an International Conference, London, September 1965*, pages 59–81. Cement & Concrete Association, 1968.

[6] F. Ansari. Stress-strain response of microcracked concrete in direct tension. *ACI Materials Journal*, 84(6):481–490, 1987.

[7] M.J. Aquino, Z. Li, and S.P. Shah. Mechanical properties of the aggregate and cement interface. *Advanced Cement Based Materials*, 2(6):211–223, 1995.

[8] T.B. Aulia. Strain localization and fracture energy of high strength concrete under uniaxial compression. *Leipzig Annual Civil Engineering Report*, 5:221–240, 2000.

[9] R.V. Balendran. Estimating the elastic modulus of concrete made with artificially manufactured lightweight aggregates. *Structural Survey*, 13(2):16–20, 1995.

[10] G.I. Barenblatt. *Scaling, Self-similarity, and Intermediate Asymptotics: Dimensional Analysis and Intermediate Asymptotics*. Cambridge Texts in Applied Mathematics. Cambridge University Press, 1996.

[11] J.D. Bass. Elasticity of minerals, glasses, and melts. *Mineral physics and crystallography: A handbook of physical constants*, 2:45–63, 1995.

[12] Y. Benveniste. A new approach to the application of Mori-Tanaka's theory in composite materials. *Mechanics of Materials*, 6(2):147–157, 1987.

[13] D. Bigoni and A. Piccolroaz. Yield criteria for quasibrittle and frictional materials. *International Journal of Solids and Structures*, 41(11):2855–2878, 2004.

[14] I. Blechman. Brittle solid under compression. Part I: Gradient mechanisms of microcracking. *International Journal of Solids and Structures*, 34(20):2563–2581, 1997.

[15] T.W. Bremner and T.A. Holm. Elastic compatibility and the behavior of concrete. In *ACI Journal Proceedings*, volume 83, pages 244–250. ACI, 1986.

[16] T.W. Bremner and T.A. Holm. High performance lightweight concrete – a review. In *Proc., 2nd CANMET/ACI International Symposium on Advances in Concrete Technology, ACI SP-154, VM Malhotra, ed., American Concrete Institute, Farmington Hills, Mich*, pages 1–19, 1995.

[17] E. Buckingham. On physically similar systems; illustrations of the use of dimensional equations. *Physical Review*, 4(4):345–376, 1914.

[18] O. Buyukozturk, A.H. Nilson, and F.O. Slate. Stress-strain response and fracture of a concrete model in biaxial loading. *ACI Journal*, 68(8):590–599, 1971.

[19] S. Caliskan. Aggregate/mortar interface: influence of silica fume at the micro- and macro-level. *Cement and Concrete Composites*, 25(4):557–564, 2003.

[20] S. Chatterji and J.W. Jeffery. Three-dimensional arrangement of hydration products in set cement paste. *Nature*, 209:1233–1234, 1966.

[21] T. Chen, C.H. Hsieh, and P.C. Chuang. A spherical inclusion with inhomogeneous interface in conduction. *Journal of Mechanics*, 19(1):1–8, 2003.

[22] W. Chuan-Zhi, G. Zhen-Hai, G. Zhen-Hai, and Z. Xiu-Qin. Experimental investigation of biaxial and triaxial compressive concrete strength. *ACI Materials Journal*, 84(2):92–100, 1987.

[23] G. Constantinides and F.-J. Ulm. The nanogranular nature of C–S–H. *Journal of the Mechanics and Physics of Solids*, 55(1):64–90, 2007.

[24] S.C. Cowin and M.M. Mehrabadi. The structure of the linear anisotropic elastic symmetries. *Journal of the Mechanics and Physics of Solids*, 40(7):1459–1471, 1992.

[25] M. Creath, J.B. Newman, and K. Newman. The influence of aggregate particles on the local strain distribution and fracture mechanism of cement paste during drying shrinkage and loading to failure. *Materials and Structures*, 2(1):73–85, 1969.

[26] A.K. Crumbie. *Characterisation of the microsctructure of concrete*. PhD thesis, Department of Materials, Imperial College, London, 1983.

[27] J. Desrues, P. Bésuelle, and H. Lewis. Strain localization in geomaterials. *Geological Society, London, Special Publications*, 289(1):47–73, 2007.

[28] S. Diamond and J. Huang. The ITZ in concrete – a different view based on image analysis and SEM observations. *Cement and Concrete Composites*, 23(2):179–188, 2001.

[29] L. Dormieux. Course de mecanique: Milieu continu tridimensional, construction des efforts intérieurs [Course on mechanics: three-dimensional continuum, estimation of internal forces]. Lecture notes, 2007. in French.

[30] eFunda. efunda – Properties of common solid materials. `http://www.efunda.com/materials/common_matl/common\_matl.cfm`. online, accessed 04/10/2012.

[31] J.D. Eshelby. The determination of the elastic field of an ellipsoidal inclusion, and related problems. *Proceedings of the Royal Society London, Ser. A*, 241(1226):376–396, 1957.

[32] Z. Gao. A circular inclusion with imperfect interface: Eshelbys tensor and related problems. *Journal of Applied Mechanics*, 62:860–866, 1995.

[33] A.N. Gent and B. Park. Failure processes in elastomers at or near a rigid spherical inclusion. *Journal of Materials Science*, 19(6):1947–1956, 1984.

[34] A. Goldman and A. Bentur. Bond effects in high-strength silica fume concretes. *ACI Materials Journal*, 86(5):440–449, 1989.

[35] Z. Hashin. Analysis of composite materials – a survey. *Journal of Applied Mechanics, Transactions ASME*, 50(3):481–505, 1983.

[36] Z. Hashin. Thermoelastic properties of particulate composites with imperfect interface. *Journal of the Mechanics and Physics of Solids*, 39(6):745–762, 1991.

[37] Z. Hashin and P.J.M. Monteiro. An inverse method to determine the elastic properties of the interphase between the aggregate and the cement paste. *Cement and Concrete Research*, 32(8):1291–1300, 2002.

[38] M.K. Head, H.S. Wong, and N.R. Buenfeld. Characterising aggregate surface geometry in thin-sections of mortar and concrete. *Cement and Concrete Research*, 38(10):1227–1231, 2008.

[39] R.A. Helmuth and D.H. Turk. Elastic moduli of hardened cement paste and tricalcium silicate pastes: Effect of porosity. In *Proceedings of a Symposium on the Structure of Portland Cement Paste and Concrete, Highway Research Board Sp. Rep. 90, National Academy of Engineering, Washington, DC*, pages 135–144, 1966.

[40] R. Hill. Elastic properties of reinforced solids: Some theoretical principles. *Journal of the Mechanics and Physics of Solids*, 11(5):357–372, 1963.

[41] T.T.C. Hsu and F.O. Slate. Tensile bond strength between aggregate and cement paste or mortar. In *ACI Journal Proceedings*, volume 60, pages 465–486. ACI, 1963.

[42] T.T.C. Hsu, F.O. Slate, G.M. Sturman, and G. Winter. Microcracking of plain concrete and the shape of the stress-strain curve. In *ACI Journal Proceedings*, volume 60, pages 209–224. ACI, 1963.

[43] S. Igarashi, A. Bentur, and S. Mindess. Microhardness testing of cementitious materials. *Advanced Cement Based Materials*, 4(2):48–57, 1996.

[44] R.P. Janeiro and H.H. Einstein. Experimental study of the cracking behavior of specimens containing inclusions (under uniaxial compression). *International Journal of Fracture*, 164(1):83–102, 2010.

[45] R. Jones. A method of studying the formation of cracks in a material subjected to stress. *British Journal of Applied Physics*, 3:229–232, 1952.

[46] H. Kupfer, H.K. Hilsdorf, and H. Rusch. Behavior of concrete under biaxial stresses. In *ACI Journal Proceedings*, volume 66, pages 656–666. ACI, 1969.

[47] E.N. Landis and J.E. Bolander. Explicit representation of physical processes in concrete fracture. *Journal of Physics D: Applied Physics*, 42(21):214002–214018, 2009.

[48] N. Laws. The determination of stress and strain concentrations at an ellipsoidal inclusion in an anisotropic material. *Journal of Elasticity*, 7(1):91–97, 1977.

[49] G. Li, Y. Zhao, S.S. Pang, and Y. Li. Effective Young's modulus estimation of concrete. *Cement and Concrete Research*, 29(9):1455–1462, 1999.

[50] Z. Li and S.P. Shah. Localization of microcracking in concrete under uniaxial tension. *ACI Materials Journal*, 91(4):372–381, 1994.

[51] C.C. Lim, N. Gowripalan, and V. Sirivivatnanon. Microcracking and chloride permeability of concrete under uniaxial compression. *Cement and Concrete Composites*, 22(5):353–360, 2000.

[52] T.C.Y. Liu, A.H. Nilson, and F.O.S. Floyd. Stress-strain response and fracture of concrete in uniaxial and biaxial compression. In *ACI Journal Proceedings*, volume 69, pages 291–295. ACI, 1972.

[53] T.Y. Lo and H.Z. Cui. Effect of porous lightweight aggregate on strength of concrete. *Materials Letters*, 58(6):916–919, 2004.

[54] W. Lode. Versuche über den Einfluß der mittleren Hauptspannung auf das Fließen der Metalle Eisen, Kupfer und Nickel [Experiments regarding the influence of the mean principal strsss on yielding of metals: iron, copper, and nickel. *Zeitschrift für Physik A Hadrons and Nuclei*, 36(11):913–939, 1926. in German.

[55] A.K. Maji and S.P. Shah. Application of acoustic emission and laser holography to study microfracture in concrete. *ACI - Special Publication*, 112:83–109, 1989.

[56] H.A. Mang and G. Hofstetter. *Festigkeitslehre [Strength of Materials]*. Springer-Verlag, 2000.

[57] I.C. Mihai and A.D. Jefferson. A material model for cementitious composite materials with an exterior point Eshelby microcrack initiation criterion. *International Journal of Solids and Structures*, 48(24):3312–3325, 2011.

[58] S. Mindess and S. Diamond. SEM investigations of fracture surfaces using stereo pairs: II fracture surfaces of rock-cement paste composite specimens. *Cement and Concrete Research*, 22(4):678–688, 1992.

[59] K. Mitsui, Z. Li, D.A. Lange, and S.P. Shah. Relationship between microstructure and mechanical properties of paste-aggregate interface. *ACI Materials Journal*, 91(1):30–39, 1994.

[60] P. Mondal. *Nanomechanical properties of cementitious materials*. PhD thesis, Nothwestern University, Evanston, Illinois, 2008.

[61] P. Mondal, S. P. Shah, and L. D. Marks. Nanomechanical properties of interfacial transition zone in concrete. In Zdenk Bittnar, Peter J. M. Bartos, Ji Nmeek, Vt milauer, and Jan Zeman, editors, *Nanotechnology in Construction 3*, pages 315–320. Springer Berlin Heidelberg, 2009.

[62] T. Mori and K. Tanaka. Average stress in matrix and average elastic energy of materials with misfitting inclusions. *Acta Metallurgica*, 21(5):571–574, 1973.

[63] J. Müller-Rochholz. Determination of the elastic properties of lightweight aggregate by ultrasonic pulse velocity measurement. *International Journal of Cement Composites and Lightweight Concrete*, 1(2):87–90, 1979.

[64] J.C. Nadeau. A multiscale model for effective moduli of concrete incorporating ITZ water-cement ratio gradients, aggregate size distributions, and entrapped voids. *Cement and Concrete Research*, 33(1):103–113, 2003.

[65] G.C. Nayak and O.C. Zienkiewicz. Elasto-plastic stress analysis. A generalization for various contitutive relations including strain softening. *International Journal for Numerical Methods in Engineering*, 5(1):113–135, 1972.

[66] J.P. Ollivier, J.C. Maso, and B. Bourdette. Interfacial transition zone in concrete. *Advanced Cement Based Materials*, 2(1):30–38, 1995.

[67] C. Perry and J.E. Gillott. The influence of mortar-aggregate bond strength on the behaviour of concrete in uniaxial compression. *Cement and Concrete Research*, 7(5):553–564, 1977.

[68] B. Pichler and C. Hellmich. Upscaling quasi-brittle strength of cement paste and mortar: A multi-scale engineering mechanics model. *Cement and Concrete Research*, 41(5):467–476, 2011.

[69] B. Pichler, C. Hellmich, and J. Eberhardsteiner. Spherical and acicular representation of hydrates in a micromechanical model for cement paste: Prediction of early-age elasticity and strength. *Acta Mechanica*, 203(3-4):137–162, 2009.

[70] G.A. Rao and B.K. Prasad. Influence of the roughness of aggregate surface on the interface bond strength. *Cement and Concrete Research*, 32(2):253–257, 2002.

[71] J. Rychlewski. On Hooke's law. *Prikladnaya Matematika i Mekhanika*, 48(3):420–435, 1984.

[72] M. Saito. Characteristics of microcracking in concrete under static and repeated tensile loading. *Cement and Concrete Research*, 17(2):211–218, 1987.

[73] J. Salençon. *Handbook of continuum mechanics: general concepts, Thermoelasticity*. Springer Verlag, 2001.

[74] K.L. Scrivener, A. Bentur, and P.L. Pratt. Quantitative characterization of the transition zone in high strength concretes. *Advances in Cement Research*, 1(4):230–237, 1988.

[75] K.L. Scrivener, A.K. Crumbie, and P. Laugesen. The interfacial transition zone (ITZ) between cement paste and aggregate in concrete. *Interface Science*, 12(4):411–421, 2004.

[76] S.P. Shah and S. Chandra. Critical stress, volume change, and microcracking of concrete. In *ACI Journal Proceedings*, volume 65, pages 770–780. ACI, 1968.

[77] S.P. Shah and R. Sankar. Internal cracking and strain softening response of concrete under uniaxial compression. *ACI Materials Journal*, 84(3):200–212, 1987.

[78] S.P. Shah and G. Winter. Inelastic behavior and fracture of concrete. In *ACI Journal Proceedings*, volume 63, pages 925–930. ACI, 1966.

[79] L. Struble, J. Skalny, and S. Mindess. A review of the cement-aggregate bond. *Cement and Concrete Research*, 10(2):277–286, 1980.

[80] L.J. Sudak, C.Q. Ru, P. Schiavone, and A. Mioduchowski. A circular inclusion with inhomogeneously imperfect interface in plane elasticity. *Journal of Elasticity*, 55(1):19–41, 1999.

[81] W.A. Tasong, C.J. Lynsdale, and J.C. Cripps. Aggregate-cement paste interface. II: influence of aggregate physical properties. *Cement and Concrete Research*, 28(10):1453–1465, 1998.

[82] M.E. Tasuji. Stress-strain response and fracture of concrete in biaxial loading. In *ACI Journal Proceedings*, volume 75, pages 306–312. ACI, 1978.

[83] A. Ulrik Nilsen and P.J.M. Monteiro. Concrete: A three phase material. *Cement and Concrete Research*, 23(1):147–151, 1993.

[84] J. Wastiels. Behaviour of concrete under multiaxial stresses – a review. *Cement and Concrete Research*, 9(1):35–44, 1979.

[85] E.W. Weisstein. Spherical coordinates. `http://mathworld.wolfram.com/SphericalCoordinates.html`. online, accessed 05/06/2012.

[86] A. Zaoui. Continuum micromechanics: Survey. *Journal of Engineering Mechanics*, 128(8):808–816, 2002.

[87] J. Zheng, X. Zhou, and X. Jin. An n-layered spherical inclusion model for predicting the elastic moduli of concrete with inhomogeneous ITZ. *Cement and Concrete Composites*, 34(5):716–723, 2012.

[88] W. Zhu and P.J.M. Bartos. Microstructure and properties of interfacial transition zone in SCC. In *SCC'2005-China: 1st International Symposium on Design, Performance and Use of Self-Consolidating Concrete*, pages 319–327. RILEM Publications SARL, 2005.

[89] R. Zimbelmann. A contribution to the problem of cement-aggregate bond. *Cement and Concrete Research*, 15(5):801–808, 1985.

Appendix A

Comments on isotropic fourth-order tensors

A.1 Volumetric and deviatoric part of isotropic fourth-order tensors

An isotropic fourth-order tensor, $\mathbb{G}$, can be decomposed into a volumetric part and a deviatoric part. Considering two tensors $\mathbb{G}$ and $\mathbb{H}$, this decomposition reads as

$$\begin{aligned} \mathbb{G} &= G_{vol}\mathbb{J} + G_{dev}\mathbb{K} \\ \mathbb{H} &= H_{vol}\mathbb{J} + H_{dev}\mathbb{K} \end{aligned} \tag{A.1}$$

where G_{vol}, G_{dev}, H_{vol}, and H_{dev} are scalars, where $\mathbb{J}$ stands for the volumetric part of the fourth-order unity tensor $\mathbb{I}$, reading as

$$\mathbb{J} = \frac{1}{3}\,\mathbf{1}\otimes\mathbf{1} \tag{A.2}$$

with $\mathbf{1}$ as the second-order unity tensor with components equal to Kronecker delta δ_{ij}, and where $\mathbb{K}$ stands for the deviatoric part of the symmetric fourth-order unity tensor

$$\mathbb{K} = \mathbb{I} - \mathbb{J}. \tag{A.3}$$

The definition of the components of the fourth-order unity tensor, given in Sec. 3.1, is herein recalled:

$$I_{ijkl} = \frac{1}{2}\left(\delta_{ik}\delta_{jl} + \delta_{il}\delta_{kj}\right) \tag{A.4}$$

Volumetric and deviatoric part of the symmetric fourth-order identity tensor satisfy

$$\mathbb{J} : \mathbb{J} = \mathbb{J} \qquad \mathbb{K} : \mathbb{K} = \mathbb{K} \qquad \mathbb{J} : \mathbb{K} = \mathbb{K} : \mathbb{J} = O\,. \tag{A.5}$$

Eq. (A.5) implies that the double-contraction of two isotropic tensors, $\mathbb{G}$ and $\mathbb{H}$, can be written as simple as:

$$\mathbb{G} : \mathbb{H} = G_{vol}H_{vol}\mathbb{J} + G_{dev}H_{dev}\mathbb{K}. \tag{A.6}$$

The inversion of an isotropic fourth-order tensor reads as

$$\mathbb{G}^{-1} = (G_{vol}\mathbb{J} + G_{dev}\mathbb{K})^{-1} = \frac{1}{G_{vol}}\mathbb{J} + \frac{1}{G_{dev}}\mathbb{K}\,, \tag{A.7}$$

In order to prove (A.7), note that $\mathbb{G} : \mathbb{G}^{-1} = \mathbb{I} = \mathbb{J} + \mathbb{K}$ and consider $\mathbb{G}$ according to (A.1) as well as $\mathbb{G}^{-1}$ according to (A.7).

A.2 Volumetric and deviatoric parts of concentration tensors and of homogenized stiffness of concrete

Rules (A.6) and (A.7) will now be applied to isotropic fourth-order tensors relevant for homogenization of concrete. We start with the Eshelby problem-related strain concentration tensor

$$\mathbb{A}_{agg}^{\infty} = \left[\mathbb{I} + \mathbb{S}_{sph} : \mathbb{C}_{cp}^{-1} : (\mathbb{C}_{agg} - \mathbb{C}_{cp})\right]^{-1} \tag{A.8}$$

where we recall that

$$\mathbb{S}_{sph} = \alpha\mathbb{J} + \beta\mathbb{K}\,, \qquad \mathbb{C}_j = 3k_j\mathbb{J} + 2\mu_j\mathbb{K} \qquad j \in \{agg, cp\}\,. \tag{A.9}$$

Combination of (A.8) with (A.9) yields, under consideration of (A.6) and (A.7)

$$\begin{aligned}\mathbb{A}_{agg}^{\infty} &= \left[1 + \alpha\frac{1}{3k_{cp}}\left(3k_{agg} - 3k_{cp}\right)\right]^{-1}\mathbb{J} + \left[1 + \beta\frac{1}{2\mu_{cp}}\left(2\mu_{agg} - 2\mu_{cp}\right)\right]^{-1}\mathbb{K} \\ &= \frac{1}{1 + \frac{\alpha(k_{agg}-k_{cp})}{k_{cp}}}\mathbb{J} + \frac{1}{1 + \frac{\beta(\mu_{agg}-\mu_{cp})}{\mu_{cp}}}\mathbb{K}\,.\end{aligned} \tag{A.10}$$

Next, we focus on the strain concentration tensor of the cement paste matrix:

$$\mathbb{A}_{cp} = \left(f_{cp}\mathbb{I} + f_{agg}\mathbb{A}_{agg}^{\infty}\right)^{-1} \tag{A.11}$$

Under consideration of (A.10), (A.6), and (A.7), the decomposition of $\mathbb{A}_{cp}$ into a volumetric and a deviatoric part reads as

$$\mathbb{A}_{cp} = \left[f_{cp} + \frac{f_{agg}}{1 + \frac{\alpha(k_{agg}-k_{cp})}{k_{cp}}}\right]^{-1}\mathbb{J} + \left[f_{cp} + \frac{f_{agg}}{1 + \frac{\beta(\mu_{agg}-\mu_{cp})}{\mu_{cp}}}\right]^{-1}\mathbb{K}\,. \tag{A.12}$$

The strain concentration tensor of the aggregates reads as

$$\mathbb{A}_{agg} = \mathbb{A}_{agg}^{\infty}\left(f_{cp}\mathbb{I} + f_{agg}\mathbb{A}_{agg}^{\infty}\right)^{-1}\,. \tag{A.13}$$

Under consideration of (A.10), (A.6), and (A.7), the decomposition of $\mathbb{A}_{agg}$ into a volumetric and a deviatoric part reads as

$$\begin{aligned}\mathbb{A}_{agg} =& \left(\frac{1}{1+\frac{\alpha(k_{agg}-k_{cp})}{k_{cp}}}\right)\left(f_{cp}+\frac{f_{agg}}{1+\frac{\alpha(k_{agg}-k_{cp})}{k_{cp}}}\right)^{-1}\mathbb{J}+\\ &\left(\frac{1}{1+\frac{\beta(\mu_{agg}-\mu_{cp})}{\mu_{cp}}}\right)\left(f_{cp}+\frac{f_{cp}}{1+\frac{\beta(\mu_{agg}-\mu_{cp})}{\mu_{cp}}}\right)^{-1}\mathbb{K}\,.\end{aligned} \tag{A.14}$$

Finally, the decomposition of the homogenized stiffness

$$\mathbb{C}_{con} = f_{agg}\mathbb{C}_{agg} : \mathbb{A}_{agg} + f_{cp}\mathbb{C}_{cp} : \mathbb{A}_{cp} \tag{A.15}$$

follows from (A.9), (A.12), and (A.14) as

$$\begin{aligned}\mathbb{C}_{con} =& 3\left[f_{cp}k_{cp}+\frac{f_{agg}k_{agg}}{1+\frac{\alpha(k_{agg}-k_{cp})}{k_{cp}}}\right]\left[f_{cp}+\frac{f_{agg}}{1+\frac{\alpha(k_{agg}-k_{cp})}{k_{cp}}}\right]^{-1}\mathbb{J}\\ &+2\left[f_{cp}\mu_{cp}+\frac{f_{agg}\mu_{agg}}{1+\frac{\beta(\mu_{agg}-\mu_{cp})}{\mu_{cp}}}\right]\left[f_{cp}+\frac{f_{agg}}{1+\frac{\beta(\mu_{agg}-\mu_{cp})}{\mu_{cp}}}\right]^{-1}\mathbb{K}\,.\end{aligned} \tag{A.16}$$

Appendix B

Further analytical results for microscopic stress and strain states under macroscopic uniaxial and biaxial loading

The microscopic traction vectors and ITZ stresses under uniaxial loading are discussed in Sec. 3.7. Herein, the corresponding strain states are studied. Average aggregate strains in spherical coordinates follow from the spatially constant Cartesian components (3.30) by the transformation (3.39). Specification of the result for uniaxial loading (3.44) delivers

$$\begin{aligned}
\frac{\varepsilon_{agg,\phi\phi}(\phi)}{\Sigma_{zz}} &= \frac{1}{3}D_{vol} + D_{dev}\left(\frac{2}{3} - \cos^2\phi\right) \\
\frac{\varepsilon_{agg,\theta\theta}(\phi)}{\Sigma_{zz}} &= \frac{1}{3}\left(D_{vol} - D_{dev}\right) \\
\frac{\varepsilon_{agg,rr}(\phi)}{\Sigma_{zz}} &= \frac{1}{3}D_{vol} + D_{dev}\left(\cos^2\phi - \frac{1}{3}\right) \\
\frac{\varepsilon_{agg,\phi r}(\phi)}{\Sigma_{zz}} &= -\frac{1}{2}D_{dev}\sin(2\phi)\,.
\end{aligned} \tag{B.1}$$

Rotational symmetry also holds for the strain components, such that shear strain components containing one index equal to θ are zero, $\varepsilon_{agg,\phi\theta} = \varepsilon_{agg,\theta\phi} = \varepsilon_{agg,\theta r} = \varepsilon_{agg,r\theta} = 0$. Three interfacial strain components in spherical coordinates follow from the strain continuity rule (3.38), the other three are

obtained from $(3.42)_{1,2}$ and $(3.43)_3$ as

$$\begin{aligned}
\frac{\varepsilon_{ITZ,\phi\phi}(\phi)}{\Sigma_{zz}} &= \frac{1}{3}D_{vol} + D_{dev}\left(\frac{2}{3} - \cos^2\phi\right) \\
\frac{\varepsilon_{ITZ,\theta\theta}(\phi)}{\Sigma_{zz}} &= \frac{1}{3}\left(D_{vol} - D_{dev}\right) \\
\frac{\varepsilon_{ITZ,rr}(\phi)}{\Sigma_{zz}} &= \frac{1}{3k_{ITZ} + 4\mu_{ITZ}}\Big\{B_{vol} + B_{dev}\left(3\cos^2\phi - 1\right) \\
&\quad + \frac{1}{3}D_{vol}\left(-6k_{ITZ} + 4\mu_{ITZ}\right) + \frac{1}{3}D_{dev}\left[\cos^2\phi\left(9k_{ITZ} - 6\mu_{ITZ}\right) - 3k_i tz + 2\mu_{ITZ}\right]\Big\} \\
\frac{\varepsilon_{ITZ,\phi r}(\phi)}{\Sigma_{zz}} &= -\frac{1}{4}\frac{B_{dev}\sin(2\phi)}{\mu_{ITZ}}
\end{aligned} \tag{B.2}$$

The strain component $\varepsilon_{ITZ,\theta\theta}$ is constant in the ITZ shell, since the problem is axisymmetric with respect to the z-direction, since a spatially constant strain state is representative within the aggregate, and since strain compatibility implies $\varepsilon_{agg,\theta\theta} = \varepsilon_{ITZ,\theta\theta}$. Specification of the strain states (B.1) and (B.2), for typical concrete properties (3.53) allows for plotting the graphs shown in Fig. B.1.

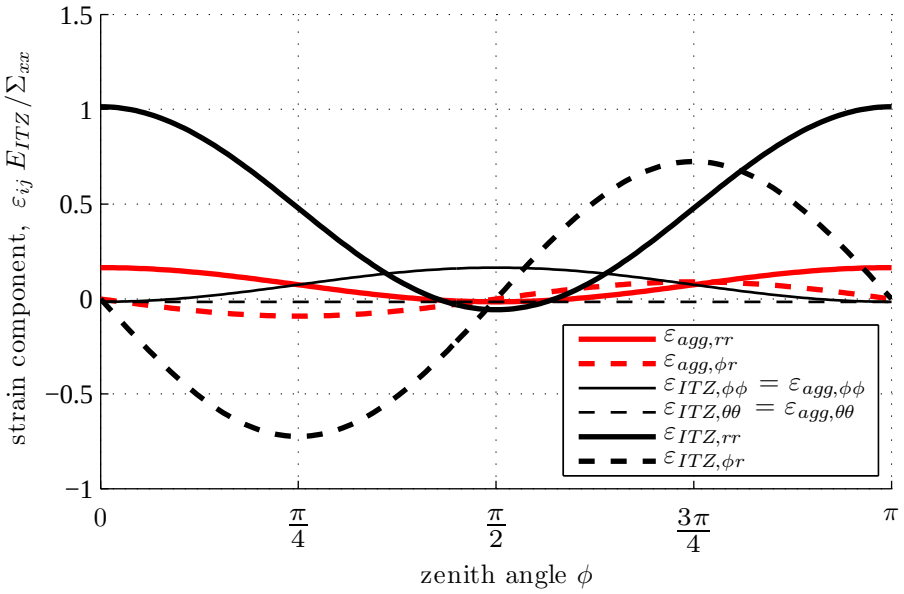

Figure B.1: Dimensionless, nonzero microscopic strain components as a function of zenith angle: aggregate strains and ITZ strains, respectively, under uniaxial loading (3.44), evaluated for elastic properties and aggregate content described in (3.53), see also (3.22), (3.11), and (3.54)

Considering symmetric biaxial loading, $\mathbf{\Sigma} = \Sigma_{xx}\ (\underline{e}_x \otimes \underline{e}_x + \underline{e}_y \otimes \underline{e}_y)$, implies rotational symmetry with respect to the z-axis. Hence, in spherical coordinates, stress and strain components are only a function of the zenith angle ϕ. Since the superposition principal is valid, we can get access to the results for biaxial loading by superimposing two uniaxial stress states, one with loading in global x-

direction, and one with loading in global y-direction, see Figs. B.2 and B.3 for numerical evaluations.

Superposition holds also for microscopic ITZ stress states. For instance, the radial normal stress

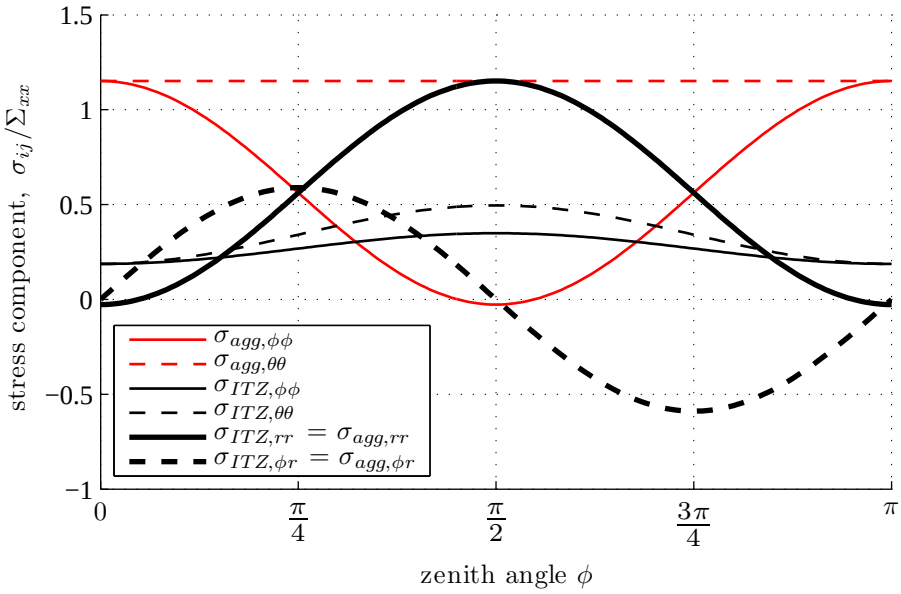

Figure B.2: Dimensionless, nonzero microscopic stress components as a function of zenith angle: aggregate strains, tractions at the aggregate's surface, and ITZ stresses, respectively, under symmetric biaxial loading, $\Sigma_{xx} = \Sigma_{yy}$, specified in (4.8), evaluated for elastic properties and aggregate content described in (3.53), see also (3.22), (3.11), and (3.54)

component at the pole is, under biaxial loading, twice as large as the radial normal stress at the equator under uniaxial loading, compare Figs. 3.3 and B.2. $\sigma_{ITZ,\theta\theta}$ at the north pole under macroscopic biaxial loading is the sum of $\sigma_{ITZ,\theta\theta}$ and $\sigma_{ITZ,\phi\phi}$, at the equator under macroscopic uniaxial loading acting in z-direction.

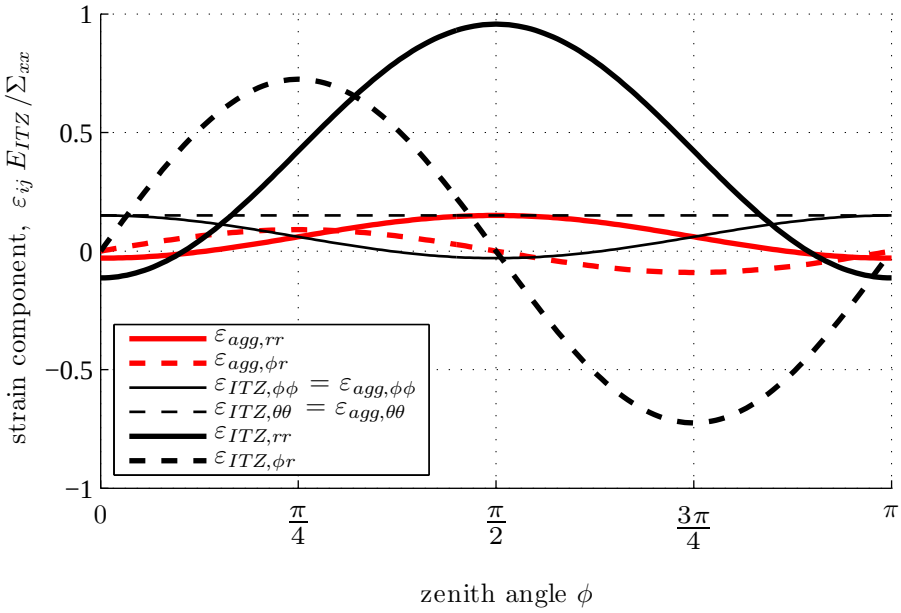

Figure B.3: Dimensionless, nonzero microscopic strain components as a function of zenith angle: aggregate strains and ITZ strains, respectively, under symmetric biaxial loading, $\Sigma_{xx} = \Sigma_{yy}$, specified in (4.8), evaluated for elastic properties and aggregate content described in (3.53), see also (3.22), (3.11), and (3.54)

Appendix C

Principal stress analysis: Solution of the characteristic equation based on Cardano's formula

The solution of a cubic function, given as a monic trinomial, is accessible based on Cardano's method. The transition from the characteristic equation (4.21) to a cubic monomial is performed by dividing Eq. (4.21) by -1 and by extracting the hydrostatic stress using the substitution

$$\Lambda = \sigma - \frac{I_1^\sigma}{3}. \tag{C.1}$$

With the invariants of the microstress deviator, $J_1^s = 0$, J_2^s, and J_3^s, this cubic monomial reads as

$$\Lambda^3 - J_2^s \Lambda - J_3^s = 0. \tag{C.2}$$

J_2^s and J_3^s follow from specification of (4.34) for microscopic quantities or from the invariants of the microscopic stress tensor I_1^σ, I_2^σ, and I_3^σ, see Eq. (4.22), as:

$$J_2^s = \frac{(I_1^\sigma)^2}{3} - I_2^\sigma \qquad J_3^s = I_3^\sigma - \frac{I_1^\sigma I_2^\sigma}{3} + \frac{2\,(I_1^\sigma)^3}{27} \tag{C.3}$$

The solution of the cubic monomial (C.2) involves the Haigh-Westergaard coordinates ρ (deviatoric component) and ϑ (Lode angle), see Eq. (4.35), and read as

$$\begin{aligned} \Lambda_1 &= \frac{\sqrt{6}}{3}\rho\cos\vartheta \\ \Lambda_2 &= \frac{\sqrt{6}}{3}\rho\cos\left(\vartheta - \frac{2\pi}{3}\right) \\ \Lambda_3 &= \frac{\sqrt{6}}{3}\rho\cos\left(\vartheta + \frac{2\pi}{3}\right). \end{aligned} \tag{C.4}$$

Back-substitution of (C.4) into (C.1), i.e. addition of the hydrostatic part of the stress tensor delivers the three sought principal ITZ stresses:

$$\begin{aligned}
\sigma_{ITZ,1} &= \Lambda_1 + \frac{I_1^\sigma}{3} = \frac{\sqrt{3}\xi}{3} + \frac{\sqrt{6}}{3}\rho\cos\vartheta \\
\sigma_{ITZ,2} &= \Lambda_2 + \frac{I_1^\sigma}{3} = \frac{\sqrt{3}\xi}{3} + \frac{\sqrt{6}}{3}\rho\cos\left(\vartheta - \frac{2\pi}{3}\right) \\
\sigma_{ITZ,3} &= \Lambda_3 + \frac{I_1^\sigma}{3} = \frac{\sqrt{3}\xi}{3} + \frac{\sqrt{6}}{3}\rho\cos\left(\vartheta + \frac{2\pi}{3}\right),
\end{aligned} \tag{C.5}$$

and

$$\{\sigma_{ITZ,I}, \sigma_{ITZ,II}, \sigma_{ITZ,III}\} = \{\sigma_{ITZ,1}, \sigma_{ITZ,2}, \sigma_{ITZ,3}\} \quad \text{with} \quad \sigma_{ITZ,I} > \sigma_{ITZ,II} > \sigma_{ITZ,III}\,. \tag{C.6}$$

In (C.5), ξ denotes the hydrostatic component of the Haigh-Westergaard representation according to Eq. (4.35).

Appendix D

Dimensional analysis

A dimensional analysis is beneficial to determine the governing factors responsible for onset of debonding and for analyzing the sensitivity of related model predictions in a systematic fashion. Based on Buckingham's Pi-Theorem [17], any physical law is independent of the arbitrarily chosen units of measurements. Any physical relation can be rewritten as a relationship between a dimensionless parameter, on the one hand, and some dimensionless parameters and several dimensionless products of the governing parameters, on the other hand [10]. This allows for a reduction of the number of arguments in these functions.

Several dimensional and dimensionless parameters have an influence on the onset of debonding and on the onset of ITZ failure, respectively. In this context, we note that, starting from the macroscopic stress state (3.29), we use the micromechanics model to derive the macrostrains. The latter provide, under consideration of the strain concentration tensor of the aggregate phase, access to aggregate strains. Hooke's law of the aggregates leads to aggregate stresses and Cauchy's formula to the traction vectors acting on the aggregate's surface. The radial traction component at the aggregate's surface, T_r, is considered to govern the onset of debonding, see (4.1). Perfect bond conditions, together with Hooke's law of the ITZ, allow for identification of the interfacial stress state. A subsequently performed principal stress analysis leads to the principal ITZ stresses, whereby the largest principal ITZ stress is denoted as $\sigma_{ITZ,I}$ and is considered to be responsible for the onset of ITZ failure, see (4.2). T_r as well as $\sigma_{ITZ,I}$ depend on the position at the aggregate's surface, i.e. they are both functions of the position angles ϕ and θ.

Collecting all parameters needed to compute the radial traction component at the aggregate's surface, allows us to write this stress component as a (dimensional) function ψ_{agg} of the parameters:

$$\sigma_{agg,rr} = T_r = \psi_{agg}\left(\boldsymbol{\Sigma}, E_{agg}, \nu_{agg}, E_{cp}, \nu_{cp}, f_{agg}, \phi, \theta\right) . \tag{D.1}$$

Similarly, we can write down a (dimensional) function ψ_{ITZ} which links the largest principal ITZ stress with all model parameters having an influence. In addition to the quantities in (D.1) the ITZ stiffness (expressed through ITZ's Young's modulus E_{ITZ} and ITZ's Poisson's ratio ν_{ITZ}) influences

the stress state within the ITZ:

$$\sigma_{ITZ,I} = \psi_{ITZ}\left(\mathbf{\Sigma}, E_{agg}, \nu_{agg}, E_{cp}, \nu_{cp}, E_{ITZ}, \nu_{ITZ}, f_{agg}, \phi, \theta\right) . \tag{D.2}$$

Next, dimensional functions of the involved physical properties are introduced and collected in the so-called exponent matrix of dimension, which reads for (D.1) as

	$[T_r]$	$[\mathbf{\Sigma}]$	$[E_{agg}]$	$[\nu_{agg}]$	$[E_{cp}]$	$[\nu_{cp}]$	$[f_{agg}]$	$[\phi]$	$[\theta]$
L	−1	−1	−1	0	−1	0	0	0	0
M	1	1	1	0	1	0	0	0	0
T	−2	2	−2	0	−2	0	0	0	0

(D.3)

and for (D.2) as

	$[\sigma_{ITZ,I}]$	$[\mathbf{\Sigma}]$	$[E_{agg}]$	$[\nu_{agg}]$	$[E_{cp}]$	$[\nu_{cp}]$	$[E_{ITZ}]$	$[\nu_{ITZ}]$	$[f_{agg}]$	$[\phi]$	$[\theta]$
L	−1	−1	−1	0	−1	0	−1	0	0	0	0
M	1	1	1	0	1	0	1	0	0	0	0
T	−2	2	−2	0	−2	0	−2	0	0	0	0

(D.4)

where $\mathbf{\Sigma}$ stands for the full stress tensor, i.e. for six independent components. L, M, and T are the base dimensions of length, mass, and time, respectively [10], i.e. they are abstract positive numbers related to any changes of units of measurements chosen to observe the physical problem. The amount n of governing properties ($n = 13$ for aggregate stresses and $n = 15$ for ITZ stresses), can subsequently be reduced by k, which is equal to the rank of the exponent matrix of dimension, $k = 1$ for both matrices, see (D.3) and (D.4), respectively. This way, we arrive at $n - k$ dimensional dependent quantities, whereby $n - k = 12$ for aggregate stresses and $n - k = 14$ for ITZ stresses. The functions ψ_{agg} and ψ_{ITZ} can now be rewritten in dimensionless form, denoted as Ψ_{agg} and Ψ_{ITZ}, whereby E_{cp} was chosen in order to make the other dimensional quantities dimensionless:

$$\frac{T_r}{E_{cp}} = \Psi_{agg}\left(\frac{\mathbf{\Sigma}}{E_{cp}}, \frac{E_{agg}}{E_{cp}}, \nu_{agg}, \frac{E_{cp}}{E_{cp}}, \nu_{cp}, f_{agg}, \phi, \theta\right) , \tag{D.5}$$

$$\frac{\sigma_{ITZ,I}}{E_{cp}} = \Psi_{ITZ}\left(\frac{\mathbf{\Sigma}}{E_{cp}}, \frac{E_{agg}}{E_{cp}}, \nu_{agg}, \nu_{cp}, \frac{E_{ITZ}}{E_{cp}}, \nu_{ITZ}, f_{agg}, \phi, \theta\right) . \tag{D.6}$$

Dimensional analysis allowed for reducing the number of influencing parameters by one. A more significant reduction is not possible, since the governing quantities are either dimensionless, such as the Poisson's ratios, the volume fraction, and the position angles, or they exhibit the same dimension, such as the stress or traction components and the elastic moduli.

Appendix E

Model implementation into the Maple environment

Herein, we provide commented *Maple* sheets (lines starting with "#" are comments). At first, some functions are briefly described (see Sec. E.1), involving some which are provided by a package for tensor calculations. Next, the input properties are initialized and the homogenized stiffness of concrete is computed, see Sec. E.1. The subsections "phase properties" and "derivation of homogenized stiffness", given in this section, are prerequisite for the following calculations. This is followed by the implementation of the debonding criterion (4.1), which is solved for the three positions on an aggregate sphere, where the maximum radial traction component may possibly be observed under a macroscopic principal loading state, see Sec. E.2. In this context, we compute the equations of the three planes of the elastic limit surface in macroscopic principal stress space, see also Fig. E.1, and we calculate the intersection of this elastic limit surface with the biaxial planes. As for ITZ failure (see Sec. E.3), we compute the stress concentration from macrostresses to ITZ microstresses, see also Fig. E.2 for a three-dimensional illustration of the radial ITZ stress component, which is equal to the radial traction component at the aggregate's surface. Next, we perform a principal stress analysis and consider the ITZ failure criterion (4.2), which is solved for uniaxial, biaxial, and triaxial macroscopic stresses, respectively. The numerical procedure for the calculation of the biaxial elastic limit envelope, see also Fig. E.3, as well as for the elastic limit surface under multiaxial loading, which is determined in deviatoric planes as well as a in meridional sections, is also included.

E.1 Code: input and homogenization

```
> restart;
> # load libraries and routines
> new_lib_dir := "/home/mk/library/": libname := new_lib_dir, libname:
> with(tens3d):with(linalg):with(bproutines):with(plots):with(plottools):with(
    LinearAlgebra):
```

```
# FUNCTIONS AND OPERATORS
> # "isoelstiff(E,nu,1)" creates 4th-order stiffness tensor with E as Young's
    modulus and nu as Poisson's ratio
> # "eshisosph(nu)" creates the 4th-order Eshelby tensor for a spherical
    inclusion embedded in infinite isotropic matrix with Poisson's ratio nu
> # "Inv4(T)" inverts the 4th-order tensor T
> # "Iso4(1)" creates the 4th-order unity tensor
> # "&++", "&--" tensor addition and subtraction for tensors of equal order
> # "&**" Multiplication of tensor with scalar
> # "&t2" double-contraction of tensors
> # "vct4(T)" illustration of 4th-order tensor T in compressed matrix notation
> # "vxt4(M)" creates a 4-th order tensor of the matrix M according to
    compressed notation
> # "compt4(T,i,j,k,l)" extracts the ijkl-component of a 4th-order tensor T
> # "def_tenseur(M,[cont,cont],base_fond)" creates the 2nd-order tensor for the
    matrix M, whereby M contains contravariant components
> # "composantes(T2,[cont,cont],base_fond)" gives the contravariant components
    of the 2nd-order tensor T2
> # "def_tenseur(v,[cont],base_fond)" creates the 1st-order tensor for the
    vector v, whereby v is given in contravariant components

# PHASE PROPERTIES
> # all phases are isotropic

> # inclusion phase (AGGREGATES)
> E_i:=2: #input, Young's modulus of inclusion
> nu_i:=0.25: #input, Poisson's ratio of inclusion
> f_i:=0.7: #input, volume fraction of inclusion phase
>
> # matrix phase (CEMENT PASTE)
> E_m:=1: #input, Young's modulus of matrix
> nu_m:=0.25: #input, Poisson's ratio of matrix
> f_m:=1-f_i: #volume fraction of matrix
>
> # interfacial transition zone, ITZ (2D during homogenization, afterwards 3D)
> E_itz:=0.5*E_m: #input, Young's modulus of ITZ
> nu_itz:=nu_m: #input, Poisson's ratio of inclusion

# DERIVATION OF HOMOGENIZED STIFFNESS
> # spherical inclusions embedded in infinite Matrix
> # --> Eshelby problem (perfect bonding, 2D-interface)

> # phase stiffness tensors
> interface(warnlevel=0):
> C_i := isoelstiff(E_i,nu_i,1):
```

```
> C_itz:=isoelstiff(E_itz,nu_itz,1):
> C_m:=isoelstiff(E_m,nu_m,1):

> # hill tensor of inclusion
> S_sph := eshisosph(nu_m): # Eshelby tensor of sphere in cement paste
> P_sph := S_sph &t2 (Inv4(C_m)): # corresponding Hill tensor
> interface(warnlevel=4):

> # homogenization
> # according to Mori–Tanaka scheme (cement paste is identified as matrix phase)
>
> # infinite strain concentration tensor for matrix
> A_m_inf := Iso4(1):
> # infinite strain concentration tensor for inclusion
> A_i_inf := Inv4((Iso4(1) &++ (P_sph &t2 (C_i &— C_m)))):
>
> # link between macrostrains and auxiliary strains at the infinite boundary
> link_E_Einf_con:=Inv4(((1-f_i) &** A_m_inf) &++ (f_i &** A_i_inf)):
>
> A_m := A_m_inf &t2 link_E_Einf_con: # strain concentration tensor for matrix
> A_i := A_i_inf &t2 link_E_Einf_con: # strain concentration tensor for
    inclusion
>
> sb1 := vct4((f_i &** A_i) &++ ((1-f_i) &** A_m)): # check, should be identity
>
> # homogenized stiffness for 2–phase composite
> C_hom := (f_i &** (C_i &t2 A_i)) &++ ((1-f_i) &** (C_m &t2 A_m)):
> C_homc:=vct4(C_hom): # matrix representation of homogenized stiffness
>
> # C_hom is isotropic, therefore, homogenized Young's modulus
> # and homogenized Poisson's ratio can be given:
> E_hom := (compt4(C_hom,1,2,1,2)*(3*compt4(C_hom,1,1,1,1)-4*compt4(C_hom
    ,1,2,1,2)))/(compt4(C_hom,1,1,1,1)-compt4(C_hom,1,2,1,2)):
> nu_hom := (compt4(C_hom,1,1,1,1)-2*compt4(C_hom,1,2,1,2))/(2*(compt4(C_hom
    ,1,1,1,1)-compt4(C_hom,1,2,1,2))):
#
```

E.2 Code: debonding

```
# STRESS STATE AT THE AGGREGATE SURFACE
> # macrostresses and macrostrains
> Sigmac := array(1..3,1..3,[[S11,S12,S13],[S12,S22,S23],[S13,S23,S33]]): #
    Introduction of macrostress in Cartesian coordinates
> Sigma := def_tenseur(Sigmac,[cont,cont],base_fond): # macroscopic stress
    tensor
```

```
>
> Epsilon := Inv4(C_hom) &t2 Sigma: # macroscopic strain tensor (Hooke's law):

> # scale transition
> # average microscopic phase strain tensors
> epsilon_m := A_m &t2 Epsilon:
> epsilon_i := A_i &t2 Epsilon:
>
> # average microscopic phase stress tensors
> sigma_m := C_m &t2 epsilon_m:
> sigma_i := C_i &t2 epsilon_i:
> sigma_ic := composantes(sigma_i,[cont,cont],base_fond): # matrix
    representation

> # the maximum radial stress is located at the pole, or at the equator where
    phi=0 or phi=pi/2
> # at these points the radial component in the spherical coordinate system is
    equal to one Cartesian component
> si_i_pol:=subs(phi=0,theta=0,sigma_ic(3,3)):
> si_i_eq0:=subs(phi=Pi/2,theta=0,sigma_ic(1,1)):
> si_i_eq90:=subs(phi=Pi/2,theta=Pi/2,sigma_ic(2,2)):

# ELASTIC LIMIT SURFACE
> with(geom3d):
> # 3 planes, describing the elastic limit
> # to obtain these planes, the respective radial stress components are set
    equal to the tensile strength of the bond ftbond,
> # but since we give the elastic limit in terms of these strength, we set the
    stresses equal to 1
>     plane(E1,si_i_pol=1,[S11,S22,S33]):
>     plane(E2,si_i_eq0=1,[S11,S22,S33]):
>     plane(E3,si_i_eq90=1,[S11,S22,S33]):
> # tip of the tetrahedron
>     intersection (P, E1, E2, E3):
>     Stipdeb:=coordinates (P, [x, y, z])[1];
> # intersection of one blue plane (pole debonding) with pi1-plane
>     plane(P1,S33=0,[S11,S22,S33]):
>     intersection (tra1, E1, P1):
>     Equation (tra1, u, [S11, S22, S33]):
> # intersection of this trace line with x-axis
>     line(xaxis,[point(orig,0,0,0),point(xx,5,0,0)]):
>     intersection(Smin,tra1,xaxis):
>     Smindeb:=coordinates(Smin)[1]; #uniaxial compressive limit
> # intersection of red plane (debonding at phi=Pi/2, theta=Pi/2) with pi1-plane
>     line(yaxis,[orig,point(xx,0,5,0)]):
```

```
>      intersection (tra2, E3, P1):
>      Equation (tra2, u, [S11, S22, S33]):
># intersection of this trace line with y-axis
>      intersection(Smax,tra2,yaxis):
>      Smaxdeb:=coordinates(Smax)[2]; #uniaxial tensile limit
># intersection of E1 and E2 delivers the edge of the tetrahedron
>      intersection (e, E1, E2):
>      Equation (e, v, [S11, S22, S33]);
># illustration of the elastic limit
> draw([E1(color=cyan),E2(color=green),E3(color=red),tra1(color=black),e(color=
    black)],axes=boxed,labels=[S11,S22,S33],view=[-20..2,-20..2,-20..2]);
#
```

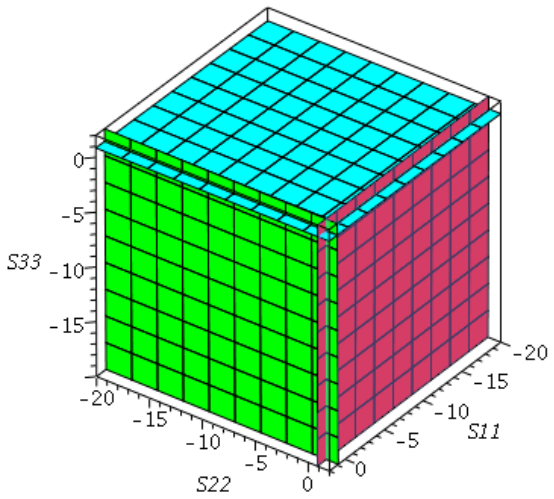

Figure E.1: Three planes describing the elastic limit envelope for debonding in principal stress space

E.3 Code: ITZ failure

E.3.1 ITZ stresses

```
# TRANSFORMATION MATRIX
># base vectors of the moving spherical coordinate system
> rx:=cos(theta)*sin(phi): ry:=sin(theta)*sin(phi): rz:=cos(phi):
> tx:=-sin(theta): ty:=cos(theta): tz:=0:
> px:=cos(theta)*cos(phi): py:=sin(theta)*cos(phi): pz:=-sin(phi):
>
> r := def_tenseur([rx, ry, rz],[cont],base_fond):
> t := def_tenseur([tx, ty, tz],[cont],base_fond):
```

```
> p := def_tenseur([px, py, pz],[cont],base_fond):

> # base vectors of the Cartesian coordinate system
> e1 := def_tenseur([1, 0, 0],[cont],base_fond):
> e2 := def_tenseur([0, 1, 0],[cont],base_fond):
> e3 := def_tenseur([0, 0, 1],[cont],base_fond):

> # transformation matrix between spherical and Cartesian coordinates
> Qc := array(1..3,1..3,[[px,py,pz],[tx,ty,tz],[rx,ry,rz]]):
> Q := def_tenseur(Qc,[cont,cont],base_fond): # tensor representation of
    transformation matrix
>
> QTc := transpose(Qc): # inverse of Q, which exhibits orthogonality
> QT := def_tenseur(QTc,[cont,cont],base_fond): # tensor representation of Qtc

# STRESSES IN AGGREGATES
> # macrostress and macrostrain
> # Introduction of macrostress in Cartesian coordinates
> Sigmac := array(1..3,1..3,[[S11,S12,S13],[S12,S22,S23],[S13,S23,S33]]):
> Sigma := def_tenseur(Sigmac,[cont,cont],base_fond): # macroscopic stress
    tensor
>
> Epsilon := Inv4(C_hom) &t2 Sigma: # macroscopic strain tensor (Hooke's law):

> # scale transition
> # average microscopic phase strain tensors
> epsilon_m := A_m &t2 Epsilon:
> epsilon_i := A_i &t2 Epsilon:
>
> # average microscopic phase stress tensors
> sigma_m := C_m &t2 epsilon_m:
> sigma_i := C_i &t2 epsilon_i:

> # transformation to spherical coordinates
> sigma_ilokal := Q &t1 sigma_i &t1 QT:
> sigma_ilokc := composantes(sigma_ilokal,[cont,cont],base_fond): #
    microstresses in spherical coordinates
> epsilon_ilokal := Q &t1 epsilon_i &t1 QT:
> epsilon_ilokc := composantes(epsilon_ilokal,[cont,cont],base_fond): #
    microstrains in spherical coordinates

# STRESSES IN INTERFACES
> # Equilibrium at the interface implies:
> sigma_itz_lok_phir := compt2(sigma_ilokal,1,3):
> sigma_itz_lok_thetar := compt2(sigma_ilokal,2,3):
```

```
> sigma_itz_lok_rr := compt2(sigma_ilokal,3,3):

> # Compatibility at the interface implies:
> eps_itz_lok_phiphi := compt2(epsilon_ilokal,1,1):
> eps_itz_lok_phitheta := compt2(epsilon_ilokal,1,2):
> eps_itz_lok_thetatheta := compt2(epsilon_ilokal,2,2):

> # Introduction of strain tensor at the interface and calculation of interface
    stress tensor
> eps_itz_lokc := array(1..3,1..3,[[eps_itz_lok_phiphi,eps_itz_lok_phitheta,
    eps_itz_lok_phir],[eps_itz_lok_phitheta,eps_itz_lok_thetatheta,
    eps_itz_lok_thetar],[eps_itz_lok_phir,eps_itz_lok_thetar,eps_itz_lok_rr]]):
> eps_itz_lok := def_tenseur(eps_itz_lokc,[cont,cont],base_fond):
>
> sigma_itz_lok := C_itz &t2 eps_itz_lok:

> # solving for the 6 unknown components of the interfacial stress and strain
    tensors
> eq1 := sigma_itz_lok_phiphi = compt2(sigma_itz_lok,1,1):
> eq2 := sigma_itz_lok_phitheta = compt2(sigma_itz_lok,1,2):
> eq3 := sigma_itz_lok_phir = compt2(sigma_itz_lok,1,3):
> eq4 := sigma_itz_lok_thetatheta = compt2(sigma_itz_lok,2,2):
> eq5 := sigma_itz_lok_thetar = compt2(sigma_itz_lok,2,3):
> eq6 := sigma_itz_lok_rr = compt2(sigma_itz_lok,3,3):
>
> assign(solve({eq1,eq2,eq3,eq4,eq5,eq6},{sigma_itz_lok_phiphi,
    sigma_itz_lok_thetatheta,sigma_itz_lok_phitheta,eps_itz_lok_rr,
    eps_itz_lok_phir,eps_itz_lok_thetar}));

> # Insertion of the derived components into the tensors
> sigma_itz_lokc := array(1..3,1..3,[[sigma_itz_lok_phiphi,
    sigma_itz_lok_phitheta, sigma_itz_lok_phir],[sigma_itz_lok_phitheta,
    sigma_itz_lok_thetatheta, sigma_itz_lok_thetar],[sigma_itz_lok_phir,
    sigma_itz_lok_thetar, sigma_itz_lok_rr]]):
> sigma_itz_lok := def_tenseur(sigma_itz_lokc,[cont,cont],base_fond):
> sigma_itz_lokc := composantes(sigma_itz_lok,[cont,cont],base_fond):
>
> eps_itz_lokc := array(1..3,1..3,[[eps_itz_lok_phiphi, eps_itz_lok_phitheta,
    eps_itz_lok_phir],[eps_itz_lok_phitheta, eps_itz_lok_thetatheta,
    eps_itz_lok_thetar],[eps_itz_lok_phir, eps_itz_lok_thetar, eps_itz_lok_rr]]):
> eps_itz_lok := def_tenseur(eps_itz_lokc,[cont,cont],base_fond):
> eps_itz_lokc := composantes(eps_itz_lok,[cont,cont],base_fond):

> # verification of the code with Hooke's law in the interface
```

```
> sbz := simplify(composantes(sigma_itz_lok &— (C_itz &t2 eps_itz_lok),[cont,
    cont],base_fond)):

# ILLUSTRATION OF STRESSES AND STRAINS
> # definition of macroscopic loading
> para := S11=0,S12=0,S13=0,S22=-0.4,S23=0,S33=1:

> # insertion of macroloading into interfacial stress tensor
> sigma_par_phiphi := (simplify(subs(para,sigma_itz_lok_phiphi)));
> sigma_par_thetatheta := simplify(subs(para,sigma_itz_lok_thetatheta));
> sigma_par_rr := simplify(subs(para,sigma_itz_lok_rr));
> sigma_par_phitheta := simplify(subs(para,sigma_itz_lok_phitheta));
> sigma_par_phir := simplify(subs(para,sigma_itz_lok_phir));
> sigma_par_thetar := simplify(subs(para,sigma_itz_lok_thetar));
> interface(displayprecision=4):

> # insertion of macroloading into interfacial strain tensor
> eps_par_phiphi := simplify(subs(para,eps_itz_lok_phiphi))*E_itz;
> eps_par_thetatheta := simplify(subs(para,eps_itz_lok_thetatheta))*E_itz;
> eps_par_rr := simplify(subs(para,eps_itz_lok_rr))*E_itz;
> eps_par_phitheta := simplify(subs(para,eps_itz_lok_phitheta))*E_itz;
> eps_par_phir := simplify(subs(para,eps_itz_lok_phir))*E_itz;
> eps_par_thetar := simplify(subs(para,eps_itz_lok_thetar))*E_itz;

> # insertion of macroloading into principal interfacial stresses
> sigma_h:=solve(evalf(subs(para,-sh^3+I1*sh^2-I2*sh+I3)=0),sh):
> s1par:=sigma_h[1]: s2par:=sigma_h[2]: s3par:=sigma_h[3]:

> # 3D illustration of one component
>
> obj1:= plot3d (3+Re(sigma_par_rr),theta = 0..Pi/2,phi = 0..Pi,coords=spherical
    ,color=red,thickness=1):
> K := sphere ([0,0,0], 3,color=grey,thickness=0,transparency=0.8):
> lx := line([0,0,0],[5,0,0],color=black, thickness=2,style=line):
> ly := line([0,0,0],[0,5,0],color=black, thickness=2,style=line):
> lz := line([0,0,0],[0,0,5],color=black, thickness=2,style=line):
> display ([obj1, K, lx, ly, lz],labels=['x','y','z'],axes=normal,orientation
    =[20,50],scaling=constrained):
#
```

E.3.2 Elastic limit surfaces

```
> # Invariants of the interfacial stress tensor
> # according to [Mang and Hofstetter,2000]:
> I1:=Trace(sigma_itz_lokc):
```

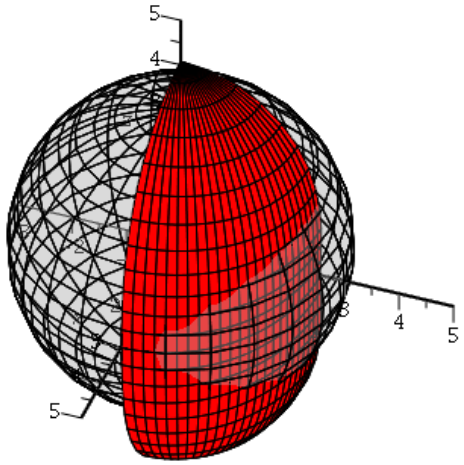

Figure E.2: Three dimensional illustration of radial stresses at the surface of the aggregate, under biaxial loading and reference material parameters

```
> I2:=Determinant(Matrix([[sigma_itz_lokc(2,2),sigma_itz_lokc(2,3)],[
    sigma_itz_lokc(3,2),sigma_itz_lokc(3,3)]]))+
> Determinant(Matrix([[sigma_itz_lokc(1,1),sigma_itz_lokc(1,3)],[sigma_itz_lokc
    (3,1),sigma_itz_lokc(3,3)]]))+
> Determinant(Matrix([[sigma_itz_lokc(1,1),sigma_itz_lokc(1,2)],[sigma_itz_lokc
    (2,1),sigma_itz_lokc(2,2)]])):
> I3:=Determinant(sigma_itz_lokc):

> # solving the characteristic equation
> # sigma_h:=solve(evalf(-sh^3+I1*sh^2-I2*sh+I3=0),sh):
> # note that a solution without specification of macrostresses is not recommend
>
> # 1st, 2nd, and third principal interfacial stress
> s1:=sigma_h[1]:s2:=sigma_h[2]:s3:=sigma_h[3]:

> ########################
> # UNIAXIAL LOADING #
> ########################
> para := S11=0,S12=0,S13=0,S22=0,S23=0,S33=1,theta=0:
> # rotational symmetry implies independence of azimuth angle

> # principal stresses and principal direction according to the well-known
    expression for plane stress state
> # valid since the shear stresses in theta-direction are vanishing (stress
    component in theta-direction = principal stress)
```

```
>
># principal stresses
> s1 := (sigma_itz_lok_rr+sigma_itz_lok_phiphi)/2 + sqrt(((sigma_itz_lok_rr-
    sigma_itz_lok_phiphi)/2)^2 + sigma_itz_lok_phir^2):
> s2 := (sigma_itz_lok_rr+sigma_itz_lok_phiphi)/2 - sqrt(((sigma_itz_lok_rr-
    sigma_itz_lok_phiphi)/2)^2 + sigma_itz_lok_phir^2):
> s3 := sigma_itz_lok_thetatheta:
>
># plot
> ph1:=plot(subs(para,s1),phi=0..Pi,color=black,linestyle=solid,thickness=1):
> ph2:=plot(subs(para,s2),phi=0..Pi,color=blue,linestyle=solid,thickness=1):
> ph3:=plot(subs(para,s3),phi=0..Pi,color=red,linestyle=solid,thickness=1):
> display([ph1,ph2,ph3]):

># principal direction
># alpha_haupt denotes the angle between the axis of the spherical coordinate
    system where the largest component occurs and the largest principal stress
> alpha_haupt:=arctan((2*sigma_itz_lok_phir)/(sigma_itz_lok_rr-
    sigma_itz_lok_phiphi))/2:
>
># plot
> plotalpha1:=plot((evalf(subs(para,(alpha_haupt))*180/Pi)),phi=0..Pi):
> plotalpha2:=plot((evalf(subs(para,alpha_haupt+phi)*180/Pi)),phi=0..Pi):
> display(array([plotalpha1,plotalpha2])):

># a) macroscopic uniaxial compression (S33<0)
># => maximum tensile stress is given by s2
>
># point at the interface (expressed through zenith angle) where the maximum of
    s2 occurs (first derivative = 0)
> phimax := fsolve(diff(subs(para,s2),phi)=0,phi=0.2..1.5):
>
># insertion of phimax into the function of s2 delivers the sought extreme
> maxs2 := eval(subs(phi=phimax,para,s2))*S:
>
># insertion of phimax into the function of alpha_haupt delivers the
    corresponding principal base frame
> alphamaxs := eval(subs(phi=phimax,para,alpha_haupt)):
>
># check of symmetry in bottom hemisphere
> phimax := fsolve(diff(subs(para,s2),phi)=0,phi=1.6..3.1):
> maxs2 := eval(subs(phi=phimax,para,s2))*S:

># macroloading corresponding to the onset of microcracks within ITZ (mode 1)
># obtained if maxs2 is equal to the interfacial tensile strength ftITZ
```

```
> Sc_mode1 := solve(maxs2=ftITZ,S):

> # comparison: macroloading corresponding to debonding (mode 2)
> # obtained if the radial aggregate stress component at the equator (phi=Pi/2)
    is equal to the bond's tensile strength
> Sc_mode2 := 1/evalf(subs(phi=Pi/2,para,sigma_ilokc(3,3)))*ftbond:

> # b) macroscopic uniaxial tension (S33>0)
> # => maximum tensile stress is given by s1
>
> # by analogy to uniaxial compression
> phimin := fsolve(diff(subs(para,s1),phi)=0,phi=0.1..1.5):
> mins1 := eval(subs(phi=phimin,para,s1))*S:
> alphamins := eval(subs(phi=phimin,para,alpha_haupt)):
>
> # check of symmetry in bottom hemisphere
> phimin := fsolve(diff(subs(para,s1),phi)=0,phi=1.6..3.1):
> mins1 := eval(subs(phi=phimin,para,s1))*S:

> # macroloading corresponding to the onset of microcracks within ITZ (mode 1)
> # obtained if mins1 is equal to the interfacial tensile strength ftITZ
> St_mode1 := solve(ftITZ = mins1,S):

> # comparison: macroloading corresponding to debonding (mode 2)
> # obtained if the radial aggregate stress component at the pole (phi=0) is
    equal to the bond's tensile strength
> St_mode2 := 1/evalf(subs(phi=0,para,sigma_ilokc(3,3)))*ftbond:

> ######################
> # BIAXIAL LOADING #
> ######################
> # STRATEGY
> # we consider biaxial loading in the S11-S22 plane
> # the macroscopic stress path is given by the S11=1 and S22=alphavor (e.g.
    alphavor=1...symmetric biaxial loading)
> # hence we calculate the elastic limit of one half within the biaxial stress
    space, the other half is derived by flipping around the first median (blue
    points in the illustration)
> parb := S11=1,S12=0,S13=0,S22=alphavor,S23=0,S33=0:

> # CALCULATION OF ELASTIC LIMIT ENVELOPE
> # 3 loops are used, 2 for different points at the interface (expressed by
    zenith angle, azimuth angle)
> # and one loop for the different ratios of S11 to S22 (expressed by alphavor)
```

```
> step_angle:=13: # amount of computation steps for loop over phi and theta,
   respectively
> step_alpha:=6: # amount of computation steps for values of alphavor
>
> # initialization of maximum principal stresses and corresponding directions
> maxs:=[seq(0(n),n=1..step_alpha)]:mins:=[seq(0(n),n=1..step_alpha)]:
> minsminus:=[seq(0(n),n=1..step_alpha)]:maxsminus:=[seq(0(n),n=1..step_alpha)]:
> thetamax:=[seq(0(n),n=1..step_alpha)]:phimax:=[seq(0(n),n=1..step_alpha)]:
> thetamin:=[seq(0(n),n=1..step_alpha)]:phimin:=[seq(0(n),n=1..step_alpha)]:
> thetamaxminus:=[seq(0(n),n=1..step_alpha)]:phimaxminus:=[seq(0(n),n=1..
   step_alpha)]:
> thetaminminus:=[seq(0(n),n=1..step_alpha)]:phiminminus:=[seq(0(n),n=1..
   step_alpha)]:
>
> for alphait from 1 to step_alpha do
>    al:=(alphait-1)/(step_alpha-1); # loop over different ratios S11/S22
>    for thetait from 1 to step_angle do
>       mytheta:=(thetait-1)/(step_angle-1)*Pi/2; # loop over latitudinal points
>       for phiit from 1 to step_angle do
>          myphi:=(phiit-1)/(step_angle-1)*Pi/2; # loop over longitudinal points
>
>          # principal stresses from invariants
>          # for positive and negative values of alphavor
>          sigma_h:=solve(evalf(subs(parb,phi=myphi,theta=mytheta,alphavor=al,
>                   -sh^3+I1*sh^2-I2*sh+I3)=0),sh);
>          sigma_hminus:=solve(evalf(subs(parb,phi=myphi,theta=mytheta,
>                        alphavor=-al,-sh^3+I1*sh^2-I2*sh+I3)=0),sh);
>
>          # reading out the minimum and maximum ITZ principal stresses for
>          # positive and negative values of alphavor:
>          min_sigma_h:=min(seq(Re(sigma_h[k]),k=1..3));
>          max_sigma_h:=max(seq(Re(sigma_h[k]),k=1..3));
>
>          min_sigma_hminus:=min(seq(Re(sigma_hminus[k]),k=1..3));
>          max_sigma_hminus:=max(seq(Re(sigma_hminus[k]),k=1..3));
>
>          # if the studied interfacial point delivers an extreme of one
>          # principal stress, this extreme and the point (phi,theta) is
>          # recorded:
>          if max_sigma_h>maxs[alphait] then
>               maxs[alphait]:=max_sigma_h;
>               phimax[alphait]:=myphi;
>               thetamax[alphait]:=mytheta;
>          end if;
>          if min_sigma_h<mins[alphait] then
```

```
>                 mins[alphait]:=min_sigma_h;
>                 phimin[alphait]:=myphi;
>                 thetamin[alphait]:=mytheta;
>             end if;
>             if min_sigma_hminus<minsminus[alphait] then
>                 minsminus[alphait]:=min_sigma_hminus;
>                 phiminminus[alphait]:=myphi;
>                 thetaminminus[alphait]:=mytheta;
>             end if;
>             if max_sigma_hminus>maxsminus[alphait] then
>                 maxsminus[alphait]:=max_sigma_hminus;
>                 phimaxminus[alphait]:=myphi;
>                 thetamaxminus[alphait]:=mytheta;
>             end if;
>
>         end do;
>     end do;
> end do:

> # PLOT
> # Initialization
> Sigmamax_xx:=[seq(0(n),n=1..step_alpha)]:
> Sigmamax_yy:=[seq(0(n),n=1..step_alpha)]:
> Sigmamin_xx:=[seq(0(n),n=1..step_alpha)]:
> Sigmamin_yy:=[seq(0(n),n=1..step_alpha)]:
> Sigmaminminus_xx:=[seq(0(n),n=1..step_alpha)]:
> Sigmaminminus_yy:=[seq(0(n),n=1..step_alpha)]:
> Sigmamaxminus_xx:=[seq(0(n),n=1..step_alpha)]:
> Sigmamaxminus_yy:=[seq(0(n),n=1..step_alpha)]:
> Sigma_zz:=[seq(0(n),n=1..step_alpha)]: # since biaxial, always zero
>
> for alphait from 1 to step_alpha do
>     al:=(alphait-1)/(step_alpha-1); # similar loop as before
>
>     # elastic limit is reached if the largest principal stress
>     # is equal to the tensile strength of the ITZ
>     # in terms of the load-increasing-coefficient, maxs*lambda=ftITZ,
>     # which means that in dimensionless diagramm, plot 1/maxs
>
>     # compression-compression
>     # mins (or the largest absolute value of the (negative) principal
>     # compressive stress for alphavor>0) implies a lambda of  1/mins
>     # and al/mins, respectively, which is both negative
>     Sigmamin_xx[alphait] := 1/mins[alphait]:
>     Sigmamin_yy[alphait] := al/mins[alphait];
```

```
>
>    # tension-tension
>    # maxs (or the largest positive principal tensile stress for alphavor>0)
>    # corresponds to a elastic limit of 1/maxs and al/maxs
>    Sigmamax_xx[alphait] := 1/maxs[alphait];
>    Sigmamax_yy[alphait] := al/maxs[alphait];
>
>    # compression-tension
>    # minsminus (or the largest absolute value of the (negative) principal
>    # compressive stress for alphavor<0) implies a lambda of  1/minsminus and
>    # al/minsminus, respectively, whereby the latter is set negative
>    # because al is by definition at the beginning of the loop positive
>    Sigmaminminus_xx[alphait] := 1/minsminus[alphait];
>    Sigmaminminus_yy[alphait] := -al/minsminus[alphait];
>
>    # tension-compression (alphavor<0)
>    # maxminus (or the largest absolute value of the principal tensile stress
>    # for alphavor<0) implies a lambda of  1/minsminus and al/minsminus,
>    # respectively, whereby the latter is set negative
>    # because al is by definition at the beginning of the loop positive
>    Sigmamaxminus_xx[alphait] := 1/maxsminus[alphait];
>    Sigmamaxminus_yy[alphait] := -al/maxsminus[alphait];
>
> end do:
>
> pbi1:=pointplot(Sigmamin_xx,Sigmamin_yy,color=black):
> pbi2:=pointplot(Sigmamin_yy,Sigmamin_xx,color=blue): # flipped
>
> pbi3:=pointplot(Sigmamax_xx,Sigmamax_yy,color=green):
> pbi4:=pointplot(Sigmamax_yy,Sigmamax_xx,color=blue): # flipped
>
>
> pbi5:=pointplot(Sigmaminminus_xx,Sigmaminminus_yy,color=red):
> pbi6:=pointplot(Sigmaminminus_yy,Sigmaminminus_xx,color=blue): # flipped
>
> pbi7:=pointplot(Sigmamaxminus_xx,Sigmamaxminus_yy,color=magenta):
> pbi8:=pointplot(Sigmamaxminus_yy,Sigmamaxminus_xx,color=blue): # flipped
>
> display([pbi1,pbi2,pbi3,pbi4,pbi5,pbi6,pbi7,pbi8],view=[-6..2,-6..2],labels=['
   S1/ftITZ','S2/ftITZ']):

> ########################
> # MULTIAXIAL LOADING #
> ########################
> # a) tip of elastic limit surface (S11=S22=S33)
```

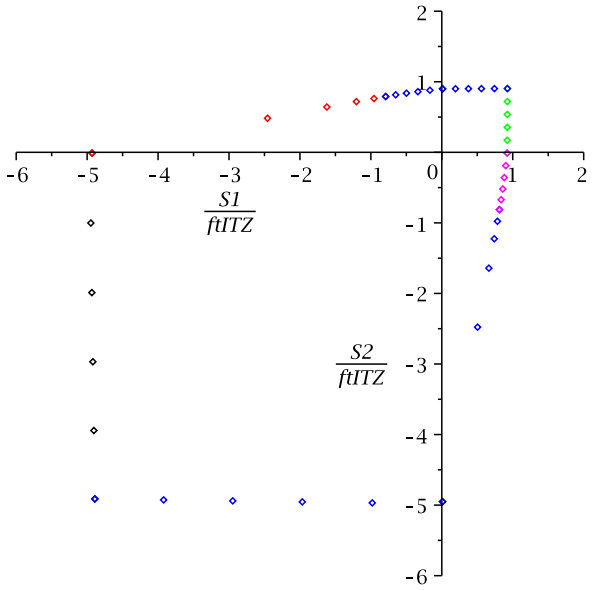

Figure E.3: Biaxial elastic limit envelope, specifying the loading path allows for calculation of the half envelope, which is subsequently mirrored with respect to the first median

```
>
> parr1 := S11=1,S12=0,S13=0,S22=1,S23=0,S33=1,phi=0,theta=0:
> # since the obtained microstresses are homogeneous,
> # the results are independent of the position at the interface
>
> # principal stresses obtained from the solution of the characteristic equation
> sigma_tri:=(evalf(solve(-sh^3+subs(parr1,I1)*sh^2-subs(parr1,I2)*sh+subs(parr1
    ,I3)=0,sh))):
> # maximum of the three principal stresses
> max_sigma_tri:=(seq(Re(sigma_tri[k]),k=1..3)):
>
> # related coordinates (S11=S22=S33=Sh_tri) in macroscopic principal stress
    space
> Sh_tri:=1/max(max_sigma_tri);

> # b) deviatoric planes
>
> steplode:=7: # steps for loop over different lode angles (0<myThe<Pi/3)
> stepmeridian:=9: # steps along the hydrostatic axis
> step_angle:=5: # steps defining the amount of studied positions at the
    interface
>
> # initialization
> S1xi:=[seq(0[k],k=1..steplode)]:
> S2xi:=[seq(0[k],k=1..steplode)]:
```

```
> S3xi:=[seq(0[k],k=1..steplode)]:
> lodexi:=[seq(0[k],k=1..steplode)]:
> rhoxi:=[seq(0[k],k=1..steplode)]:
> xixi:=[seq(0[k],k=1..steplode)]:
> phirel_xi:=[seq(0[k],k=1..steplode)]:
> thetarel_xi:=[seq(0[k],k=1..steplode)]:
>
># general relation between the Haigh–Westergaard coordinates
># and the macroscopic principal stresses
> S1:=1/sqrt(3)*xic+sqrt(2/3)*rhoc*cos(Thc):
> S2:=1/sqrt(3)*xic+sqrt(2/3)*rhoc*cos(Thc-2*Pi/3):
> S3:=1/sqrt(3)*xic+sqrt(2/3)*rhoc*cos(Thc+2*Pi/3):
>
> maxtryendmin:=0.1: # start value of deviatoric component
>
> for meridianit from 1 to stepmeridian do
># loop for different position of the deviotoric plane, expressed by the
># hydrostatic stress componen myxic<Sh_tri*sqrt3
>     myxic:=evalf(Sh_tri*sqrt(3)*9/10-(meridianit-1)^2*sqrt(3)/10*Sh_tri);
>
>     #myxic:=-5;
>     #meridianit:=52;
>     mm:=0:
>
>     for lodeit from 1 to steplode do
>     # loop for different angles within the deviatoric plane,
>     # expressed by the Lode angle myThc
>         myThc:=evalf((0+(lodeit-1)/(steplode-1)*60)*Pi/180);
>         whilej:=0:
>         maxtry:=0:
>         while maxtry<1 do
>            # computation as long as the maximum principal stress is smaller
>            # than the interfacial tensile strength i.e. as long as maxtry<1
>            # we increase the third coordinate (rho=m) till
>            # we reach the elastic limit
>             whilej:=whilej+1;
>
>            # Initialization of the starting values for m
>             if whilej<1.5 then
>                 if lodeit=1 then m:=maxtryendmin; end if;
>                # the starting value of m=rho is equal to maxtryendmin
>                # (i.e. maxtry for lode=0 from the last deviatoric plane)
>                 if lodeit=2 then m:=maxtryend*9/10; end if;
>                # the starting value of m=rho is a little less than maxtryend
>                # (i.e. maxtry for lode=0 from the currend deviatoric plane)
```

```
>                 if lodeit>2.5 then m:=maxtryend; end if;
>                 # the starting value of m=rho is equal to maxtryend
>                 step_angle:=25; # full amount of locations in each first run
>             end if:
>             if whilej>1.5 then
>                 # i.e. for all other runs m is set equal to the amount
>                 # where the elastic limit for the previous lode was reached
>                 m:=mm;
>
>                 step_angle:=5+round(maxtry^5*5)+round(maxtry^10*5)+
>                             round(maxtry^20*5)+round(maxtry^50*5);
>                 # amount of locations increases when nearing the elastic limit
>                 # => prerequisite for a fast computation
>             end if:
>
>             S1try:=evalf(subs(xic=myxic,rhoc=m,Thc=myThc,S1));
>             S2try:=evalf(subs(xic=myxic,rhoc=m,Thc=myThc,S2));
>             S3try:=evalf(subs(xic=myxic,rhoc=m,Thc=myThc,S3));
>
>             maxtry:=0:
>             for thetait from 1 to step_angle do
>                   mytheta:=(thetait-1)/(step_angle-1)*Pi/2;
>
>                   for phiit from 1 to step_angle do
>                       #WARNING("mm = %1",mm);
>                       myphi:=(phiit-1)/(step_angle-1)*Pi/2;
>
>                       sigma_h:=solve(evalf(subs(S12=0,S23=0,S13=0,S11=S1try,
>                                S22=S2try,S33=S3try,phi=myphi,theta=mytheta,
>                                -sh^3+I1*sh^2-I2*sh+I3)=0),sh);
>                       maxtry_sigma_h:=max(seq(Re(sigma_h[k]),k=1..3));
>
>                       if  maxtry_sigma_h>maxtry then
>                       # if we obtain a new maximum at a specific position
>                       # we memorize the maximum and the position
>                             maxtry:=maxtry_sigma_h;
>                             phirel_xi[lodeit] := evalf(myphi);
>                             thetarel_xi[lodeit] := evalf(mytheta);
>                       end if;
>                   end do;
>              end do:
>
>              WARNING("m=%1, step_angle=%2, maxtry=%3, phi/theta=%4/%5",
>              m,step_angle,maxtry,phirel_xi[lodeit],thetarel_xi[lodeit]);
>
```

```
>              mm:=m;
>              mm:=mm+0.1*(1-maxtry)+0.001;
>              # increase of rho is denoted as mm,
>              # the increase is proportional to the difference (1-maxtry)
>              # => faster computation
>
>              if meridianit=1 then
>                  if lodeit=1 then
>                      if whilej<1.5 then
>                          mm:=0.1+0.5*(1-maxtry)+0.0005;
>                      end if;
>                  end if;
>              end if; #hence in the very first run
>          end do;
>
>          S1xi[lodeit]:=S1try;
>          S2xi[lodeit]:=S2try;
>          S3xi[lodeit]:=S3try;
>          lodexi[lodeit]:=myThc;
>          rhoxi[lodeit]:=m;
>          xixi[lodeit]:=myxic;
>
>          WARNING("DONE: xic=%1, Thc=%2, rhoc=%3, theta=%4, phi=%5, maxtry=%6",
>          myxic,myThc,m,thetarel_xi[lodeit],phirel_xi[lodeit],maxtry);
>
>          maxtryend:=m:
>          # starting value of rho for next run within current deviatoric plane
>
>          if lodeit =1 then
>              maxtryendmin:=maxtryend;
>              # starting value of rho for the next deviatoric plane
>          end if:
>
>      end do;
>
>      # OUTPUT
>      file := cat(pfad,"mode",mode,_multi_haupt_,comp,"_xi",meridianit,".m"):
>      fd := fopen(file, WRITE):
>      for i from 1 to steplode do
>       fprintf(fd, "s1_multi_xi%a(%a)  = %.10f;\n",meridianit,i,S1xi[i]):
>       fprintf(fd, "s2_multi_xi%a(%a)  = %.10f;\n",meridianit,i,S2xi[i]):
>       fprintf(fd, "s3_multi_xi%a(%a)  = %.10f;\n",meridianit,i,S3xi[i]):
>       fprintf(fd, "lode_multi_xi%a(%a) = %.10f;\n",meridianit,i,lodexi[i]):
>       fprintf(fd, "rho_multi_xi%a(%a) = %.10f;\n",meridianit,i,rhoxi[i]):
>       fprintf(fd, "xi_multi_xi%a(%a) = %.10f;\n",meridianit,i,xixi[i]):
```

```
>       fprintf(fd, "phi_multi_xi%a(%a) = %.10f;\n",meridianit,i,phirel_xi[i]):
>       fprintf(fd,"theta_multi_xi%a(%a)=%.10f;\n",meridianit,i,thetarel_xi[i]):
>      od:
>      fclose(fd):
>
>      # PLOT
>            pl1:=pointplot3d(S1xi,S2xi,S3xi,color=black):
>            pl2:=pointplot3d(S2xi,S3xi,S1xi,color=grey):
>            pl3:=pointplot3d(S3xi,S1xi,S2xi,color=green):
>            pl4:=pointplot3d(S1xi,S3xi,S2xi,color=red):
>            pl5:=pointplot3d(S3xi,S2xi,S1xi,color=magenta):
>            pl6:=pointplot3d(S2xi,S1xi,S3xi,color=blue):
>      cat(plot,xitext,round(abs(myxic)*100)):=[pl1,pl2,pl3,pl4,pl5,pl6]:
> end do:

> # PLOT of deviatoric planes
> display(plot1,plot2,plot3,plot4,plot5,axes=normal,scaling=constrained,
>         view=[-15..2,-15..2,-15..2],labels=['S1/ftITZ','S2/ftITZ','S3/ftITZ'])
    :

> # c) meridians
>
> # procedure is similar to the one applied for the deviatoric planes
> stepmeridian:=9: # number of steps along the hydrostatic axes
> myThc:=0: # Lode angle expressing the meridian which is considered (myThc=0...
    tensile meridian, myThc=60...compressive meridian)
>
> step_angle:=25:
>
> # initialization
> S1lode:=[seq(0(k),k=1..stepmeridian)]:
> S2lode:=[seq(0(k),k=1..stepmeridian)]:
> S3lode:=[seq(0(k),k=1..stepmeridian)]:
> lodelode:=[seq(0[k],k=1..stepmeridian)]:
> rholode:=[seq(0[k],k=1..stepmeridian)]:
> xilode:=[seq(0[k],k=1..stepmeridian)]:
> phirel_lode:=[seq(0[k],k=1..stepmeridian)]:
> thetarel_lode:=[seq(0[k],k=1..stepmeridian)]:
>
>    maxtryend:=0.1:
>    lodeit:=1: # other if loop around different meridians
>    mm:=0:
>
>    for meridianit from 1 to stepmeridian do
>         myxic:=evalf(Sh_tri*sqrt(3)*9/10-(meridianit-1)^2*sqrt(3)/10*Sh_tri);
```

```
>
>          maxtry:=0;
>          whilej:=0:
>
>          while maxtry<1 do
>
>               whilej:=whilej+1;
>               if whilej<1.5 then m:=maxtryend; end if;
>               if whilej>1.5 then m:=mm; end if:
>
>               S1try:=evalf(subs(xic=myxic,rhoc=m,Thc=myThc,S1));
>               S2try:=evalf(subs(xic=myxic,rhoc=m,Thc=myThc,S2));
>               S3try:=evalf(subs(xic=myxic,rhoc=m,Thc=myThc,S3));
>
>               for thetait from 1 to step_angle do
>                    mytheta:=(thetait-1)/(step_angle-1)*Pi;
>                    for phiit from 1 to step_angle do
>                         myphi:=(phiit-1)/(step_angle-1)*Pi;
>
>                         sigma_h:=solve(evalf(subs(S12=0,S23=0,S13=0,S11=S1try,
>                                   S22=S2try,S33=S3try,phi=myphi,theta=thetait,
>                                   -sh^3+I1*sh^2-I2*sh+I3)=0),sh);
>
>                         maxtry_sigma_h:=max(seq(Re(sigma_h[k]),k=1..3));
>                         if  maxtry_sigma_h>maxtry then
>                              maxtry:=maxtry_sigma_h;
>                              phirel_lode[meridianit] := evalf(myphi);
>                              thetarel_lode[meridianit] := evalf(mytheta);
>                         end if;
>
>                    end do;
>               end do:
>               maxtryend:=m:
>               mm:=mm+1.0*(1-maxtry)+0.002;
>          end do:
>
>          S1lode[meridianit]:=S1try;
>          S2lode[meridianit]:=S2try;
>          S3lode[meridianit]:=S3try;
>          lodelode[meridianit]:=myThc;
>          rholode[meridianit]:=m;
>          xilode[meridianit]:=myxic;
>
>          WARNING("DONE: xic=%1, Thc=%2, rhoc=%3, theta=%4, phi=%5, maxtry=%6",
>          myxic,myThc,m,thetarel_xi[lodeit],phirel_xi[lodeit],maxtry);
```

```
>      end do:

> # PLOT of meridian
> cat(plot_lode,round(myThc/evalf(Pi)*180)):=pointplot3d([S1lode,S2lode,S3lode],
    color=black):
> display(plot_lode0,axes=normal,scaling=constrained,view
    =[-15..2,-15..2,-15..2],labels=['S1','S2','S3']):
#
```

Nomenclature

General Abbreviations

α	Volumetric coefficient of Eshelby tensor $\mathbb{S}_{sph}^{cp}$
β	Deviatoric coefficient of Eshelby tensor $\mathbb{S}_{sph}^{cp}$
δ_{ij}	Kronecker delta
γ	Two angles describing the directions of the two principal normal stresses under uniaxial loading relative to the the local r-axis
Λ	Auxiliary variable for substitution in characteristic equation
$\mathcal{I}_{agg}^{ITZ}$	Two-dimensional interface between aggregate and the surrounding three-dimensional ITZ
μ_j	Shear modulus of linear elastic phase j
μ_{agg}	Shear modulus of aggregates
μ_{con}	Homogenized shear modulus of concrete
μ_{cp}	Shear modulus of cement paste
μ_{ITZ}	Shear modulus of linear elastic ITZ
ν_j	Poisson's ratio of phase j
ν_{agg}	Poisson's ratio of aggregates
ν_{cp}	Poisson's ratio of cement paste
ν_{ITZ}	Poisson's ratio of ITZ
Ω	Volume of RVE
Ω_j	Volume of phase j
$\partial\Omega$	Boundary of RVE
$\partial\Omega_{agg}$	Boundary of the aggregate phase, (aggregates' surfaces)
ϕ, θ, r	Spherical (local) coordinates: zenith angle $\phi \in [0, \pi]$, reference is Cartesian z-axis, azimuth angle $\theta \in [0, 2\pi)$, reference is Cartesian x-axis, and radial distance $r \in [0, \infty)$
ϕ_{tu}^{lim}, ϕ_{cu}^{lim}	Zenith angle describing the position at which the onset of ITZ failure under uniaxial tension and compression occurs, respectively
Σ_{cu}^{lim}, Σ_{cb}^{lim}	Model-predicted stress level related to the elastic limit under uniaxial and (symmetric) biaxial macroscopic compressive loading, respectively
σ_{ITZ}^{ult}	Tensile strength of ITZ
$\Sigma_{tu,exp}^{lim}$, $\Sigma_{cu,exp}^{lim}$	Experimentally determined macrostress level related to the elastic limit under uniaxial tension or compression, respectively

Σ_{tu}^{lim}, Σ_{tb}^{lim}, Σ_{tt}^{lim}	Model-predicted macrostress level related to the elastic limit under uniaxial, (symmetric) biaxial, and (isotropic) triaxial macroscopic tensile loading, respectively
$\boldsymbol{Q}$	Transformation matrix, transforms Cartesian components into spherical components
ϱ	Angle between global z-axis and the direction of the largest principal ITZ stress
ϱ_{tu}^{lim}, ϱ_{cu}^{lim}	Angle between global z-axis and the direction of the maximum of the largest principal ITZ stress under uniaxial tension and compression, respectively, i.e. this angles describe the orientation of the normal vector of ITZ crack planes
ξ, ρ, ϑ	Haigh-Westergaard coordinates: hydrostatic component, deviatoric component, and Lode angle respectively, used in macroscopic principal stress space
a	Stress ratio of biaxial stresses, $a = \Sigma_{xx}/\Sigma_{yy} \in [-1\,,1]$
A_{vol}, A_{dev}	Volumetric and deviatoric coefficients of aggregate strain concentration tensor $\mathbb{A}_{agg}$
B_{vol}, B_{dev}	Volumetric and deviatoric coefficient of stress concentration tensor $\mathbb{B}_{agg}$
d	Characteristic size of an RVE
D_{vol}, D_{dev}	Volumetric and deviatoric coefficient of concentration tensor $\mathbb{D}_{agg}$
E_j	Young's modulus of phase j
E_{agg}	Young's modulus of aggregates
E_{cp}	Young's modulus of cement paste
E_{ITZ}	Young's modulus of ITZ
f_j	Volume fraction of phase j
$f_{\mathcal{I}_{agg}^{ITZ}}$	Failure function expressing debonding at $\mathcal{I}_{agg}^{ITZ}$
f_{agg}	Volume fraction of aggregates
f_{cp}	Volume fraction of cement paste
f_{ITZ}	Failure function expressing ITZ failure
G_{vol}, G_{dev}	Volumetric and deviatoric coefficient of $\mathbb{G}$
H_{vol}, H_{dev}	Volumetric and deviatoric coefficient of $\mathbb{H}$
I_1^{Σ}, I_2^{Σ}, I_3^{Σ}	Invariants of macroscopic stress tensor $\boldsymbol{\Sigma}$
I_1^{σ}, I_2^{σ}, I_3^{σ}	Invariants of microscopic stress tensor of ITZ, $\boldsymbol{\sigma}_{ITZ}$
j	Specific phase within an RVE
$J_1^{\boldsymbol{S}}$, $J_2^{\boldsymbol{S}}$, $J_3^{\boldsymbol{S}}$	Invariants of the macroscopic stress deviator $\boldsymbol{S}$
$J_1^{\boldsymbol{s}}$, $J_2^{\boldsymbol{s}}$, $J_3^{\boldsymbol{s}}$	Invariants of the microscopic stress deviator of the ITZ $\boldsymbol{s}$
k_j	Bulk modulus of linear elastic phase j
k_{agg}	Bulk modulus of aggregates
k_{con}	Homogenized bulk modulus of concrete
k_{cp}	Bulk modulus of cement paste
k_{ITZ}	Bulk modulus of linear elastic ITZ
n_p	Number of phases within an RVE
T_r^{ult}	Tensile strength of the $\mathcal{I}_{agg}^{ITZ}$, bond strength
x, y, z	Cartesian Coordinates
ℓ	Characteristic size of embedded heterogeneities in an RVE
$\ell_{con}^{(A)}$	Characteristic length of heterogeneity of concrete-related RVE

$\ell_{ITZ}^{(B)}$	Characteristic length of heterogeneity of the ITZ-related RVE
$\mathcal{L}$	Characteristic size of stress and strain fluctuations inside the structure containing the RVE
$\mathcal{L}_{ITZ}^{(B)}$	Characteristic length of stress and strain fluctuations with respect to the ITZ-related RVE, is equal to $\ell_{con}^{(A}$)
$d_{con}^{(A)}$	Characteristic length of concrete-related RVE
$d_{ITZ}^{(B)}$	Characteristic length of ITZ-related RVE
ITZ	Interfacial Transition Zone
RVE	Representative volume element

Mathematical Symbols and Operators

$\cdot$, :	Single contracting product, double contracting product of tensors, respectively
$\otimes$	Tensor product
∂	Partial differentiation
tr	Trace function of a tensor
$\boldsymbol{Q}^T$	Transpose of transformation matrix $\boldsymbol{Q}$ or of a tensor
$\boldsymbol{\nabla}$	Gradient (nabla symbol)

First-order tensors

$\underline{e}_\phi$, $\underline{e}_\theta$, $\underline{e}_r$	Unit base vector in ϕ-, θ-, and r-direction, respectively, defining the spherical (local) base frame
$\underline{e}_x$, $\underline{e}_y$, $\underline{e}_y$	Unit base vector in x-, y-, and z-direction, respectively, defining the Cartesian (global) base frame
$\underline{n}$	Unit outward normal vector acting on the aggregate-ITZ interface $\mathcal{I}_{agg}^{ITZ}$
$\underline{t}$	Tangent vector acting on the aggregate-ITZ interface $\mathcal{I}_{agg}^{ITZ}$
$\underline{T}_{agg}$	Traction vector acting on the aggregates' surfaces
$\underline{u}$	Displacement vector
$\underline{u}_{agg}$	Displacement vector field within aggregate phase
$\underline{u}_{ITZ}$	Displacement vector field within ITZ
$\underline{x}$	Position vector, labeling points within the RVE and on its boundary

Second-order tensors

$\mathbf{1}$	Second-order unity tensor with components equal to Kronecker delta δ_{ij}
$\boldsymbol{\sigma}_{agg}$	Average microscopic stress tensor of aggregates
$\boldsymbol{\varepsilon}_{agg}$	Average microscopic strain tensor of aggregates
$\boldsymbol{\varepsilon}_j$	Average microscopic strain tensor of phase j
$\boldsymbol{E}$	Macroscopic strain tensor
$\boldsymbol{E}_\infty$	Auxiliary macroscopic strain tensor in a matrix-inclusion problem, imposed on the infinite boundary
$\boldsymbol{S}$	Macroscopic stress deviator, corresponds to macroscopic stress tensor $\boldsymbol{\Sigma}$

$\boldsymbol{s}$	Microscopic stress deviator, corresponds to ITZ stress tensor $\boldsymbol{\sigma}_{ITZ}$

Fourth-order tensors

$\mathbb{A}_{agg}$	Strain concentration tensor of aggregates
$\mathbb{A}_{cp}$	Strain concentration tensor of cement paste
$\mathbb{A}_j$	Strain concentration tensor of phase j
$\mathbb{B}_{agg}$	Stress concentration tensor of aggregates
$\mathbb{C}_\infty$	Auxiliary stiffness tensor of the infinite matrix in a matrix-inclusion problem
$\mathbb{C}_j$	Stiffness tensor of phase j
$\mathbb{C}_{agg}$	Stiffness tensor of aggregates
$\mathbb{C}_{con}$	Homogenized elastic stiffness tensor of concrete
$\mathbb{C}_{cp}$	Stiffness tensor of cement paste
$\mathbb{C}_{hom}$	Homogenized stiffness tensor of the RVE
$\mathbb{D}_{agg}$	Fourth-order concentration tensor, linking macrostress $\boldsymbol{\Sigma}$ to microscopic aggregate stresses $\boldsymbol{\varepsilon}_{agg}$
$\mathbb{G}$, $\mathbb{H}$	Isotropic fourth-order auxiliary tensors
$\mathbb{I}$	Fourth-order identity tensor with components $I_{ijkl} = \frac{1}{2}\left(\delta_{ik}\delta_{jl} + \delta_{il}\delta_{kj}\right)$
$\mathbb{J}$	Volumetric part of the fourth-order unity tensor, $\mathbb{J} = 1/3\ \mathbf{1} \otimes \mathbf{1}$
$\mathbb{K}$	Deviatoric part of the fourth-order unity tensor, $\mathbb{K} = \mathbb{I} - \mathbb{J}$
$\mathbb{P}_j^\infty$	Hill tensor of phase j embedded in infinite matrix
$\mathbb{P}_{shp}^{cp}$	Hill tensor of a spherical inclusion embedded in an infinite matrix of cement paste
$\mathbb{S}_{shp}^{cp}$	Eshelby tensor of a spherical inclusion embedded in an infinite matrix of cement paste